Acoustic Signal-based Underwater Oil Leak Detection and Localization

by

© Geetha Varsha Kosanam Chandrasekar, B.E.

A thesis submitted to the

School of Graduate Studies

in partial fulfilment of the

requirements for the degree of

Master of Engineering

Department of *Electrical and Computer Engineering*

Memorial University of Newfoundland

May 2021

St. John's Newfoundland

Abstract

Underwater Wireless Sensor Networks (UWSNs) have been becoming popular for exploring offshore, natural resource development, geological oceanography, and monitoring the underwater environment. The acoustic channel characteristics in underwater impose challenges, including limited bandwidth, signal attenuation, and propagation delay that limits UWSN utilization. The marine environment is under threat from pollution, which impacts human life and activities. Compared to other pollution types, the oil leak is a significant threat to the marine ecosystem. When the leaked oil or other petroleum products mix with water in the ocean, significant biological and economic impacts could result.

Although much research has focused on improving the reception and processing of acoustic signals, increasing performance, and reducing packet delay, no significant research results have been reported on finding an effective early-stage leak detection method using acoustic signal processing. Accurate information about oil spill location and its characteristics is much needed for oil spill containment and cleanup operations. Developing an efficient underwater oil leak detection and localization algorithm is still challenging in UWSNs because of the impairments of the acoustic channel. In this thesis, we propose a technique that detects the presence of an oil leak in the underwater environment at an early stage. We also propose a localization algorithm that determines the approximate location of the oil leak.

Firstly, we review the propagation properties of acoustic signals to understand acoustic communication in the marine environment better. We then discuss the transmission of sound in terms of reflection and refraction. We propose a leak detection technique based on the range estimation method to detect oil leak at an early stage before reaching the ocean surface. We perform a two-dimensional analysis for evaluating the performance of the proposed detection technique. To investigate the proposed technique, we perform evaluation with different network sizes and topologies. We discuss the detection ratio, network scalability,

power and intensity of the received signal. We then perform a three-dimensional analysis to evaluate the performance of the proposed technique. We conduct theoretical analysis to investigate the proposed technique in terms of detection ratio, network scalability, power and intensity of the received signal. We assess the efficiency of the proposed detection method by considering an oil leak at different ocean levels.

Finally, we propose a cooperative localization algorithm for localizing the leak in the UWSN. We then evaluate the proposed localization algorithm for two different topologies. Our results show that our proposed technique works well for an underwater network with concentric hexagonal topology. We can extend the proposed method for other types of targets with different shapes and sizes.

Dedicated to my Mom and Dad

Acknowledgements

First and foremost, I would like to express my sincere appreciation and gratitude to my supervisors Dr. Ramachandran Venkatesan and Dr. Cheng Li, for giving me the opportunity to do my research and for their guidance, advice, encouragement, support throughout my graduate program.

I would like to gratefully acknowledge the financial support provided by School of Graduate Studies and my supervisors. I would also like to thank Dr. Faisal Khan, Associate Dean of Graduate Studies, for ensuring smooth operation of the administrative aspects of my graduate program.

I would like to thank my parents Mr. Chandrasekar and Mrs. Bhuvaneswari, for their unconditional love, prayers, and affection. I would also like to thank my sister Gajalakshmi for encouraging me during my program.

I am extending heartfelt thanks to my uncle Dr. Munaswamy Katna and my aunt Mrs. Saraswathy Katna for their continued support since I moved to St. John's. I would also like to thank my friends and colleagues for their continuous support during my graduate program.

Contents

List of Abbreviations

AAL	AUV-aided localization
ADCP	Acoustic Doppler Current Profiler
AoA	Angle of Arrival
ALAN	Acoustic Local Area Network
AUV	Autonomous Underwater Vehicle
BC	British Columbia
BER	Bit Error Rate
BPS	Buoy Profiling System
CODAR	Coastal Ocean Dynamics Applications Radar
COFDL	Coastal and Ocean Fluid Dynamics Laboratory
CTD	Conductivity, Temperature, and Depth
DMAS	Data Management and Archiving System
DNRL	Dive and Rise Localization
DoA	Distance of Arrival
ESONET	European Seas Observatory NETwork
FH/FSK	Frequency-Hopping Frequency Shift Keying
GBS	Gravity Based Structure
GPS	Global Positioning System

GTD	Gas Tension Device
H2O	Hawaii 2 Observatory
HOV	Human Occupied Vehicle
LAN	Local Area Network
LRAUV	Long Range Autonomous Underwater Vehicle
LEO	Long-term Ecosystem Observatory
MAC	Medium Access Control
MARS	Monterey Accelerated Research System
MBARI	Monterey Bay Aquarium Research Institute
MEF	Main Endeavour Vent Field
MOEN	Meridional Overturning Exchange with the Nordic Seas
MVCO	Martha's Vineyard Coastal Observatory
NEPTUNE	North East Pacific Time-series Underwater Networked Experiments
NE-RCM	North East Regional Circulation Moorings
NeMO	New Millenium Observatory
NOAA	National Oceanic and Atmospheric Administration
N-RCMP	North RCM Platform
NW-RCM	North West Regional Circulation Moorings
OTTB	Ocean Technology Test-Bed
PL	Proxy Localization
PLUTO	Panama LJL Underwater Tropical Observatory
PRIMO	Polar Remote Interactive Marine Observatory
PSK	Phase shift keying
RF	Radio Frequency

ROV	Remotely Operated Vehicle
SAR	Synthetic Aperture Radar
SISO	Single-Input Single-Output
SL	Silent Localization
SLMP	Scalable Localization with Mobility Prediction
SNR	Signal-to-Noise Ratio
TL	Transmission Loss
ToA	Time of Arrival
UWSN	Underwater Wireless Sensor Network
WHOI	Woods Hole Oceanographic Institution
WSN	Wireless Sensor Network
VENUS	Victoria Experimental Network Under the Sea
VIP	VENUS Instrument Platform
ZAP	Zooplankton Acoustic Profiler

List of Symbols

$a_{water}(f)$	Absorption coefficient of sound in seawater
$a_{oil}(f)$	Absorption coefficient of sound in crude oil
c_{oil}	Speed of sound in oil
c_{water}	Speed of sound in seawater
c_{air}	Speed of sound in air
d_c	Distance between two adjacent nodes
E_R	Energy reflection coefficient
E_T	Energy transmission coefficient
f	Operating frequency
κ	Spreading factor
l	Distance between source node and receiver node
l_p	Reference pressure
l_{pwr}	Reference power
l_r	Reference distance
μ_s	Shear viscosity of oil
μ_B	Bulk viscosity of oil
N_s	Number of sensor nodes
N_h	Number of hexagons

ω	Angular frequency
p_t	Transmit power in Watts
P_t	Transmit power in dB
P_T	Pressure transmission coefficient
p_r	Received power in Watts
P_r	Received power in dB
P_R	Pressure reflection coefficient
ρ_{oil}	Density of oil
ρ_{water}	Density of seawater
θ_i	Angle of incidence
θ_r	Angle of reflection
θ_t	Angle of transmission
θ_c	Critical angle
V_R	Velocity reflection coefficient
V_T	Velocity transmission coefficient
z	Acoustic impedance

List of Tables

List of Figures

Chapter 1

Introduction

1.1 Overview

Underwater Wireless Sensor Networks (UWSNs) have been used for underwater surveillance, military applications, security monitoring, onshore exploration, disaster prevention and monitoring, geological oceanography, and natural resource development [1][2][3]. The ideal communication solution for long-term monitoring of UWSN is a Local Area Network (LAN). The Woods Hole Oceanographic Institution (WHOI), Northeastern University, and Monterey Bay Aquarium Research Institute (MBARI) took a collaborative effort to develop the Acoustic Local Area Network (ALAN) Protocol. ALAN protocol was deployed in Monterey Canyon, off California, with sensor nodes placed on the ocean bed, and one central surface deployed receiver [4]. The sensor nodes on the seabed transmit data to the surface node via an acoustic link. The data is then sent to the shore station using radio frequency (RF) link via batch fashion. The other examples of UWSN include Seaweb'98, Seaweb'99, and Seaweb 2000. Seaweb '98 and Seaweb '99 is a non-centralized bi-directional network with 10 and 15 battery-powered and anchored nodes. Seaweb 2000 advanced the network deployment by introducing telesonar modem hardware and a compact protocol [5]. Figure

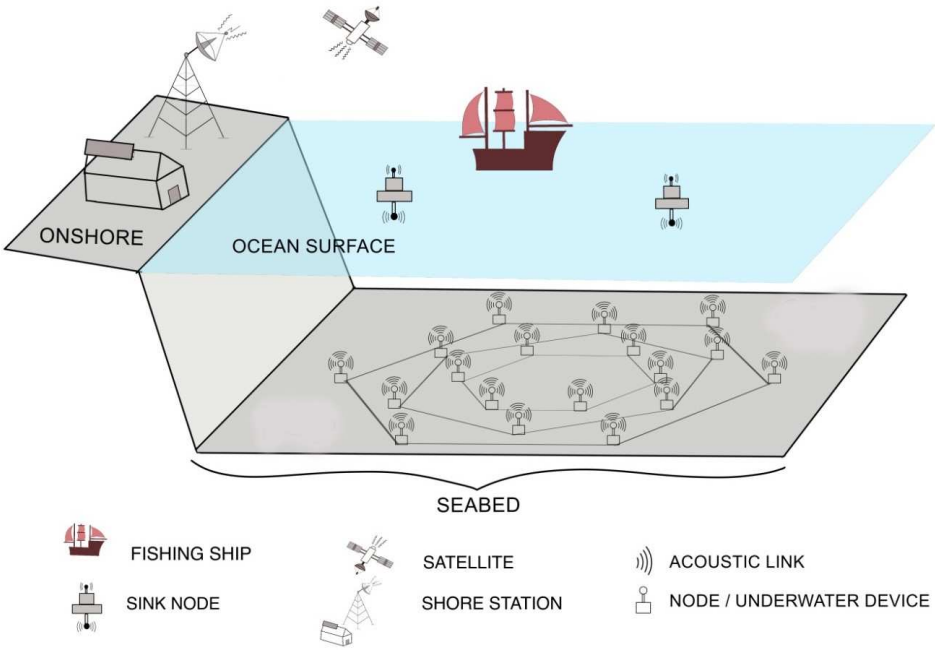

Figure 1.1: Illustration of underwater wireless sensor network

1.1 shows the illustration of UWSNs with a set of nodes at the ocean floor, a pair of surface buoyed nodes, onshore base station. The surface node collects the data from sensor nodes on the seabed via the acoustic link and sends it to the satellites via a radio link. The shore station can then download this data from the satellite. The UWSNs are later expanded by increasing the design and deployment of underwater vehicles such as autonomous underwater vehicles (AUVs), remotely operated vehicles (ROVs), and human occupied vehicles (HOVs). These underwater vehicles are equipped with sensors for exploring the marine environment [6][7][8][9]. Figure 1.2 shows the illustration of UWSNs with AUV, which collects information from the sensor nodes located on the ocean floor. The AUV then returns to the surface ship and reports the collected data. The radio signals used in Wireless Sensor Networks (WSNs) do not propagate well in UWSN because of their high attenuation and absorption rate [10][11]. Optical signals are easily absorbed or dispersed by suspended particles in the upper part of the seawater. These optical signals can reach only a few hundred meters in

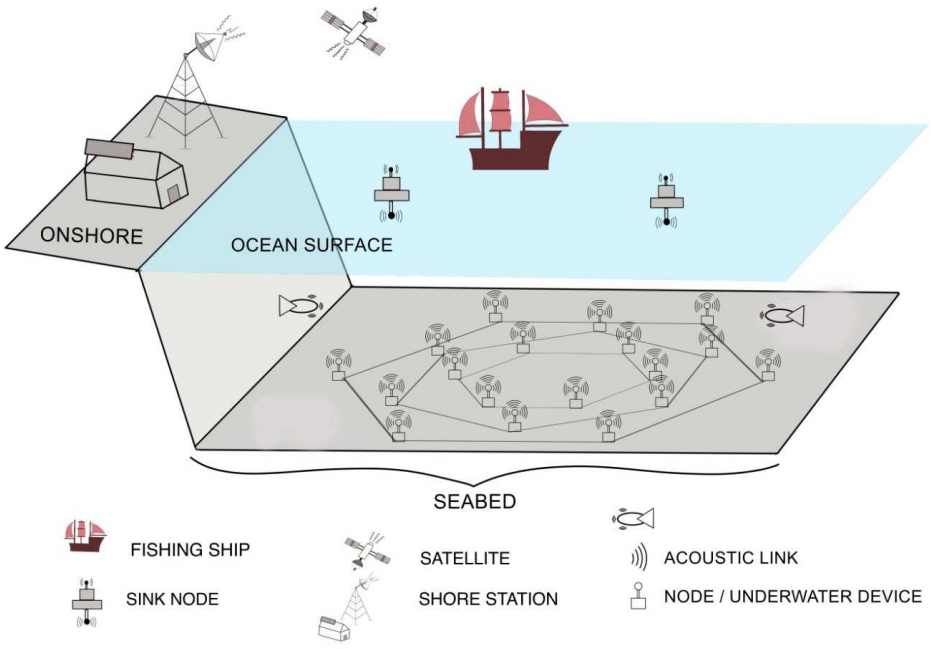

Figure 1.2: Illustration of underwater wireless sensor network with AUV

the seawater [12][13][14]. Acoustic waves are used in the underwater environment due to the high attenuation, absorption, and dispersion of radio waves and optical waves. Acoustic waves can travel a few thousands of meters or more in seawater, and the communication quality is better than electromagnetic signals because of low attenuation [15][16][17].

Underwater Acoustic Communication (UAC) uses hydrophones for sending and receiving the signals in the underwater environment. The performance of underwater communication is related to acoustic channel conditions. Acoustic communication in the marine environment pose difficulties due to multipath, fading, and high bit error rate (BER), making it different from other terrestrial networks [18]. The energy is limited in acoustic communications because of the non-chargeable battery in the sensor nodes. The data rate of acoustic communications (i.e., 1 or few kb/s) is lower than that of RF communications because of the low bandwidth of acoustic signals. The data rate of acoustic communications increases when the transmission distance is shorter, with more sensor nodes. High-density UWSN

brings additional challenges because of the high cost of acoustic devices. In Section 2.2.2, we summarize the acoustic modems that can be used for academic and commercial purposes.

Network deployment strategy is an issue in UWSNs due to the high cost of acoustic devices and deployment. For the past 50 years, two-dimensional and three-dimensional architectures are used in the underwater marine environment. In two-dimensional architecture, the sensor nodes are placed on the seabed using regular topology such as ring, star, or grid because randomly distributed network topology is not realistic for the underwater environment. The position information of the sensor nodes is assumed to be known *a priori*. In three-dimensional architecture, the sensor nodes are deployed in different ocean levels to connect to the surface nodes [19]. The sensor nodes deployed in the marine environment are used for different applications such as detecting illegal fishing ships, icebergs, oil spills, etc.

The marine environment is under threat from pollution, which impacts human activities and life. Increasing concern about pollution levels in the ocean and coastal regions has resulted in multiple strategies to monitor and reduce marine pollution to achieve sustainable marine water quality. Compared to other marine pollution types, the oil leak is a significant threat to the marine ecosystem because the hydrocarbons present in the oil can have biological and economic impacts. Pipeline breakage is the most common reason for the occurrence of oil spills reported in the past decade. These submarine pipelines are laid on the seabed to transport oil or gas from the drilling rig. Figure 1.3 shows the illustration of UWSN with the presence of an oil rig. The sensor nodes are placed near the oil rig to detect leak from the pipeline. The summary of different types of oil rigs is given later in Section 2.4. The parameters and conditions used in this thesis are based on the oil rigs in the Newfoundland and Labrador region.

Underwater observatory is a network with a single node or a set of nodes connected via

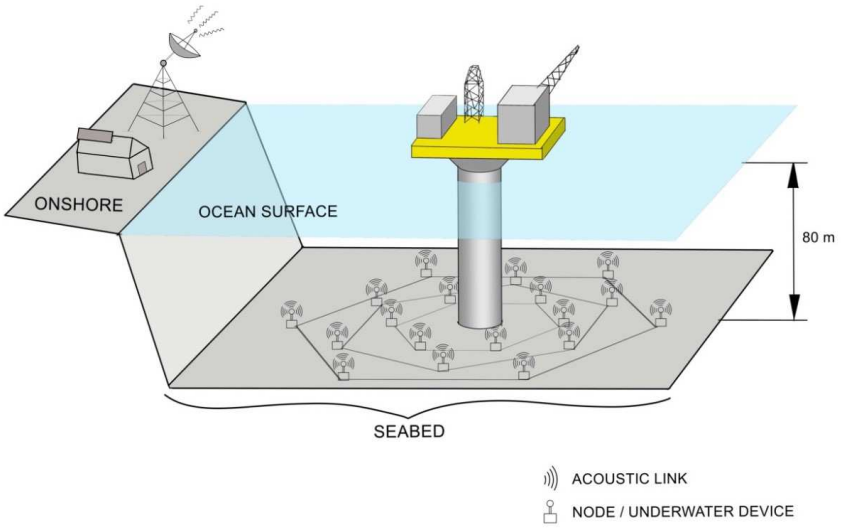

Figure 1.3: Illustration of underwater wireless sensor network with oil rig platform

fibre optic cable. In addition to the sensor nodes, observatories include a camera platform, buoy profiling system, shore station, and water column devices for measuring the water properties, seismic activities, and other biological activities. There are three types of underwater observatories, such as global observatory, coastal observatory, and regional cabled observatory. We discuss underwater observatories in detail in Section 2.1.

This thesis addresses the detection and location efficiency of oil spills based on the proposed approach for UWSNs in long-term marine monitoring applications. Through a comprehensive understanding of shallow water acoustic channels and network topologies, the approaches proposed in this thesis consider the network connectivity, which we utilize for monitoring leaks in the UWSNs.

1.2 Motivation of the Research

This research is a part of a project that involves detecting the targets such as ships, icebergs, and oil spills in the marine environment. Our research mainly focuses on the detection and localization of oil spills in the underwater environment.

An oil spill is an accidental release of petroleum hydrocarbons into the marine ecosystem. The spill happens from the offshore platforms, drilling rigs, oil tankers, and the underwater oil pipelines. The spilled oil travels to the surface and forms an oil slick. This oil slick spreads in the water surface because of wind and surface current. Oil spill causes harmful consequences to the marine and coastal ecosystems. The crude oil or the refined fuel spills from the tanker ship accidents have affected the ecosystems in Alaska, the Gulf of Mexico, Galapagos Island, Sundarbans, and many other places. In recent times, one of the massive oil spills was the deepwater horizon oil spill in 2010 that resulted in 4.9 *million* barrels of oil spilled in the Gulf of Mexico, which significantly impacted flora and fauna. It also affected people living along the coast and killed many animals, including birds, sea turtles, mammals, and fishes. After the oil spill, cleanup and recovery operations are difficult and expensive because it depends upon many factors, including the temperature of the water, type of oil spilled, variety of shorelines, and beaches involved. Therefore, to reduce the impact of the oil spill and prevent the massive oil spill from happening, early and accurate leak detection and localization of leaks are necessary, ensuring a quick and targeted response to the affected location.

Remote sensing is a widely used method for the detection of oil spills. It is classified into passive and active remote sensing. Passive remote sensing sensors exploit the optical properties of the oil, such as relative reflectance and relative absorbance, to distinguish the oil from the water. On the other hand, active remote sensing uses synthetic-aperture radar (SAR) to capture the images of the spilled oil in the water surface. Though remote sensing is

widely used to detect oil spills on the water surface, this method depends on several factors including, weather, time, and wind speed. Much of the research in the past decade focused on detecting oil spills using remote sensing and fibre optics. In contrast, very little work has been done to detect the oil spill at the early stage using acoustic signal processing. We utilize wireless acoustic sensing for obtaining information from the sensor of other nodes. In long-term marine monitoring applications, under the challenging conditions of the underwater environment, developing a leak detection approach that detects the leak from the pipeline before reaching the ocean surface becomes more important.

Wireless Sensor Networks (WSNs) often use randomly distributed network topology for deploying the nodes in the network. Nevertheless, the randomly distributed topology is not realistic in the underwater marine environment. The predetermined and regular topologies are more suitable for UWSNs [20] [21]. Unlike WSN, UWSN uses fewer nodes because of the high cost of acoustic devices and deployment costs. Therefore, we should consider regular topology with fewer nodes in UWSNs. In this thesis, we assess different aspects related to the detection efficiency in UWSNs. Power, intensity, and network connectivity are closely related to the propagation properties of acoustic signals in the marine environment. Because of the high cost of sea trials, researchers utilize models that better resemble realistic channels. A semi-empirical formula is a convenient approach for estimating shallow water acoustic channels [16].

The range estimation method provides a way for detecting the presence of oil leaks from the pipeline using direct and reflected propagation properties of acoustic signals. The cooperative localization algorithm in the underwater environment estimates the location of the oil leak approximately. The early containment methods to detect the leak before it reaches to the surface should be studied. The main objective of our research is to develop an early-stage leak detection and localization method that yields a 90% detection and localization ratio.

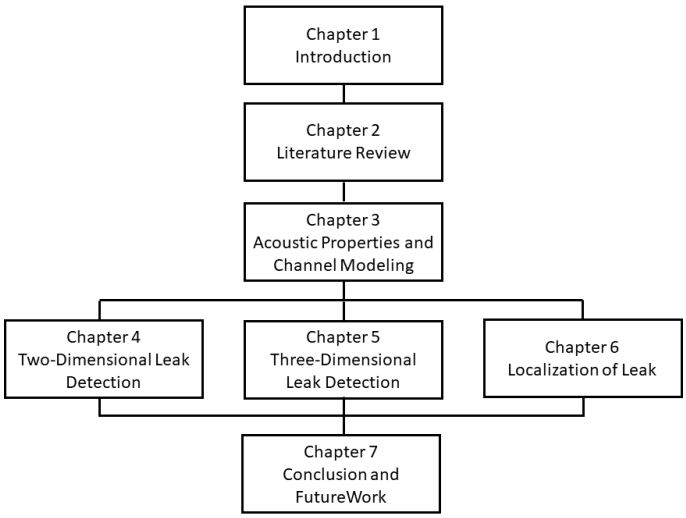

Figure 1.4: Thesis organization

We aim for a modest detection and localization ratio of 90% because of the complications and challenges of the underwater environment.

1.3 Thesis Organization

The thesis organization is illustrated in Figure 1.4. In this thesis, our primary goal is to detect and localize the oil leak effectively. The parameters used in this thesis are obtained from underwater acoustic channels and the specifications of commercial acoustic modems. The power parameters of Sonardyne Modem 6 Sub-Mini are discussed in Chapter 2 and used in Chapters 4, 5, and 6.

Chapter 2 presents a literature review of underwater observatories with its applications. The modems that are used for communication purposes in commercial and academic areas are described. The shallow acoustic channels and their propagation properties are discussed. Different oil rig platforms and their operations are categorized based on the type of oil rig platforms. In particular, methods for leak detection designed for the detection of oil leak are

closely examined. Finally, the localization techniques developed so far for locating the leak are discussed.

In Chapter 3, we study the propagation properties of the acoustic signal in seawater. We discuss transmission loss in the seawater and present the semi-empirical formula for calculating the transmission loss. We utilize the semi-empirical formula for calculating the absorption loss of sound in seawater. We also present the expressions for other signal properties such as power, intensity, and time of arrival (ToA). We study the different deployment process and regular topologies we used in our research.

Chapter 4 describes the two-dimensional analysis of the range estimation approach for leak detection in UWSN for long term marine monitoring applications. We present the two different topologies and investigate the operations of sensor nodes for detecting the leak in UWSNs. We then assume the different shapes and sizes for two-dimensional analysis of oil leak at the different levels of oceans (seafloor, middle of the sea, and the ocean surface). We conduct a theoretical analysis to investigate the detection ratio of the proposed approach for different topology sizes. Performance evaluation of the proposed scheme is studied for different leak sizes under different topology densities for varied transmission ranges. To get a better detection ratio, we perform three-dimensional analysis, which is discussed in Chapter 5.

In Chapter 5, we study the results of different shapes and sizes of the oil leak in UWSNs. We present the three-dimensional analysis of the range estimation approach to achieve a better detection ratio than the two-dimensional analysis discussed in Chapter 4. We consider both direct and reflected propagation properties of acoustic signals. We evaluate the performance of the three-dimensional analysis for different leak sizes under different topology densities for varied transmission ranges and by using different numbers of nodes. We then conduct a theoretical analysis to compare the detection ratio of two-dimensional and

three-dimensional analyses of the range estimation approach.

Chapter 6 proposes the cooperative scheme between the sensor nodes placed on the seabed to estimate the location of the leak in UWSNs. First, the basic cooperative communication scheme is described. We then present a localization algorithm for estimating the location of the oil leak approximately. The location of the leak is estimated by considering the time consumption and the number of sensor nodes involved in leak detection. Furthermore, the received power of the signal is considered for estimating the leak location effectively. We evaluate the performance of the proposed localization algorithm for two different topologies. The thesis is concluded in Chapter 7. Suggestions for possible expansion of the work presented in this thesis for future research are provided.

Chapter 2

Literature Review

In this chapter, we summarize underwater observatories established so far and their applications. Acoustic and optical modems are an essential part of underwater communications. We present and compare the performance of a few optical and acoustic modems available for UWSNs. We survey the different oil platforms, their operations, and applications categorized based on the type of oil platforms. We review underwater acoustic channel models for shallow and deep water reported in the past 20 years to understand protocol designs for UWSNs better. Different leak detection methods, including interior, exterior, and visual techniques are discussed. Interior and exterior leak detection methods consider the area in and out of the pipeline in the underwater environment. Also, we examine the different localization techniques reported in the past 20 years for UWSNs.

2.1 Underwater Observatories

Centuries ago, citizens and scientists observed the ocean from the shore. Then, they started to observe from the ships, submersibles, and recently from satellites. To understand and interact with the sea, the scientists developed ocean observatories for long-term marine

monitoring. Ocean observatories consist of suites of instruments and sensors with stable power supplies and permanent communication links to feed data and the Internet to the devices. Ocean observatories use novel technologies such as satellite communications, acoustic modems, and fibre-optic cables that are spread several miles across the seafloor. Observatories allow the scientists to collect the data passively and adjust the instruments from several miles away in shore-based laboratories. Some ocean observatories and observing platforms are already in operation, whereas some larger observatories are under construction. According to WHOI, ocean observatories generally fall into three categories: regional cabled observatory, coastal observatory, and global observatory. We discuss each observatory and present the information about the observatory useful for our research and its applications in the following sections.

2.1.1 Coastal Observatory

A coastal observatory is a monitoring system in coastal waters, including cabled instruments, AUVs, moorings, buoys, and floating platforms, to provide comprehensive data on multiple parameters required to understand the physical, chemical, and biological processes in coastal waters. Most of the coastal observatories provide real-time data by using telemetry [22]. Generally, coastal observatories consist of fixed platforms and buoys with instruments and sensors to measure temperature, salinity, current profiles, and meteorological conditions. Scientists monitor the health and safety of coastal environments by exploring the fundamental processes of the estuaries. In many places of the north sea and baltic sea, fixed automated measuring stations are in operation. A coastal observatory includes additional components such as sensors for measuring turbidity, chlorophyll and nutrients, drifters for measuring surface currents and surface properties, research vessels to service moorings, meteorological data from local met stations, and tide gauges.

Some of the cabled coastal observatories are Martha's Vineyard Coastal Observatory (MVCO), Victoria Experimental Network Under the Sea (VENUS), Panama LJL Underwater Tropical Observatory (PLUTO), Long-term ecosystem observatory (LEO), Polar Remote Interactive Marine Observatory (PRIMO), and coastal observatory research arrays. This type of observatory also consists of observing systems using buoys, moorings, and other platforms such as coastal observing systems clearinghouse, eastern consortium of coastal ocean observatories, Gulf of Maine ocean observing system, new approaches for coastal observatories, southeast atlantic coastal ocean observing system, Chesapeake Bay observing system, southern California coastal ocean observing system, and Sargasso sea ocean/atmosphere observatory.

2.1.1.1 Martha's Vineyard Coastal Observatory (MVCO)

WHOI built Martha's Vineyard Coastal Observatory (MVCO) near south beach in Edgartown [23]. This project was initiated in the Coastal and Ocean Fluid Dynamics Laboratory (COFDL) at WHOI for studying the coastal atmospheric and oceanic processes. This observatory provides long-term ($25-30$ years) observation for climate studies. MVCO consists of a small shore lab near Katama Airpark, a 10 m meteorological mast near the south beach, a subsurface node at 12 m deep and an air-sea interaction tower with a topside node. A buried electro-optic power cable connects the meteorological and the subsea instrumentation to the shore lab. The meteorological mast consists of instruments for measuring the wind speed, the direction of the wind, temperature, humidity, precipitation and fluxes. The offshore node consists of oceanographic sensors for measuring current profiles, waves, salinity and temperature.

2.1.1.2 Victoria Experimental Network Under the Sea (VENUS)

The Victoria Experimental Network Under the Sea (VENUS) is the world's first cabled seafloor observatory that began its operations in early 2006 with a single node at 100 m depth hosted near Saanich Inlet. The VENUS observatory then expanded into the Strait of Georgia, which lies between Vancouver in the mainland and Vancouver Island. This observatory has two nodes at 300 m and 170 m water depth and an extension at Fraser delta at 175 m water depth, as shown in Figure 2.1. VENUS observatory network aims to study coastal oceans through its two sites near Victoria and Vancouver, BC. VENUS uses the Internet, telecommunication technology, and a network of about 50 km of fibre optic cables at a maximum depth of 300 m to create a permanent link to cameras and other monitoring instruments on the seafloor. VENUS uses sonar to build acoustic profiles that estimate the stability of the muddy shelf deposits [24] [25] [26].

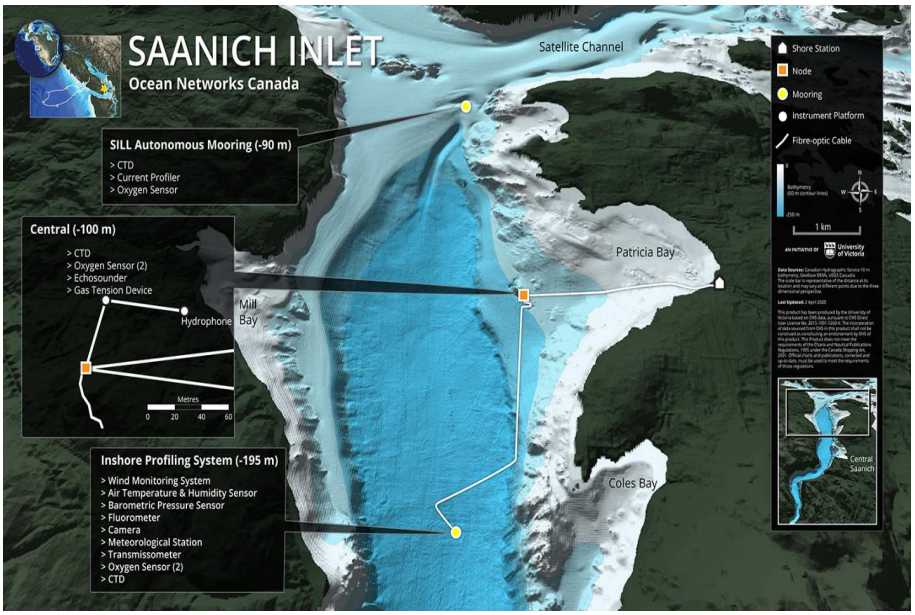

Figure 2.1: Pictorial representation of Saanich Inlet [24]

The observatory infrastructure in Saanich Inlet includes a shore station, a subsea node

100 m depth), platforms with instruments and sensors, autonomous mooring at the entrance to the inlet, cabled buoy profiling system south near Coles Bay, and the ocean technology test-bed (OTTB) buoy platform in Patricia Bay as shown in Figure 2.2. It also has a mini observatory at Brentwood College with necessary sensors that measure water properties at 8 m depth [27] [28].

The Saanich shore station is one of two shore stations in the VENUS observatory. The shore station provides a link between scientists and the undersea activity being monitored in the inlet. The ocean sensor data carried by fibre optic cables are connected to the network computer at the shore station. This computer transmits the data to the Data Management and Archiving System (DMAS) at the University of Victoria, where the information is accessible to scientists. Much of the scientific data that passes through the Saanich shore station is available for the public in the VENUS observatory's data portal.

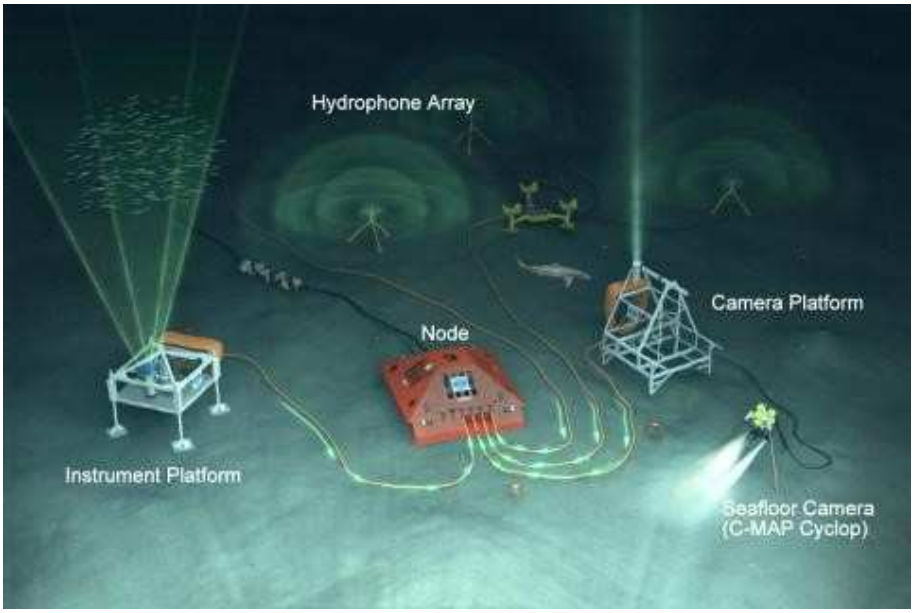

Figure 2.2: Pictorial representation of Saanich Inlet node [24]

The Saanich Inlet node, located at 98 m deep, is a part of VENUS observatory, a cabled

undersea laboratory for ocean researchers and explorers. It is the central hub of energy and communications connecting many ocean sensors deployed across the Saanich Inlet. This node directly connects to the VENUS Instrument Platform (VIP – Saanich Inlet) and Saanich Inlet Camera Platform. These platforms operate with the help of this node. VIP is shown in Figure 2.3.

Figure 2.3: Pictorial representation of VIP - Saanich Inlet [24]

This platform is one of the primary sites containing ocean sensors in the VENUS Saanich Inlet observatory. The VIP platform has a large steel frame supported by four steel legs rested on the seabed at 95 m depth. The ocean sensing devices hosted by this platform are changed every year. The currently hosted devices include:

1. CTD recorder: measures ocean conductivity (S/m), temperature (^oC), depth via pressure ($dbar$) and calculated values for salinity (PSU) and sound velocity (m/s)

2. Two different types of oxygen sensors

3. Gas Tension Device (GTD): measures the pressure of the total dissolved gases in the water

4. Zooplankton Acoustic Profiler (ZAP).

The scientists who work in the Saanich Inlet use the information collected by these devices to understand the natural marine processes and monitor changes due to human activities and climate changes. Saanich Inlet is considered one of the well-studied marine basins globally because of the Saanich Inlet observatory. It was selected for close observation because of its unique plankton-rich environment despite its deep waters and low oxygen levels. Due to this factor, VENUS observatory focuses on marine ecology and zooplankton monitoring in the Saanich Inlet. The scientists use the information collected by these devices to understand the natural marine processes and monitor changes due to human activities and climate changes. The camera platform is shown in Figure 2.4.

Figure 2.4: Pictorial representation of camera platform - Saanich Inlet [24]

The VENUS camera platform is on the ocean floor, where the water depth is 92 m. This platform provides a frame containing the range of ocean sensors that provides pictures of marine life and processes along the seafloor in the Saanich Inlet. The sensors include:

1. High-resolution camera: captures videos and images of the seabed

2. CTD recorder: measures ocean conductivity (S/m), temperature (C), depth via pressure ($dbar$) and calculated values for salinity (PSU) and sound velocity (m/s)

3. Oxygen sensor: measures dissolved oxygen content along the seafloor

4. Turbidity meter: measures the haziness of the water due to the presence of suspended particles.

Figure 2.5: Pictorial representation of buoy profiling platform [24]

The VENUS Buoy Profiling System (BPS) is part of the VENUS Phase II - Geospatial Expansion development in the VENUS Observatory. BPS is shown in Figure 2.5. BPS was in its testing stages at the Ocean Technology Test Bed (OTTB) before deployment in its permanent location in the central Saanich Inlet, west of Coles Bay. The BPS consists of a meteorological station, surface winch, and control system connected to the VENUS node in Patricia Bay. BPS will allow scientists to study marine life and processes in the water column, rather than on the seafloor.

Strait of Georgia:

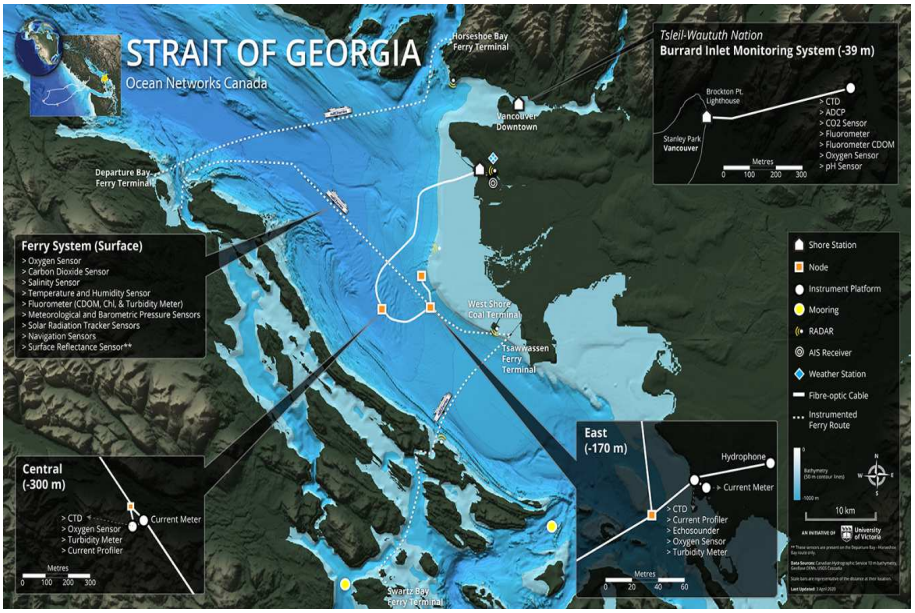

Figure 2.6: Pictorial representation of Strait of Georgia [29]

The Strait of Georgia consists of two full nodes and one mini node located southwest of the Fraser River's main mouth, including a deep node at 300 m and a shallow node at 170 m, as shown in Figure 2.6. The central node connects to the central VIP, which hosts a range of ocean sensors that measure marine life and oceanic processes along the Strait floor [30]. The instrument platform in the Strait of Georgia include:

1. Seafloor network linking three nodes at 300 m(central), 170 m(east) and 175 m (Fraser delta)

2. CTD recorder with dissolved gas sensors

3. ADCP for measuring the vertical structure of water currents

4. A suite of fixed and mobile systems monitoring the surface and water column conditions

5. Two shores based high-frequency radar (CODAR with two antennas) installations to measure the surface currents from Iona to Tsawwassen

6. Thermosalinograph systems installed on BC ferries to monitor surface properties of water

7. Seasonal glider missions to monitor both phytoplankton blooms in spring and profound water renewal events.

2.1.1.3 Long-term Ecosystem Observatory (LEO)

The Institute of Marine and Coastal Sciences at Rutgers University developed the Long-term Ecosystem Observatory (LEO). This observatory monitors the processes in the ocean with online IT systems. It consists of sensors for measuring temperature, salinity and pressure of the ocean water [31].

2.1.1.4 Panama LJL Underwater Tropical Observatory (PLUTO)

The Panama LJL Underwater Tropical Observatory (PLUTO) is located northwest of Panama city at the water depth of 18 m. This observatory consists of an underwater camera, an array of temperature sensors, down-welling lights, and sensors. The underwater fibre-optic cable was used to send the data from the node to the shore station [32].

2.1.1.5 Polar Remote Interactive Marine Observatory (PRIMO)

The Polar Remote Interactive Marine Observatory (PRIMO) is a cabled observatory located to the south of Palmer station at a depth of 130 m. An electro-optical cable connects the instruments of the observatory. The observatory consists of a vertical profiler with CTD, current meter, sensors for chlorophyll and CDOM fluorescence, oxygen, nitrate, a bio-optical package, and an under-ice video observation surveillance system. The electro-optical cable

connects the instruments of the observatory. The profiler rises to the surface multiple times per day from a seafloor-mounted platform consisting of a winch, ADCP and a remote video camera [33].

2.1.2 Global Observatory

Global observatories consists of drifters, arrays of buoys, floats with acoustic modems for examining the ocean-wide process. Some of the global observatories are Argo, OceanSITES, and New Millenium Observatory (NeMO).

2.1.2.1 Argo

Argo is a global array with 3,000 free-drifting profiling floats to measure the temperature and salinity of 2000 m from the ocean's surface. It allows for the continuous monitoring of the temperature, velocity and the salinity of the upper ocean [34].

2.1.2.2 OceanSITES

OceanSITES is a long-term deepwater reference station that measures dozens of variables and monitors the ocean's full depth about 5000 m. The growing OceanSITES consists of 30 surface and 30 subsurface arrays. OceanSITES moorings play as an integral part of the Global Ocean Observing System (GOOS) [35] [36].

2.1.2.3 New Millenium Observatory (NeMO)

The project NeMO was led by NOAA's Pacific marine environmental laboratory to establish a multi-year observatory along the Juan de Fuca ridge [37].

2.1.3 Regional Cabled Observatory

The regional cabled observatories use fibre-optic cables and electric power cables to establish grids for sensors on the ocean floor and in the water column. Some of the regional cabled observatories are NEPTUNE, MARS, H2O, and ESONET.

2.1.3.1 North East Pacific Time-series Underwater Networked Experiments (NEPTUNE)

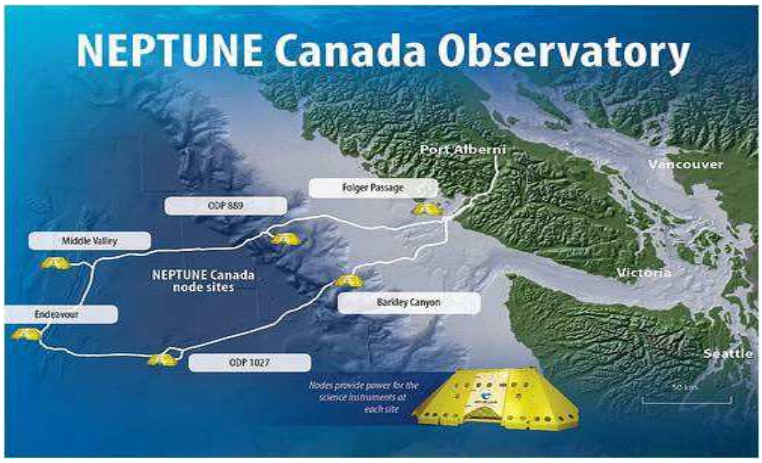

Figure 2.7: Pictorial representation of NEPTUNE network [38]

North East Pacific Time-series Underwater Networked Experiments (NEPTUNE) is the largest cabled ocean observatory located in the northeast Pacific Ocean [38] [39]. NEPTUNE is based on an 840 km loop of fibre optic cable installed from a shore station at Port Alberni across the continental shelf into the deep sea as in Figure 2.7. Nodes were instrumented on the continental shelf at Folger Passage, the continental slope at Clayoquot slope and Barkley canyon, mid-plate at Cascadia basin, on the crest of the Endeavour segment of the Juan de Fuca ridge. The sixth site at middle valley is cabled for future development. Figure 2.8 represents the NEPTUNE network along with applications carried by each node.

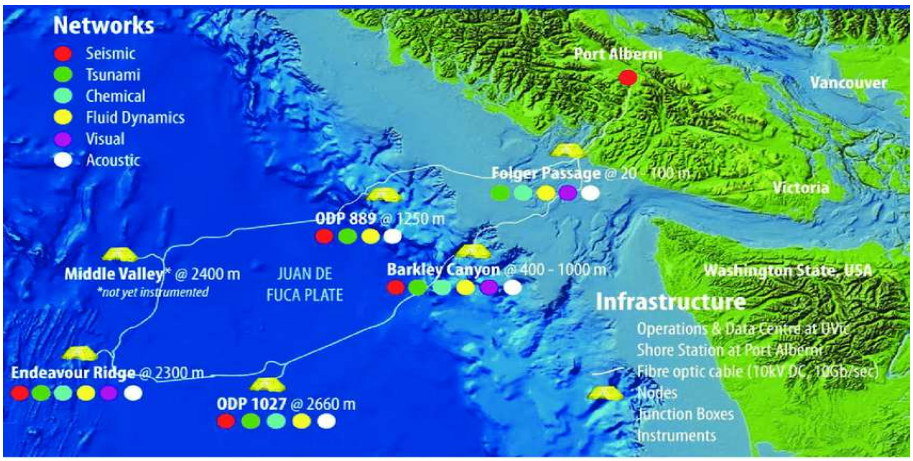

Figure 2.8: Pictorial representation of NEPTUNE network with applications [38]

1. **Folger Passage:**

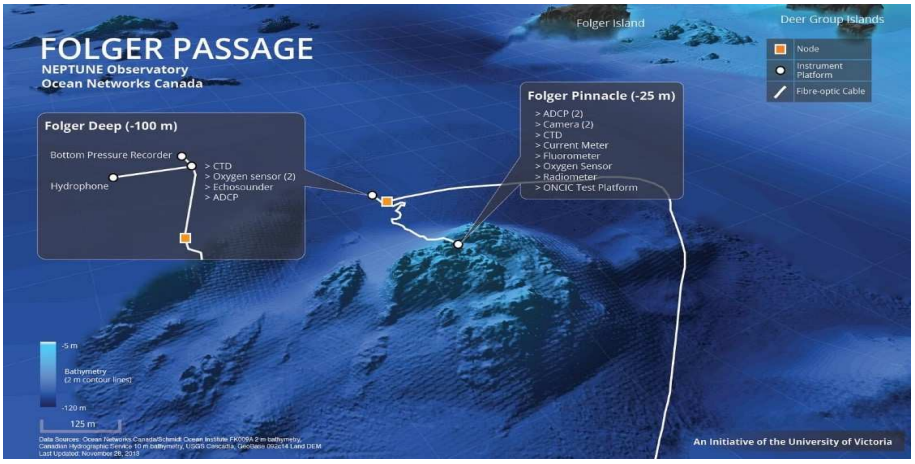

Figure 2.9: Pictorial representation of Folger passage [40]

Figure 2.9 shows the Folger Passage node. The Folger passage is located on the southwest coast of Vancouver Island. This node focuses on ocean biogeochemistry, terrestrial-marine interactions, coastal physical oceanography, phyto and zooplankton, fish, and marine mammals. The Folger passage consists of 2 instrument platforms: Folger deep (100 m) and Folger pinnacle (23 m) [40].

2. **Barkeley Canyon:**

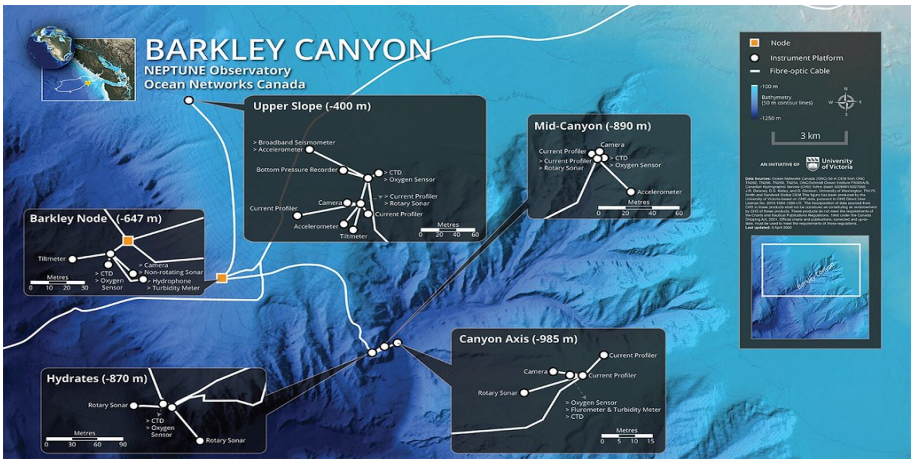

Figure 2.10: Pictorial representation of Barkeley canyon [41]

Barkley canyon is located at the leading edge of the Cascadia subduction zone as shown in Figure 2.10. The Barkley Canyon consists of 8 instrument platforms: Barkley canyon axis - Pod1 (985 m), Barkley Benthic Pod 2 (396 m), Barkley Benthic Pod 3 (890 m), Barkley Benthic Pod 4 (894 m), Barkley hydrates (870 m), Barkley upper slope (395 m), POGO vertical profiler ($0 - 396$ m), and Wally ($855 - 870$ m). The research in this site focuses on gas hydrate stability, sediment dynamics, upwelling on biological, ecological, and physical processes [41].

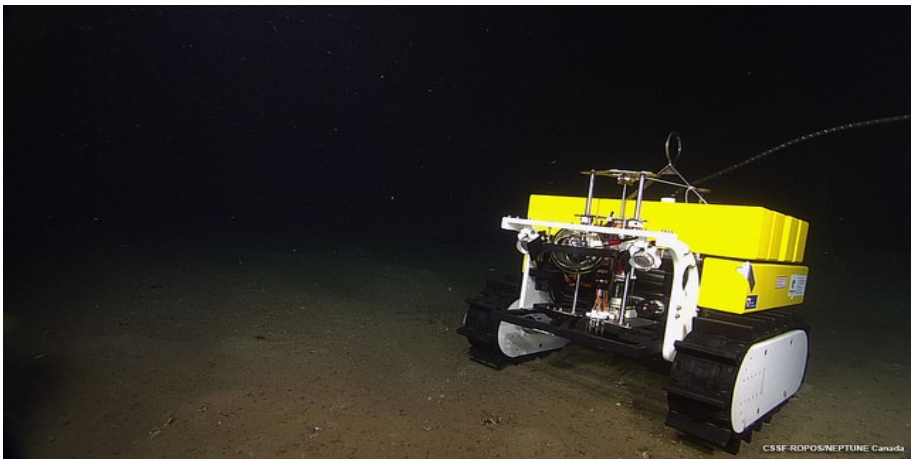

Figure 2.11: Pictorial representation of Wally the crawler [41]

Barkley canyon has a widest array of instruments, spread over the highest number (8) of instrument platforms on one node, with the two mobile platforms on the NEPTUNE observatory: Ocean Networks Canada's vertical profiler POGO and the world's first Internet operated deep-sea crawler, Wally the crawler [41]. Wally the crawler is shown in Figure 2.11.

3. **Cascadia Basin:**

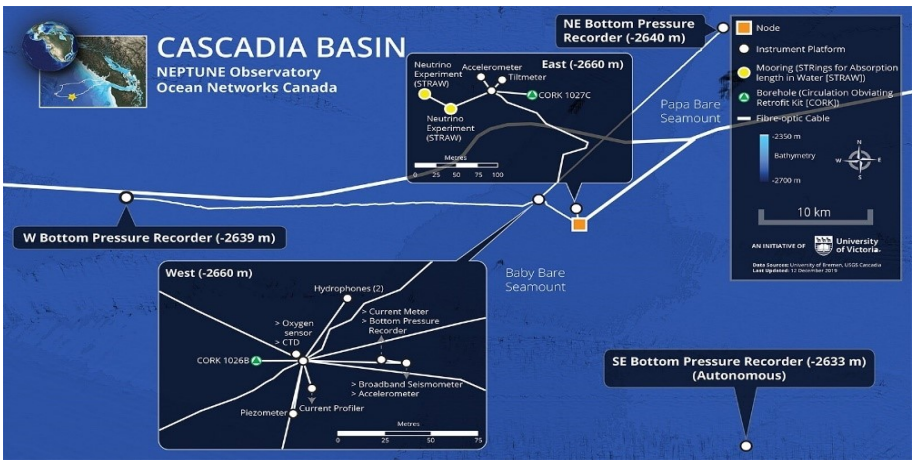

Figure 2.12: Pictorial representation of cascadia basin [42]

The Cascadia basin node is located at the center of the Cascadia basin, which extends from the base of the continental margin to the mid-ocean ridge at a depth of 2660 m as shown in Figure 2.12. Most of the research at the Cascadia basin observatory revolves around the physical sciences and seafloor stability [42]. A selection of the study includes:

- Seismograph network uses four broadband/strong-motion seismographs and four short-period seismographs to study subsea earthquakes and other tectonic activity
- Ocean crustal hydrogeology project utilizes boreholes drilled across the Juan de Fuca tectonic plate to help reveal the relationship between dynamic processes such as episodic plate motion, internal plate strain, and earthquakes
- West coast "Tsunami-Meter" studies the generation, propagation, transformation, run-up, and dissipation of tsunamis and other long waves.

4. **Endeavour:**

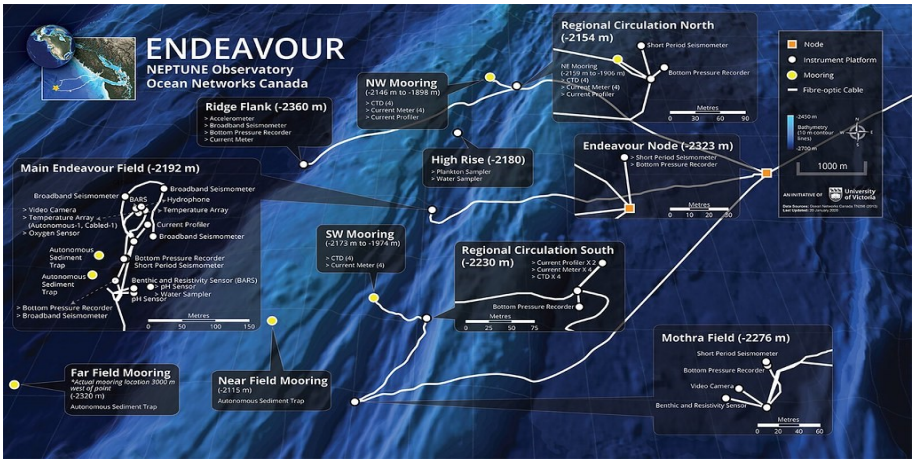

Figure 2.13: Pictorial representation of Endeavour [43]

Endeavour is located at the part of the complex mid-ocean ridge system along the

spreading seafloor boundary between the Juan de Fuca and Pacific tectonic plates. Endeavour is shown in Figure 2.13. It consists of 5 instrument platforms: Main Endeavour Vent Field (MEF) at a depth of 2192 m, NE and NW Regional Circulation Moorings (NE-RCM and NW-RCM) at a depth of 2158 m and 2138 m, North RCM Platform(N-RCMP) at a depth of 2154 m, and Tempo-Mini at a depth of 2186 m. The research in this site focuses on seismicity, volcanism, and hydrothermal vent system. [43].

5. **Clayoquot Slope:**

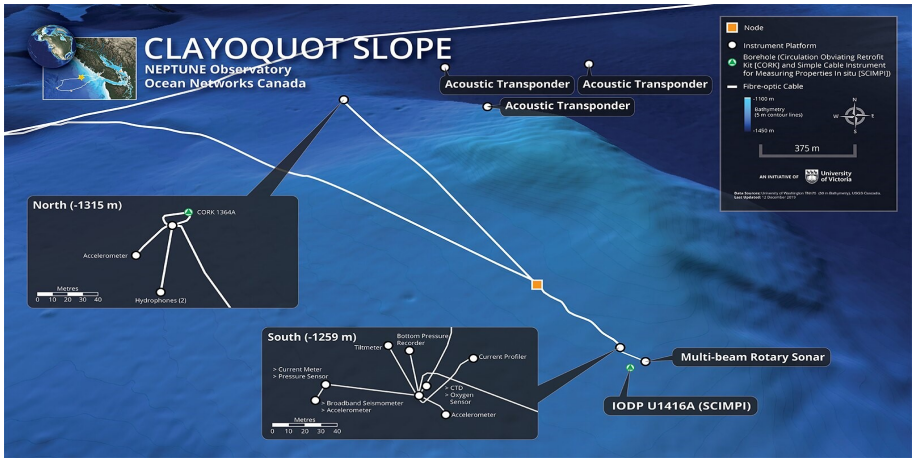

Figure 2.14: Pictorial representation of Clayoquot slope [44]

This site is located on the mid-continental slope off south-central Vancouver Island, about 20 km landward of the toe of the Cascadia subduction zone as shown in Figure 2.14. This site consists of one instrument platform at a depth of 1258 m. The principal research of this site focuses on seismicity, study on deep-sea organisms, seafloor fluids, and gases.

6. **Middle Valley:** This site is located at the northern end of the Juan de Fuca ridge but not yet instrumented. The installation node is planned to be placed at a depth of

2400 m.

2.1.3.2 Monterey Accelerated Research System (MARS)

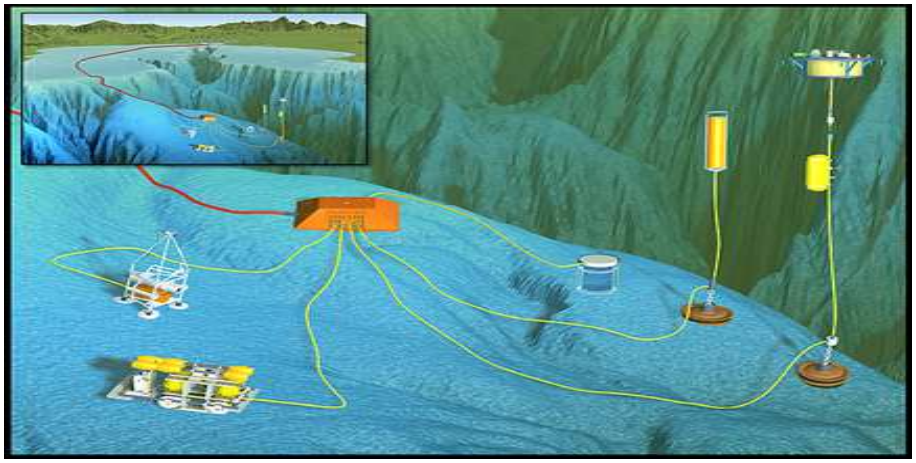

Figure 2.15: Pictorial representation of MARS network [45]

MARS network consists of 52 km underwater cable that carries data and power to the science node located at a depth of 891 m in Monterey Bay as shown in Figure 2.15. MARS observatory experimented with testing the robot. They use Long Range Autonomous Underwater Vehicle (LRAUV) for detecting and tracking oil spills. The MBARI engineers outfitted the LRAUV with the fluorometers to detect the presence of oil in water. They used a non-toxic, biodegradable dye for simulating the oil spill. This LRAUV/ Robot is placed in water, and then the robot goes in search of an oil plume. After the robot finds the plume, it measures the concentration of dye and records the areas of high intensity. If the robot reaches the plume's outer edge, it heads back to the plume and starts measuring the concentration of dye. By doing this repeatedly, the robot will be able to detect and track the plume [45].

2.1.3.3 Hawaii 2 Observatory (H2O):

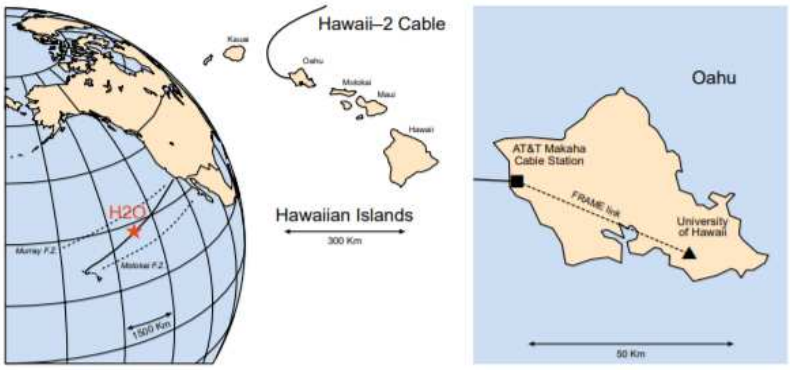

Figure 2.16: Pictorial representation of H2O observatory [46]

H2O is the first global seismographic network station on the seafloor with a suite of wet-mateable connectors on a junction box. This observatory is located between Oahu, Hawaii, and California coast at a depth of 5000 m as shown in Figure 2.16 [46].

2.1.3.4 European Seas Observatory NETwork (ESONET)

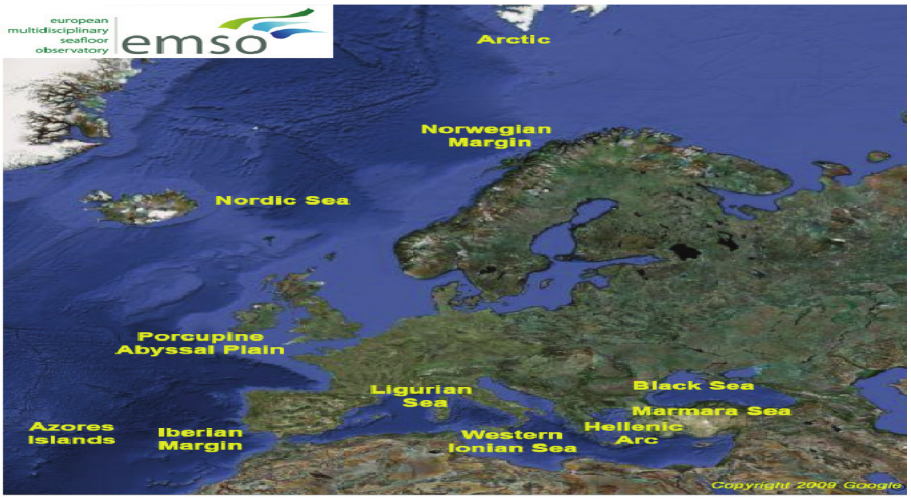

Figure 2.17: Pictorial representation of ESONET network [47]

European Seas Observatory NETwork (ESONET) aims to promote the implementation and the management of a network of long-term multidisciplinary ocean observatories in deep waters around Europe. The ESONET proposes a network of seafloor observatories around the european ocean margin, from the arctic sea to the black sea for long-term monitoring. The pictorial representation of ESONET is shown in Figure 2.17. The submarine terrain around Europe, from the continental shelves to 4000 m depth, is known as the European ocean margin. This area extends approximately 15000 km from the arctic ocean to the black sea and accounts for 3 $million\ km^2$. The network will have geophysics, geotechnics, chemistry, biochemistry, oceanography, biology, and fisheries. Ten initial areas for ESONET development have been identified, in addition to a mobile emergency response station. The locations for elements of ESONET are based broadly on three criteria: geohazards, global change and environmental monitoring [47].

1. **Arctic:**

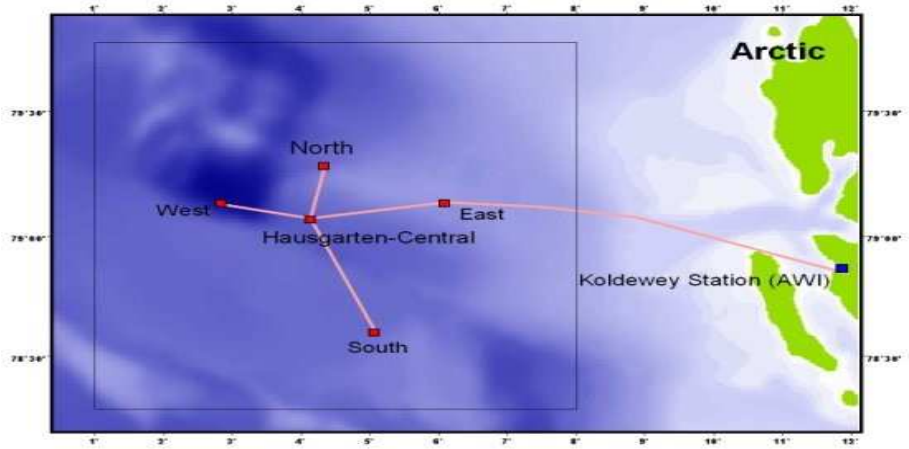

Figure 2.18: Pictorial representation of Arctic node [47]

The Arctic node is shown in Figure 2.18. Arctic water exiting into the Atlantic ocean between Europe and Greenland is an important component of the global deepwater

circulation of the planet and its heat budget. The establishment of a long-term station here is important for tracking global change as ice cover decreases. Still, there are also important deep-sea habitats such as mud volcanoes in the 'Hausgarten' region off Svalbard. The research in this area includes detecting unexpected changes of abiotic and biotic parameters governing global climate conditions.

2. **Norwegian Margin:**

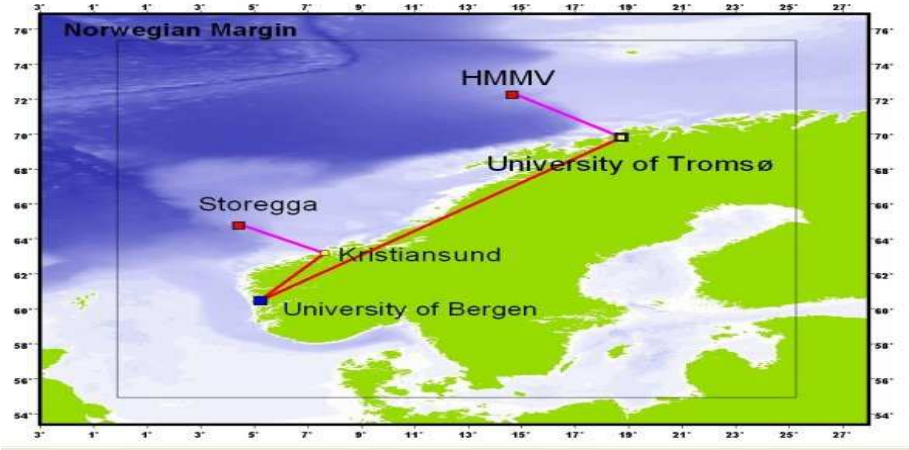

Figure 2.19: Pictorial representation of Norwegian margin [47]

The Norwegian margin region has shown slope instability with evidence of significant slides, which, if repeated, could result in catastrophic damage to offshore oil and gas installations as well as indirect effects of tsunamis striking the coasts of the British Isles and elsewhere. Two observatories are planned in this area, the first close to one of the largest deepwater gas fields in Europe (Ormen Lange at Storegga) and the second at the Barents sea margin at a submarine mud volcano (HMMV). This site measures the amount of fluid flow in and around these regions. Norwegian margin is shown in Figure 2.19.

3. **Nordic Sea:**

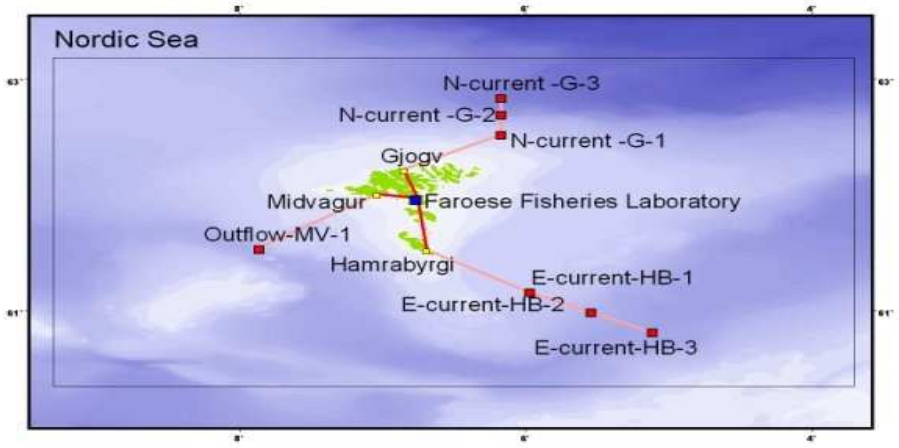

Figure 2.20: Pictorial representation of Nordic sea [47]

Nordic sea is shown in Figure 2.20. The MOEN (Meridional Overturning Exchange with the Nordic seas) station uses the Faroes branch of the CANTAT-3 cable for measuring water column induced voltage. The recorded voltage is strongly influenced by the inflow of the North Atlantic Current (NAC). Long term monitoring of this current is vital in understanding the oceanic fluxes of heat, salt and freshwater at high northern latitudes and their effect on global ocean circulation and climate change in the arctic region.

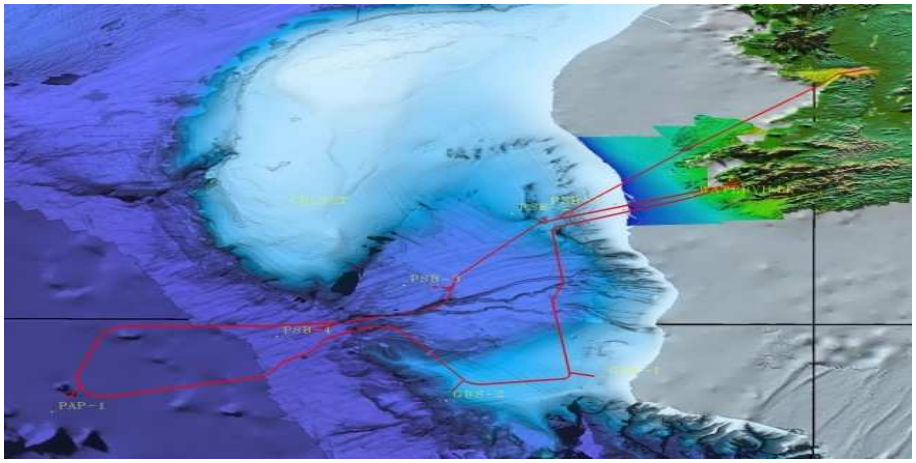

Figure 2.21: Pictorial representation of Porcupine seabight/Abyssal plain [47]

4. **Porcupine Seabight/Abyssal Plain:** The setup at Porcupine seabight is shown in Figure 2.21. Porcupine Sea bight and Abyssal Plain have been an important area for biogeochemical flux studies in the past but are also very productive fisheries and oil-gas exploration areas. It is a stable margin with little evidence of seismicity but does have critical deepwater habitats. This region focuses on the study of the coral reef ecosystem.

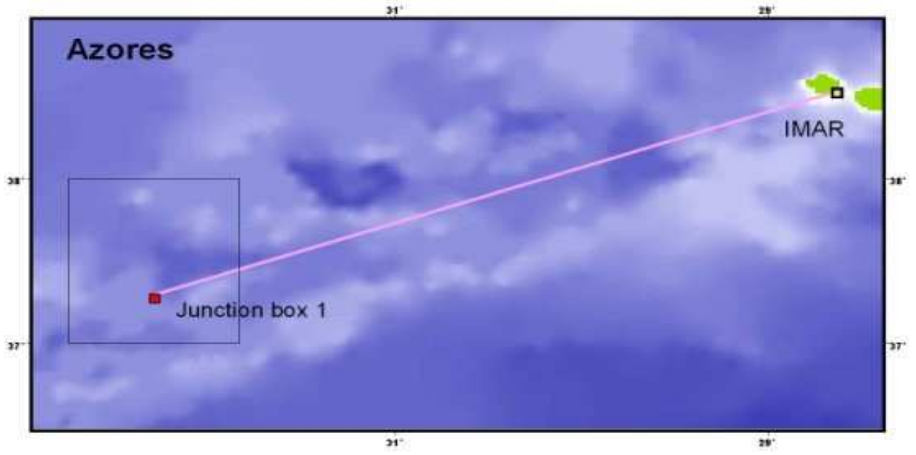

Figure 2.22: Pictorial representation of Azores mid-atlantic ridge [47]

5. **Azores Mid-Atlantic Ridge:**

   The Azores and mid-atlantic ridge area has unique habitats associated with hydrothermal vents and seafloor morphology. Scientific objectives of the MoMAR (Monitoring the Mid-Atlantic Ridge) project are studying the temporal variability in active processes such as hydrothermalism, ecosystem dynamics, volcanism, seismicity, and ground deformation. Azores mid-atlantic ridge is shown in Figure 2.22. This area extends over the Azores Islands and along the mid-atlantic ridge and offers a unique opportunity to monitor: biodiversity of marine ecosystems, the mid-atlantic ridge, volcanic seamounts, response to environmental change, sustainable management of fishing resources/ biodiversity, chemical, geological, and geophysical processes.

6. **Gulf of Cadiz-Iberian margin**

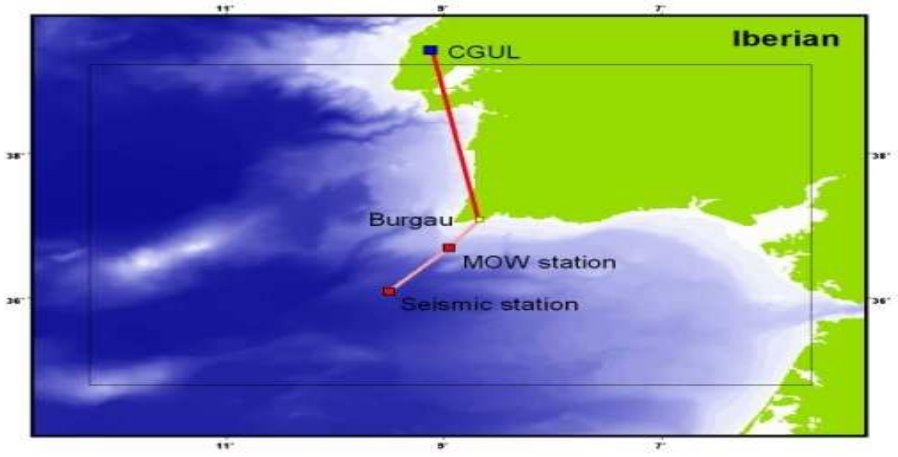

Figure 2.23: Pictorial representation of Iberian margin [47]

The Gulf of Cadiz/Iberian margin is a region of complexity with the junction of the Eurasian and African plates resulting in doming of the seafloor, mud volcanoes and other complex features. The interaction of the mediterranean outflow with Atlantic waters is significant. The Iberian region's main objective is to realize a seismic mon-

itoring network in the Gulf of Cadiz, providing an in-depth knowledge of the area's seismic activity and a capability in early detection of the tsunami. Iberian margin is shown in Figure 2.23.

7. **Ligurian Sea:**

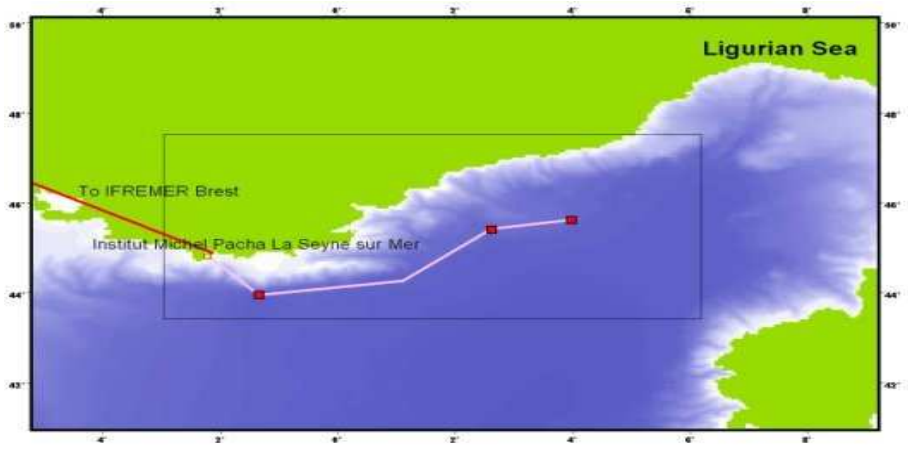

Figure 2.24: Pictorial representation of Ligurian sea [47]

This area has been monitored for a long time with a conventional cruise. The Ligurian sea is a broad multidisciplinary area of interest with many technical advantages for a demonstration observatory. This site includes the study of tidal currents.

8. **Sicily:** East Sicily is an important offshore site close to Mount Etna which is shown in Figure 2.25. The existing cable for the NEMO neutrino experiment focuses on real-time data transfer and the integration of the seafloor observatory into land-based networks. The Eastern Sicily node will be based on SN-1, a deep seafloor multi-parametric cabled to shore observatory. SN-1 mainly focuses on geophysical, oceanographic, and environmental data that are unique time referenced. Modular design allows additional sensors to be added as required.

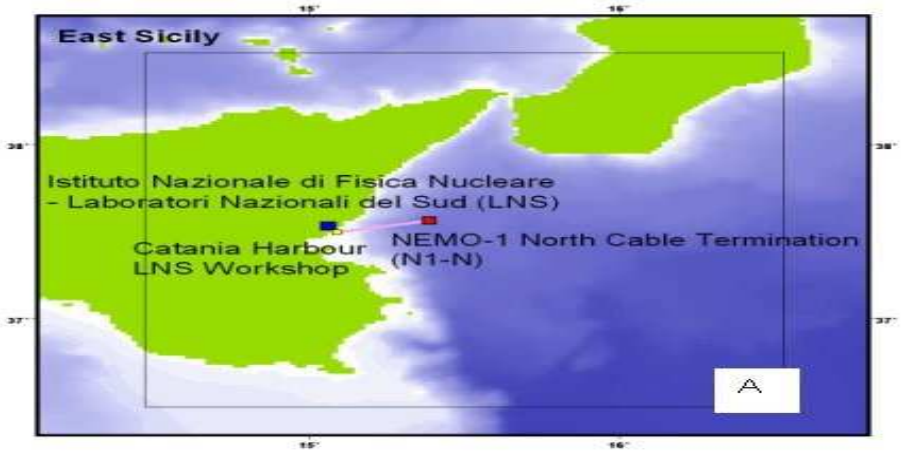

Figure 2.25: Pictorial representation of East Sicily [47]

9. **Hellenic Arc**

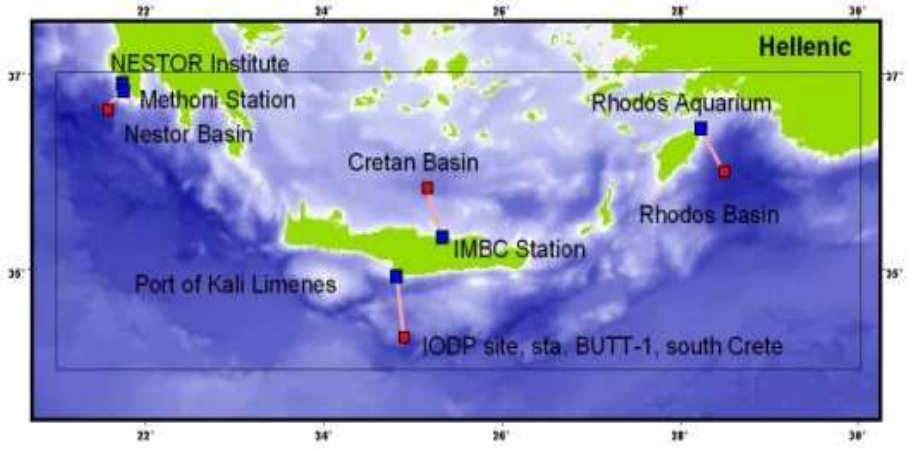

Figure 2.26: Pictorial representation of Hellenic arc [47]

The hellenic arc is shown in Figure 2.26. The eastern mediterranean is characterized by significant seismicity, unique habitats in deep basins and a very steep drop off from the coastlines. The Hellenic region comprises of four distinct networks: NESTOR (existing neutrino observatory cable), BUTT-1 (IODP – site of the proposed deep borehole), Cretan basin, and Rhodos basin. The overall aim of these stations is for the

long-term investigation of seafloor processes, to quantify slow versus fast fluid flow and carbon/methane fluxes, to develop long term monitoring observatories for the oil/gas industry, to carry out hydroacoustic studies on fluid flow pathways and mineral crusts in upper sediment layers, to link fluid, methane flow with tectonic movement and seismic activity, and to monitor the biology and ecology of the deep area.

10. **Black Sea:**

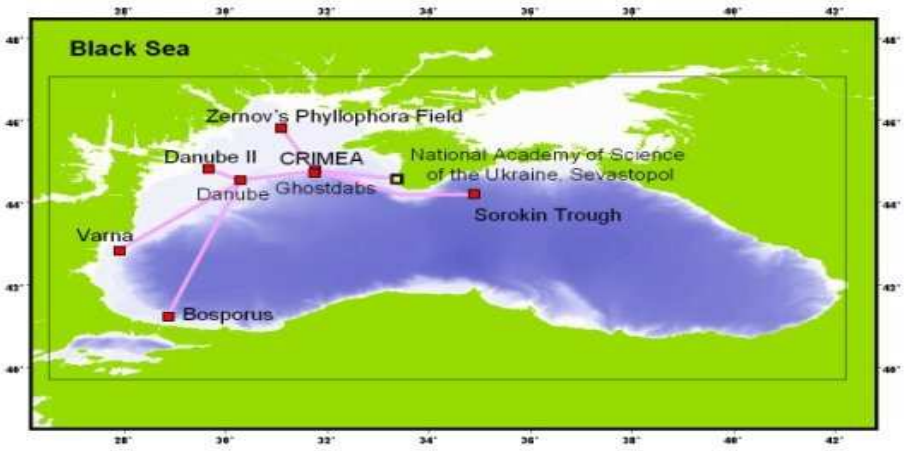

Figure 2.27: Pictorial representation of Black Sea [47]

Black sea is one of the most massive regional seas of the european continent and unique in its geographical, geological, biological, hydrographical and socio-political characteristics. With anoxic conditions in the deep, problems with invasive species and high sediment loads delivered to the system. The long-term cabled observatory will provide continuous data on high-intensity gas flares and environmental control parameters of gas and fluid discharge (e.g. bottom currents, microseismicity, earthquakes, gas hydrate stability, the role of mud volcanoes). Black sea setup is shown in Figure 2.27.

In the above section, we discussed underwater observatories and their applications in the marine environment. From the observatories mentioned above, VENUS observatory is located

in conditions similar to those in Newfoundland coast in terms of depth.

2.2 Underwater Modems

2.2.1 Underwater Optical Modems

As mentioned earlier, optical waves suffer from severe scattering due to water current and suspended particles in the seawater. Although optical waves are affected by diffusion, they can provide a higher data rate for a short communication range. The BlueComm is the high-speed underwater optical modem produced by Sonardyne [48]. This modem utilizes an array of high power light-emitting diodes to modulate optical signals for transmitting data. The BlueComm optical modem can reach a range of 20 m at a transmission rate of 5 Mb/s in shallow water. For deep water, which is over 350 m, this modem can transmit data at rates of up to 20 Mb/s for a range of 200 m. For real-time data transmissions, such as high definition videos or images, the BlueComm modem can be used to collect a large amount of data.

2.2.2 Underwater Acoustic Modems

Although acoustic communication poses challenges, it is the most commonly used communication solution for UWSNs. Underwater acoustic modems are used for commercial applications such as oil exploration, ocean observations, and natural resource development. WHOI developed a compact and low-power acoustic modem called micro-modem. Micro-modem can be employed in two different modulations: frequency-hopping frequency shift keying (FH/FSK) and phase-shift keying (PSK). FH/FSK modulation is used for shallow water communication with a low data rate of 80 b/s. In contrast, PSK modulation is used for deepwater communication with a high data rate of 5000 b/s.

AquaComm is an underwater acoustic modem used for the short-range communication produced by DSPComm [49]. The AquaComm modem can achieve a communication range of 3 km with a data rate of 100 or 480 b/s. The operation bandwidth is from 16 kHz to 30 kHz. The price of the AquaComm modem starts at $6000. A German-based company called Evologics produces six different acoustic modems based on a sweep-spread carrier, aiming to mitigate the multipath effect in the seawater. This type of acoustic modems provides self-adaptive algorithms for reliable acoustic communications.

Acoustic modems converts digital data into sound signals and transmits that signal to the other nodes in the topology network. The other nodes receives the transmitted signal and converts them back to digital data. If collaborative approach is used for receiving, the capabilities of propagation time and distance between transmitter and receiver can be exploited to support the synchronization and coordinated across multiple nodes. Modem 6 Sub-Mini is an underwater acoustic modem developed by Sonardyne based on 6G equipment which provides a reliable and cost-effective method for underwater wireless communications. This modem offers a depth rating of upto 1000 m. The specifications of this modem are given in Appendix A.

Table 2.1: Comparison of acoustic modems and optical modems

	Blue-Comm	Micro-modem	AquaComm	Evologics	Sonardyne
Modulation	N/A	FH-FSK/PSK	DSSS/OFDM	Sweep-Spread Carrier	
Data Rate (b/s)	$1 \times 10^6/20 \times 10^6$	80/5000	100/480	19200/31200	9000
Transmitting Power (W)	40	≤ 50	N/A	2.8/8/35	1
Receiving Power (W)	8	3	N/A	1.1	0.02 x 10^{-9}
Communication Range (m)	≤ 200	N/A	N/A	≤ 3500	1000-1500
Type of Modem	Optical	Acoustic	Acoustic	Acoustic	Acoustic

We present the five commercially available modems in terms of data rates, transmitting

power, receiving power, and communication range in Table 2.1.

2.3 Underwater Acoustic Channel Models

Acoustic Signals in the underwater environment suffer from severe attenuation, absorption, Doppler spread, and multipath propagation. To design protocols for the MAC layer and the network layer, it is necessary to understand the underwater acoustic channel models. Due to temporal and spatial variability, there is no agreement on the statistical characterization of underwater acoustic models. This section investigates a few shallow underwater acoustic channel models and the acoustic signal propagation properties in deep water.

2.3.1 Shallow Acoustic Channel Models

Naderi *et al.* developed a stochastic geometry-based channel model for wideband single-input single-output (SISO) shallow underwater acoustic (UWA) channels [50]. The authors derived the reference model, considering the scatterers are distributed randomly on the surface and the water bottom. They also analyzed the probability density function and the angle of arrival of the reference model.

Chitre investigated the shallow warm-water acoustic channel for the underwater communication environment with the two main characteristics, which include extensive time-varying multipath and non-Gaussian ambient noise [51]. The proposed channel model captures the multipath arrival structure and the statistical effects of acoustic signals such as fading and arrival time jitter. Stojanovic and Preisig present Rayleigh fading at 15 m water depth, which was verified for the horizontal communication ranges of 50 m, 100 m, and 1020 m. The author concludes that the time-correlation of acoustic channel is not affected, and thus short-distance communication in seawater is not affected. The derived channel model agrees

with the experimental data obtained from the sea trial conducted in Singapore [52].

The author studied the random channel variations and proposed the statistical underwater acoustic channel models by considering the frequency-dependant attenuation and bottom/surface reflections [53]. They classify the random channel variations into the small-scale and large-scale based on the wavelength size. The small-scale channel model includes scattering and motion-induced Doppler shifting, whereas the large-scale channel model has a lognormal distribution.

The experimental data collected from the TREX04 sea trial, non-Rayleigh or non- Rician distribution characteristics of acoustic channel models can be observed [54]. In the TREX04 trial, the depth of the water column was assumed to be 70 m, and the source and receiver are placed at a depth of 35 m. The data packets were transmitted over a horizontal distance of 3.4 km. Several conventional channel models fail to present non-Rayleigh or non-Rician distribution characteristics because all these models assume fading statistics as valid for all time scales. Yang *et al*. categorize the timescale fading phenomena into long-term and short-term based on a 0.2 s time scale obtained from the experimental data collected from the TREX04 sea trial [55]. For long-term fading statistics, a lognormal distribution was used, whereas Rayleigh distribution was used for short-term fading statistics. The authors studied the random channel variations and proposed the statistical underwater acoustic channel models by considering the frequency-dependant attenuation and bottom/surface reflections. They classify the random channel variations into the small scale and large scale based on the wavelength size. The small-scale channel model includes scattering and motion-induced Doppler shifting, whereas a large-scale channel model has a lognormal distribution.

2.3.2 Propagation Properties of Acoustic Signals in Deep Water

Acoustics propagation properties in deep water have been studied by conducting several sea trials in the past ten years. Udovydchenkov *et al.* concentrated on the sea-bottom reflection effect with a horizontal communication range of 50 km [56]. The depth of seawater considered in their experiment was 1.4 km. Using the experimental data collected from the long-range acoustic propagation experiment, the authors concluded that bottom- reflected acoustic signals are sensitive to ocean topography and its properties. The bottom-reflected acoustic signals interfere with refracted acoustic signals within the transmission range of bottom-reflected and surface-reflected acoustic signals. Furthermore, the seafloor was modelled as a fluid layer without scattering.

The oceanic experiment was conducted at a depth of 5000 m in Japan to evaluate multiuser communication performance in deep water [57]. The transmitters were deployed at depths of 2000 m, 2500 m, and 3000 m, respectively. The receiver arrays were placed at a depth of 1000 m. Adaptive time reversal with a single channel decision feedback equalizer is used to mitigate the potential data packets collision at the base station.

2.4 Oil Platforms

An oil platform is a massive structure built for drilling to explore, extract, store, and process petroleum and other gas that lies beneath the seabed. Though the oil platforms can also be used in lakes and inland seas, they are also engaged in the continental shelf activities. The oil platform can be fixed on the ocean floor or float on the ocean surface based on the circumstances. The offshore drilling process involves environmental challenges, from the hydrocarbons and the other materials produced during the drilling operation. The oil drilling platforms can operate in water depths of up to 3 km. The mobile platforms are

anchored to the seabed for shallow water, whereas, for the deep water, which is more than 1.5 km deep, the drillships or semi-submersibles are maintained using dynamic positioning. Notable offshore drilling fields include the north sea, California, Gulf of Mexico, arctic ocean, Atlantic Canada, and several areas of West Africa. In the following section, we discuss the different types of oil rig platforms.

2.4.1 Conventional Fixed Platform

A conventional fixed platform is a type of long-term offshore platform used to produce petroleum gas or oil. These platforms are built on steel or concrete legs, which are anchored directly onto the seabed. These legs support the deck with space for production facilities, drilling rigs, and crew quarters. Fixed platforms are suitable for water depths of up to 150 m.

2.4.2 Compliant towers

A compliant tower platform is a fixed rig structure used for the offshore production of gas or oil. This type of rig consists of narrow compliant towers with a piled foundation supporting the deck for drilling operations. Compliant tower platforms are suitable for the water depths of up to 450 m to 900 m. The most in-depth compliant tower platform is the Chevron Petronius tower, which is located at 623 m depth. Compared with other floating systems, such as tension-leg platforms and SPARs, the production risers in compliant towers are conventional.

2.4.3 Semi-Submersible Platform

Semi-Submersible platforms have hulls of sufficient buoyancy to make the platform structure to float [58]. This type of platform can be ballasted up or down by adjusting the buoyancy

tanks. It is suitable for the water depths between 60 m and 6000 m.

2.4.4 Jack-up drilling rigs

A jack-up rig is a type of mobile drilling platform with a buoyant hull, the detachable legs of which help raise the hull to the sea's surface. The buoyant hull is responsible for transportation and other attached machinery to the desired location. This type of rigs is not self-propelled, relying on tugs and heavy lift ships to transport the units. By the end of the year 2013, there were 540 operating jack-up drilling rigs. Noble Lloyd Noble is the tallest jack-up rig built so far with 214 m tall legs.

2.4.5 Drillships

A drillship is a maritime vessel fitted with drilling apparatus, which is most often used to explore new drilling oil or gas wells. In earlier days, the modified tanker hulls are used, whereas a purpose-built design is in use today. To maintain the well's position, the dynamic positioning systems are outfitted with the drillships that can drill in the water depth of up to 3700 m.

2.4.6 Tension-Leg Platforms

A tension-leg platform is a floating structure that is vertically moored and used for offshore oil or gas production. This type of platform is most suitable for the water depths greater than 300 m and less than 1500 m. The use of a tension-leg platform has been proposed for wind turbines. The platform is permanently moored using a group of tethers called tension-legs at each corner of the structure.

2.4.7 Gravity Based Structure

A gravity based structure is a platform structure which is held in a place by gravity. An offshore oil platform is a common application for the GBS. The GBS platforms are often built-in fjords because the depth of fjords is desirable and sufficient for the construction. The GBS, which is intended to use, is constructed with concrete tanks to control the buoyancy. After the completion of GBS, it is towed to the desired location and sunk in the water. The seabed information in the intended area is studied before the deployment to avoid unforeseeable circumstances. This structure can also be used for offshore wind power plants. These platforms are suitable for the water depth above 20 m. There are two Newfoundland-based GBS platforms: Hibernia and Hebron. Hibernia is located in the North Atlantic Ocean off the Jeanne d'Arc basin. Hebron is located off the coast of Newfoundland and is the fourth field to start production in the Jeanne d'Arc basin.

2.4.8 Spar Platforms

A Spar is a floating oil platform suitable for deep water, which is developed as an alternative for conventional platforms. These platforms are less prone to wind or water currents since these are in-depth water platforms that allow for both dry and subsea production. To support the deck, a spar platform consists of a single vertical cylinder weighted at the bottom with a chamber filled with particles that are less dense than water. The spar platform is classified into three types: classic, truss, and cells. The very first spar platform is the Neptune spar, which is located in the Gulf of Mexico. Perdido is the most in-depth truss spar platform located in the Gulf of Mexico at the water depth of about 2438 m.

2.5 Leak Detection Methods

In UWSNs, the oil leak is the leading cause of marine pollution, which affects the marine environment because of the presence of hydrocarbons in it. In long-term marine monitoring applications, pipelines are used for transferring petroleum products such as crude oil, fossil fuels, and gases. Pipeline failure is one of the significant causes of oil leaks in the underwater environment, which results in severe environmental disasters, financial loss, and human casualties. A practical approach to monitor the pipelines for timely detection of oil leaks should be developed to reduce the impact of pipeline breakage. Leak detection methods can be classified into internally-based, externally-based and visual-based. We present the advantages and disadvantages of currently deployed leak detection methods in Table 2.2

Table 2.2: Advantages and disadvantages of leak detection methods

Method	Advantages	Disadvantages
Acoustic Sensing	High sensitivity, real time monitoring, early and rapid detection of defects and reduced cost	Require examination to provide quantitative results
Fibre optic sensing	Light weight, small in size, offers dynamic range and large bandwidth	Expensive and detection systems are complex
Infrared thermography	Non-contact and non-destructive testing	Interpretation of results requires knowledge and experience
Vapour sampling	Detect small leaks	Time consuming
Mass-Volume Balance	Low cost and insensitive to noise interference	Dependent on leak size
Negative Pressure Waves	Fast response time	Only effective for large leaks
Dynamic Modelling	Handles large amount of data	High computational complexity

In this section, we survey different leak detection methods developed for the underwater environment.

2.5.1 Exterior Methods

Exterior leak detection methods involve sensing devices placed around the pipeline to monitor the outer part of the pipelines. Exterior methods are used to detect the abnormal activities happening around the pipelines to detect an oil leak. Some of the sensing devices in the external leak detection methods include acoustic sensing, fibre optic sensing, vapour sampling, and infrared thermography.

2.5.1.1 Acoustic Sensing

Acoustic emission sensors generate noise or vibration when there is a pressure drop because of the occurrence of a leak. Martini et al. proposed a method that produces elastic waves with a frequency of up to 1 MHz due to the pipeline breakage's high-pressure fluid [59]. Li *et al.* proposed an acoustic leak detection method that contains a set of sensors placed on the pipeline. The sensors emit the acoustic signals, and the time lag between the acoustic signals is used to determine the breakage position. Acoustic leak detection methods can be classified into active sensing and passive sensing. The active sensing method detects the presence of leaks by listening to the reflecting echoes generated by sound pulses, which is emitted as a result of leakage. In contrast, passive sensing detects leaks' presence by listening to the sound generated by the pressure waves in the pipeline. Several studies have been reported in the past years for using the acoustic emission sensors for detecting the leak from the pipeline breakage [60] [61] [62].

2.5.1.2 Fibre Optic Sensing

Fibre optic sensing method involves the installation of fibre optic sensors on the outer part of the pipelines. Fibre optic sensors can be installed in a distributed or point sensor to detect the physical and chemical properties of hydrocarbon spills from the pipelines. In fibre optic sensing, the temperature of the cable will vary if there is a pipeline breakage. Based on the variations in the fibre optic cable's temperature, the pipeline's leak position will be estimated [63]. Tanimola and Hill presented different leak detection methods based on the frequency of optical signals using distributed optical fibre sensors [64]. Fibre optic sensors can detect small pipeline leaks. In the past decade, several pipeline leakage detection methods have been proposed using fibre-optic sensors [65] [66] [67] [68]. Du *et al.* reported the effectiveness of using distributed optical fibre for pipeline leak detection [69].

2.5.1.3 Vapour Sampling

Vapour sampling determines the degree of hydrocarbon vapour in the pipeline environment. Oil spills from the pipeline breakage can be determined by measuring the gas concentration as a pumping time [70]. Different types of vapour sampling for detecting the presence of oil leakage was proposed in recent years [71] [72]. Vapour sampling includes some advantages: detection of small leaks, independent of pressure, and flow balance [73].

2.5.1.4 Infrared Thermography

Infrared thermography uses the infrared image-based technique for detecting the temperature changes around the pipeline area using infrared cameras. The image captured by infrared cameras is referred to as a thermogram. Thermography is classified into active thermography and passive thermography. The active thermography area includes background thermal contrast, whereas passive thermography has temperature variation [74].

2.5.2 Visual/Biological Methods

Visual/Biological leak detection methods are the traditional way of detecting oil leaks around the pipelines using trained dogs, personnel, smart pigging, drones, or helicopters [75]. This method requires trained personnel to walk along the pipelines to identify the abnormal conditions around the pipeline. The trained personnel observe the smelling odour coming out from the pipeline cracks. Trained dogs and smart PIG (Pipeline Inspection Gauges) method works in the same way as trained personnel. Smart pigging includes sensors and data recording devices such as optical cameras or video sensors for recording the event. Trained dogs can detect the odour more effectively than human personnel and smart pigging [76] [77]. These inspection methods can be applied only to onshore pipeline activities and offshore shallow pipeline activities. The detection time is based on the frequency of inspections since this detection method involves on-site inspection methods [71].

In addition to trained dogs, personnel, and smart pigging, ROVs came into existence. Later, AUVs were introduced, which reduced the extent of human operation through its intelligent control machinery [78]. AUVs and ROVs are available for inspecting subsea pipelines, but these vehicles are expensive. On the other hand, they are more suitable for monitoring remote and hazardous environments [79].

2.5.3 Interior/Computational Based Methods

Interior or computational leak detection methods require internal fluid measurement instruments to measure fluid flow inside the pipeline. This measuring instrument monitors the status of products inside the pipeline in terms of temperature, pressure, flow rate, and other parameters to characterize the released products. Some of the interior leak detection methods include mass-volume balance, negative pressure waves, and dynamic modelling.

2.5.3.1 Mass-volume Balance

This method is quite a straightforward approach for detecting the leak based on the principle of mass conservation. The inflow and outflow fluid in the pipeline is monitored, which should be balanced in case of no leak, or else it will provide a discrepancy between the measured mass and volume [80] [81].

2.5.3.2 Negative Pressure Waves

The negative pressure wave leak detection method is the widely used method for pipeline monitoring because of its fast response time and ability to localize the leak. This method utilizes the alteration in pressure and decreases in the flow speed when the leak occurs [82].

2.5.3.3 Dynamic Modelling

Dynamic modelling leak detection methods are used for detecting a leak in both the surface and subsea pipelines. Dynamic modelling involves detecting a leak from two different points: a statistical point of view and a transient perspective [83]. The transient leak detection technique is the most complex pipeline detection technique which requires the formulation of a mathematical model using fluid flow equations.

2.6 Underwater Localization

Localization of targets such as tracking ships, icebergs, the oil spill is essential in UWSNs because it helps to take several measures to avoid adverse consequences. Yashwanth *et al.* proposed a localization technique that involves a recursive positioning system with distinct sensor nodes [84]. UWSNs can help to monitor and control oil rigs to prevent disastrous effects in the marine environment. Park *et al.* suggested a model that utilizes electromag-

netic waves in water [85]. Kim *et al.* proposed a $3D$ localization algorithm for maritime surveillance that uses tiny beacons for localization [86]. Unlike WSNs, GPS cannot work appropriately in UWSNs because of high attenuation. Usually, underwater devices are more expensive, which makes the process of localization more challenging. Zhou *et al.* proposed a new localization technique for large-scale UWSNs to predict mobility of the sensor nodes. Anchor nodes conduct linear prediction by considering the benefits of the inherent temporal correlation [87]. In the following subsections, we discuss localization techniques and localization algorithms.

2.6.1 Localization Techniques

The localization techniques can be categorized into centralized and distributed localization. Centralized and distributed localization techniques can be sub-classified into prediction-based localization and estimation-based localization. In estimation-based localization, the available information is used to obtain the current position of the sensor node. In prediction-based localization, information about previous location, distance, and anchor location is used to predict the location of sensor nodes.

2.6.1.1 Distributed Localization

Distributed localization allows each sensor node to locate separately instead of depending on the central node to find the position of other sensor nodes. In distributed localization, the sensor nodes in the network communicate through peer-to-peer communication. Estimated-based distributed localization includes AUV-aided localization (AAL), silent localization (SL), dive and rise localization (DNRL), and proxy localization (PL). prediction-based distributed localization included scalable localization with mobility prediction (SLMP). The SLMP localization technique uses surface buoys and anchor nodes.

2.6.1.2 Centralized Localization

In a centralized location technique, the central node calculates each sensor node's position because the position of sensor nodes is not known *a priori*. Estimation-based centralized location includes hyperbola-based localization, motion aware self-localization, 3D multipower area localization and area-based localization. Janik *et al.* proposed a two-dimensional localization method based on a hyperbola, which identifies the sound source's location using hydrophones [88]. Bian *et al.* present an alternate approach for better localization accuracy using a hyperbola-based strategy to detect the event's place [89]. Mirza and Schurgers proposed motion aware self-localization to model the ocean currents, variable velocity, and the sensor movement [90]. Chandrasekhar *et al.* proposed an area localization scheme different from the motion-aware self-localization technique, combining the anchor node and a variable rate of transmission energy [91]. Area-based localization provides the estimation of the sensor node's location instead of precise coordinates. Cheng *et al.* propose a range-free and centralized localization algorithm. Prediction-based localization includes a collaborative localization technique for estimating the position of the sensor node [92]. Mirza *et al.* proposed a cooperative scheme that considers the sensor nodes to gather ocean depth information. The collaboration localization includes time-synchronization protocol evaluated using maximum likelihood, time of arrival (ToA), and distance of arrival (DoA) [90].

2.6.2 Localization Algorithms

Localization algorithms can be classified into range-based algorithms and range-free algorithms.

2.6.2.1 Range based Algorithms

The range-based algorithm is based on accurate estimation of distance or angle measurement. This algorithm estimates distance and angle using TDoA, ToA, and AoA calculations. Guo et al. present the ToA based algorithm for locating the position of the target [93]. ToA is the measurement of arrival time for distance estimation. The most frequently used technique for underwater localization is the ToA algorithm. ToA is mostly implemented in the underwater environment, although ToA needs synchronization among nodes. Because of time-varying characteristics, the received signal strength indication is not convenient. TDoA involves arrival time difference and is measured based on the time difference between the transmission medium and the receiver. Synchronous localization is estimated using the TDoA algorithm, which does not rely on the transmitter's starting time. Diamant and Lampe define a sequential method for localization in the underwater acoustic channel [94].

1. **Time Difference of Arrival (TDOA):**

   An asynchronous ToA-based localization method is used, in which the transmission source time is unknown, and ToA measurements have a favourable prejudice due to the synchronization mistake, which can lead to a big localization mistake. One method uses TDoA-based measures to fix this issue, which does not rely on a transmitter's transmission time [95] [96]. Since GPS signals are attenuating underwater, it is necessary to develop a precise range-based algorithm for locating underwater. The authors define a sequential method for time synchronization and localization in the acoustic channel [94]. Authors consider a realistic situation in which nodes are not time-synchronized, and underwater sound speed is also unknown, validating as two linear estimation issues. The authors define a new sequential algorithm in underwater for joint time synchronization and location. This method is based on exchanging information between the anchor and static nodes, using the directional navigation algorithm

used in nodes to achieve precise short-term estimates of movement and using continuous nodes. This method performs an accurate localization environment is utilizing only two anchor sensor nodes and exceeds the benchmark systems when node synchronization and propagation speed data are unknown.

2. **Time of Arrival (ToA):**

   In the ToA-based algorithm, the target must be symmetric with or sensor nodes. The author's proposed a new model called ToA-Based Tracked Synchronization (ToA-TS) that expands GPS as localization [97]. The beacon transmits a signal that includes the beacon data gathered from GPS and the time stamp that represents the time it was sent based on worldwide time. The receiving time of the message is saved according to the submersible's local clock on the receiver's hand. The investigator introduces a hybrid localization algorithm for Time-of-Flight (ToF) and Direction-of-Arrival (DoA), which is desirable in the setting of external underwater control applications and harbour monitoring operations. ToF measurements are performed by calculating the propagation time between the reference antenna and an antenna array. The DoA measurement is performed by evaluating the signal touching the DoA angle on the antenna array. For real-time positioning, a suitable low overhead monitoring method for portable underwater networks measures vehicle location in real-time circumstances where nodes follow predictable paths [98]. The localization efficiency can be improved by strategically positioning beacons. A joint localization and time synchronization considers the underwater environment's stratification. Authors investigate the issue of locating an underwater sensor node based on message broadcasting from ground nodes.

3. **Angle of Arrival (AoA):**

   AoA is an orientation and distributed localization algorithm that assumes that all

sensor nodes can detect incident signal angles of nearby sensor nodes [99] [100]. This algorithm is intended under the assumption of noisy angle estimation. Using the capability of AoA, the axis of nearby nodes for each node bearing can be identified. The data processing algorithm is described, and its outcomes are analyzed from information collected in two distinct structures. A model based on the measurement consequence is suggested in the clustered double Poisson ToA model. In the time-angle indoor multipath data, a proper clustering shape was determined. The collected information maintains the temporal clustering, and the angle clustering shape has been found. The mean angle of each cluster was chosen to be split evenly over all angles.

4. **Received Signal Strength Indicator (RSSI):**

   The signal power mostly depends on the radio wave propagation path loss impact. Suppose there is an obstacle between the sources of transmitter and receiver. In that case, the signal power can fall considerably on the respective obstructed connection, which is degrading the range estimate for precision [101] [102]. The author suggested an RSS-based localization algorithm based on Maximum Likelihood Estimation (MLE) for obstructed fields with unknown Path Loss Exponent (PLE). An RSS-based localization was implemented for underwater sensor networks using acoustic communication [103]. A new implementation of the Lambert function is suggested for an underwater range estimation based on RSS. It is demonstrated that the derived mathematical equation can calculate precise distance using four iterations of the Lambert function [104]. The author provided an RSS-based underwater localization algorithm with stratification compensation (NRA-WSE). One of the fundamental problems in the underwater environment is to determine the location of the detectors, which is achieved by evaluating the distance between anchor nodes and unknown sensor nodes. The ranging algorithms are performed by either assessing the ToA signal or RSS signal.

2.6.2.2 Range-free Algorithms

For range-free localization algorithms, we do not need to use various bearing information. This algorithm only provides a coarse estimation of the node of the sensor position that is distinct from the range-based algorithm [105]. The sensor nodes in the topology network are divided into multistage nodes for range-free algorithm and each stage has a distinct localization operation. Both range-based and range-free algorithms are used to enhance the precision of localization and decrease the cost of communication. This algorithm does not require any previous understanding of the velocity of motion that is used in an underwater environment. The range-free algorithm is categorized into the hop count-based, area-based algorithm, and centroid algorithms.

1. **Hop count-based algorithms**

   The anchor sensor nodes are placed along with the boundaries or corners of a square grid in the hop count-based algorithm. This algorithm is classified into solid positioning algorithm, DHL and DV-Hope algorithm. For estimating the distance to the anchor node, the DV-Hope algorithm utilizes an average estimation of the spectrum of hope and the counted number of hops [106]. A solid positioning algorithm is used to raise DV-Hop by inserting an extra refinement step, whereas the DHL algorithm may use density consciousness to estimate distance dynamically. For actual deployments, DHL has been recommended to improve position estimation accuracy when the distribution of nodes in the network is not uniform.

2. **Area-based algorithm:**

   Area-based algorithm can be classified into Area-Based Localization Scheme (ALS) and approximate point in a triangle (APIT). ALS is a centralized range-free system whose primary benefits are the resistance and simplicity underwater to the variable sound

speed. They can measure the location of a sensor node within a specific functional area. The clock of the sensor node must be synchronized in time. For instance, the 3D multipower area localization scheme (3D-MALS) extends 2D-ALS to 3D, whereas APIT requires a heterogeneous network [107]. Anchors are eqipped with high-power transmitters and can accurately acquire location data using GPS coordinates. Wang et al. used a new technique based on Mel Frequency Cepstral Coefficients (MFCCs). A nonlinear algorithm is required because underwater acoustic method is nonlinear and very hard to evaluate. MFCC is an efficient recognition and extraction algorithm.

3. **Centroid algorithm:**

   The centroid algorithm is a localization algorithm based on proximity and coarse-grained range-free. The disadvantage of the centroid localization algorithm is the high localization error because of the centroid formula. For the three-dimensional network application, the centroid algorithm focusing on a node's self-localization may not be suitable. A three-dimensional underwater localization algorithm utilizes three floating buoys on the ground called anchor nodes that are fixed with RF, GPS and acoustic transceivers [108]. The number of underwater sensor are installed at different depths. These can be fitted on the surface of the water with floating buoys and anchored to the bottom of the ocean. These sensor nodes have restricted capacity for movement and are referred to as semi-stationary nodes.

2.7 Terms used in this thesis

The terms used in the subsequent chapters are defined below:

- Source node: A sensor node that transmits the acoustic signal
- Receiver nodes: All the sensor nodes except the source node

- Topology: A set of sensor nodes arranged either in a square grid or concentric hexagons
- Observatory: It consists of a node with sensors, buoy profiling, shore station, and other instruments for long-term monitoring of the underwater environment.

2.8 Summary

In this chapter, we described different underwater observatories and their applications. Most of the underwater observatories presented in this thesis are cabled which is used for several underwater applications. We use untethered topology network for detecting oil leak in the underwater environment. We compared different underwater acoustic modems and an underwater optical modem used for commercial and academic purposes. We presented shallow acoustic channel models and the propagation properties of acoustic signals in deep water. Different types of oil rig platforms built for the production of oil or gas are also reviewed. There are many oil rig platforms already deployed and producing oil. We focussed on Hibernia oil rig platforms and chose the parameters such as depth and diameter of the caisson based on this platform. Different leak detection technologies for UWSNs were investigated. Additionally, different localization techniques which may vary based on application requirements are reviewed.

Chapter 3

Acoustic Properties and Channel Modelling

This chapter investigates the propagation characteristics of acoustic signals with different types of transmission loss in seawater to explore and develop the UWSNs. The propagation properties of acoustic signals in the marine environment have been researched in the past decades to gain a better understanding of acoustic communications. Several acoustic models have been used to study the underwater acoustic channels by considering Doppler spread, noise, attenuation, sound speed, and multipath propagation. Sound in the marine environment is characterized by noise, transmission loss, temporal and spatial variability of the channel. The transmission loss and the noise are the principal factors for determining the available bandwidth, transmission range, and signal-to-noise (SNR) ratio. Acoustic propagation models have different strengths and limitations because of the time-varying and space-varying nature of the underwater acoustic channels. First, we describe the properties of acoustic signal propagation in seawater that we plan to use in the following chapters. We utilize the semi-empirical formula for estimating the absorption loss of sound in seawater. We then discuss transmission loss and present expressions for other signal properties.

3.1 Propagation Properties of Acoustic Signals

In this section, we present the sound speed profile, absorption loss of sound, and the principal transmission loss, which are the basic propagation properties of the acoustic wave in the underwater environment. We then present the expression for calculating the power, intensity, time of arrival (ToA), and the angle of arrival (AoA) of the acoustic signal.

3.1.1 Sound Speed Profile

The velocity of sound in the sea is the important oceanographic parameters that determine the behaviour of sound transmission in the underwater environment. The density fluctuations can influence the propagation of acoustic signals, but these fluctuations are negligibly small compared to the sound speed in seawater. The nominal value for the speed of sound in the ocean is 1500 m/s, but the precise value for the sound speed depends on temperature, salinity, and pressure (or depth) of the entire ocean column. Several empirical formulas were developed to calculate the speed of sound in seawater with respect to temperature, salinity, and pressure (or depth). The three simple and commonly used expressions for sound velocity is mentioned below [16].

Leroy *et al.* proposed a new equation for calculating sound speed in seawater as a function of temperature, salinity, depth, and latitude in all oceans and open seas. The proposed equation is given by [109]:

$$\begin{aligned} c = 1402.5 + 5T - 5.44 \times 10^{-2}T^2 + 2.1 \times 10^{-4}T^3 + 1.33S - 1.23 \times 10^{-2}ST + 8.7 \times 10^{-5}ST^2 \\ +1.56 \times 10^{-2}Z + 2.55 \times 10^{-7}Z^2 - 7.3 \times 10^{-12}Z^3 + 1.2 \times 10^{-6}Z\big(\phi - 45\big) \\ -9.5 \times 10^{-13}TZ^3 + 3 \times 10^{-7}T^2Z + 1.43 \times 10^{-5}SZ \end{aligned} \tag{3.1}$$

Equation 3.1 is a pure polynomial form with 14 terms and coeefficients of only one to three significant figures. Leroy *et al.* performed substantial simplication of Equation 3.1 using Leroy-Parthiot algorithm to transform depth into pressure. The simplified equation in terms of T, S, and D in the ranges -2 $\leq T \leq 25^o$, 30 $\leq S \leq$ 42 ppt, 0 $\leq D \leq$ 1000 m is given by:

$$c = 1492.9 + 3\big(T-10\big) - 0.006\big(T-10\big)^2 - 0.04\big(T-18\big)^2 + 1.2\big(S-35\big) \tag{3.2}$$

Medwin *et al.* proposed a simple equation with the realistic combination of T, S, and D in the ranges $0 \leq T \leq 35^o$, $0 \leq S \leq 45$ ppt, and $0 \leq D \leq 1000$ m. The equation is given by [110]:

$$c = 1449.2 + 4.6T - 0.055T^2 + 0.00029T^3 + \big(1.34 - 0.01T\big)\big(S-35\big) + 0.016D. \tag{3.3}$$

Mackenzie proposed a simple empirical expression for the speed of the sound in terms of T, S, and D with the range $0 \leq T \leq 30^o$, $30 \leq S \leq 40$ ppt, and $0 \leq D \leq 8000$ m. The proposed nine-term equation is given by [111]:

$$\begin{aligned} c = 1448.96 + 4.591T - 0.05304T^2 + 0.0002374T^3 + 1.340\big(S-35\big) + 0.01630D \\ +0.0000001675D^2 - 0.01025T\big(S-35\big) - 0.0000000000007139TD^3. \end{aligned} \tag{3.4}$$

In Equation 3.1, Equation 3.2, Equation 3.3, and Equation 3.4 ϕ is the latitude, Z is the depth measured in terms of m, c is the speed of the sound in seawater measured in terms of m/s, T is the temperature of the seawater measured in terms of °C, S is the salinity measured in terms of ppt, and D is the depth of the seawater measured in terms of m. From the three simple and most commonly used expressions for sound velocity, we utilize the expression proposed by Leroy *et al.* in our work [109]. We consider the depth of the water column as 80 m for our work. The expression for sound velocity proposed by Leroy *et al* is applicable for the depth of 0 to 1000 m. Because of this, we utilize this expression throughout our work.

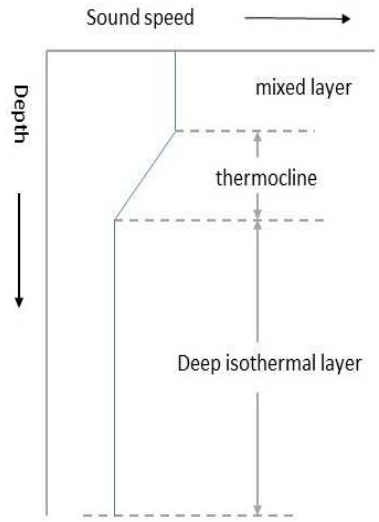

Figure 3.1: Relationship between sound speed and temperature [16]

The sound speed profile can be divided into three layers: a mixed layer, thermocline layer, and deep isothermal layer associated with different temperature distributions as shown in Figure 3.1. The sonic layer is below the ocean surface, which is generally associated with the mixed layer [15] [17]. In this mixed layer, the speed of the sound increases with depth under uniform temperature. The sound's speed can also be affected by heating, cooling, or the action of wind. When the sound wave travels in the opposite direction with the wind, the speed of the sound will be reduced by the wind speed which results is lower speed in the upper region. The upward refraction of sound in this layer keeps the acoustic energy concentrated near the ocean surface, making the sound propagate over long distances [16]. The layer below the mixed layer is the thermocline layer, where the speed of the sound decreases with depth because of the decrease in the temperature of the water. The layer below the thermocline layer, which extends to the seafloor, is called a deep isothermal layer. In this layer, the temperature of the water remains stable. The speed of the sound in this layer increases with depth because the water pressure becomes linear with a positive gradient.

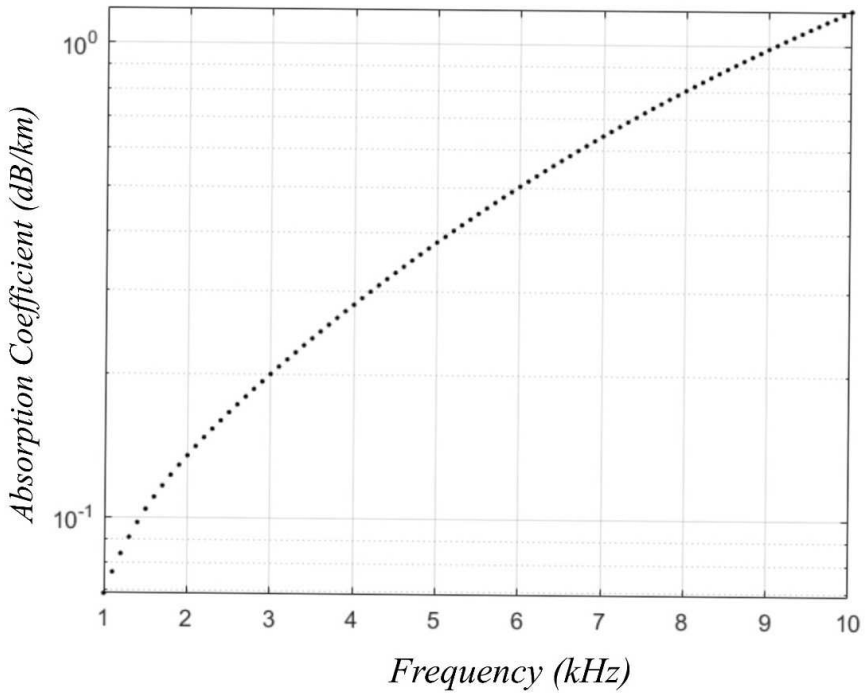

Figure 3.2: Absorption coefficient of acoustic signal in seawater [16]

3.1.2 Absorption Loss

The signal attenuation in the seawater includes absorption, diffraction, scattering, and duct leakage. Absorption loss is considered as the primary source of attenuation of sound signals in an underwater environment. The absorption of sound in seawater is high compared to the absorption of sound in pure water. Researchers proposed different empirical formulas to describe absorption loss. Early measurements for absorption coefficient of seawater were made from 1931 to 1934 by Stephenson using sinusoidal pulses. These pulses are transmitted through seawater between the surface ship and a submarine. The simple frequency dependent (f in kHz) and efficient formula for measuring absorption of sound in seawater was proposed by Thorp in 1967 [16] [17].

$$a_{water}(f) = \frac{0.11f^2}{1+f^2} + \frac{44f^2}{4100+f^2} + 2.75 \times 10^{-4} f^2 + 0.003, \tag{3.5}$$

where f is the frequency of the sound in kHz, and $a_{water}(f)$ is the absorption coefficient of sound signal in seawater (dB/km). Figure 3.2 shows the graph of the absorption coefficient of sound in seawater plotted using Thorp's formula. The constant 0.003 in this expression is added to work for very low frequencies at 100 Hz – 3 kHz. Since, the empirical formula for absorption coefficient of sound in seawater works well even for the low frequencies, we utilize this expression for the frequency of 10 kHz for our work. The first two terms in the formula represent the absorption of sound due to the relaxation of boric acid H_3BO_3 and $MgSO_4$ in seawater. The proposed formula is applicable for the temperature of 4^oC with a depth of about 900 m. This formula is sufficiently accurate for most of the problems in the underwater acoustic environment.

Since our research concentrates on the detection of an oil leak, it is essential to estimate the acoustic properties of sound in oil. Thorp's formula for determining the absorption coefficient of sound in seawater is not applicable for other liquids because of the varying density and speed of the sound in other liquids. Stokes' proposed a formula for estimating the absorption of sound in fluids by considering the structural relaxation [112].

$$a_{oil}(f) = \frac{\omega^2}{2\rho_{oil}c_{oil}^3}\left(\frac{4}{3}\mu_s + \mu_B\right), \tag{3.6}$$

where ω is the angular frequency in kHz, f is the frequency of the sound in kHz, ρ_{oil} is the density of oil, c_{oil} is the speed of sound in oil, μ_s is the shear viscosity of oil, μ_B is the bulk viscosity of oil and $a_{oil}(f)$ is the absorption coefficient of sound signal in oil (dB/km). The values of these parameters are given in Chapter 4. Figure 3.3 shows the graph of the absorption coefficient of sound in oil plotted using Stokes' formula. From Figure 3.2 and Figure 3.3, it is evident that oil absorbs less sound compared to seawater.

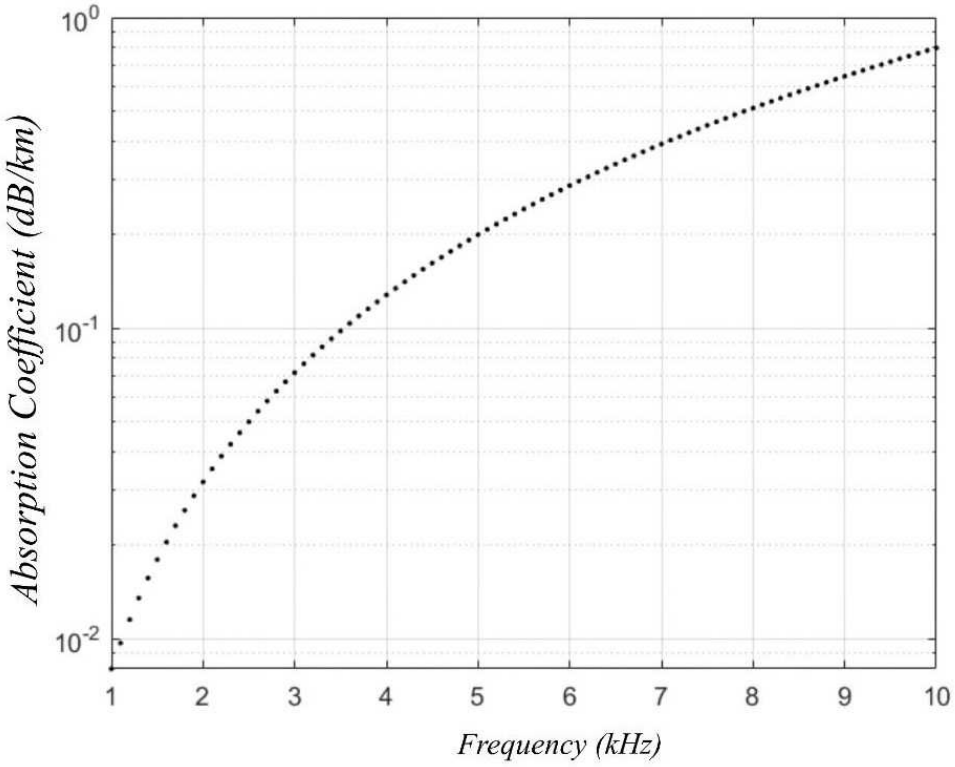

Figure 3.3: Absorption coefficient of acoustic signal in crude oil [112]

3.1.3 Transmission Loss

The acoustic signal travelling in the seawater gets distorted or weakened due to multipath or other loss mechanisms. Transmission loss is the standard measure to estimate the signal strength, which weakens as the range increases. It is generally described as an accumulated decrease in intensity of the signal when the signal propagates outwards from the source or propagates through some areas. It is measured in decibels (dB) and, is defined as,

$$TL = 10 \log \frac{I_o}{I}, \tag{3.7}$$

where I_o is the intensity at the reference point, and I is the intensity of the received signal.

In underwater environment, the transmission loss is considered as the sum of the spreading loss and attenuation loss in the ocean. The spreading loss is the regular weakening of

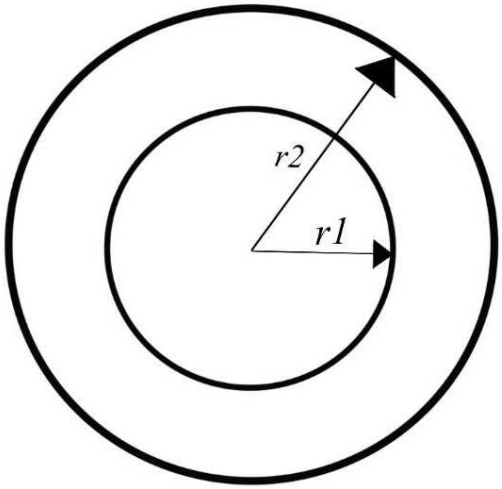

Figure 3.4: Illustration of spherical spreading [16]

the acoustic signal as it moves outward from the source. The spreading loss is classified into two types in the underwater environment: spherical spreading and cylindrical spreading.

The power generated by the signal from the point source in an unbounded homogenous medium radiates equally in all directions, which is distributed over a surface of the sphere, as shown in Figure 3.4. Since, the power is radiated equally in all directions in the spherical medium, it is distributed equally over the surface. Therefore, the power can be expressed as,

$$P = 4\pi r_1^2 I_1 = 4\pi r_2^2 I_2, \tag{3.8}$$

where I_1 is the reference intensity, I_2 is the intensity of the sound signal, r_1 is the reference radius, r_2 is the radius of the sphere. When the sound propagates in the medium, which has plane-parallel upper and lower bound, it will not spread spherically; instead, the sound is distributed over the surface of the cylinder having the radius r equal to the transmission range and the height H corresponding to the distance between parallel planes, as shown in

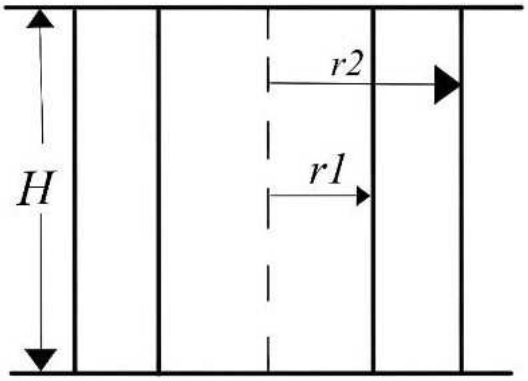

Figure 3.5: Illustration of cylindrical spreading [16]

Figure 3.5. The power crossing these cylindrical spheres can be expressed as,

$$P = 2\pi r_1 H I_1 = 2\pi r_2 H I_2, \tag{3.9}$$

where I_1 is the reference intensity, I_2 is the intensity of the sound signal, r_1 is the reference radius, r_2 is the radius of the cylinder, and H is the height of the cylinder.

The finite element analysis utilized in acoustic toolbox for estimating transmission loss is computationally intensive and time-consuming [113]. Marsh *et al.* proposed a semi-empirical formula for calculating the transmission loss of the acoustic signal. The transmission loss can be calculated from [16] [114],

$$10\log TL = \kappa 10\log l + l 10\log a\big(f\big), \tag{3.10}$$

where l is the distance between source and receiver, the first term is the spreading loss, and the second term is the absorption loss of the sound signal, calculated from Equation 3.5. κ is the spreading factor that depends on the type of geometrical spreading. $\kappa = 1$ for cylindrical spreading, $\kappa = 2$ for spherical spreading and $\kappa = 1.5$ is for transition region. We consider κ

= 1.5 as the spreading factor for our research because the spreading factor for the transition region is 1.5. [16] [115]. We utilize Equation 3.10 for calculating the transmission loss of the acoustic signal in seawater and oil in our work. The $a(f)$ in Equation 3.10 is calculated from Equation 3.5 for seawater and Equation 3.6 for oil.

This empirical formula is used to obtain a relatively accurate transmission loss of the acoustic signal in the underwater environment because it achieves the balance between accuracy and computational complexity.

3.1.4 Power and Intensity

The acoustic signal is transmitted with few watts of power from the source. The transmit power depends on the type of modem we use for specific applications. We discussed acoustic modems and their specifications in Section 2.2. The transmit power (p_t) in W can be converted into transmit power(P_t) in $dB\ re\ 1\mu Pa$ by using the Equation 3.11 [16] [116],

$$P_t = 10 \log_{10} \frac{p_t}{l_p}, \tag{3.11}$$

where l_p is the reference pressure. In our research, we assume the transmit power of the acoustic signal in W. To calculate the received power, we convert the transmit power (P_t) in W to $dB\ re\ 1\mu Pa$ using Equation 3.11.

The received power of the acoustic signal depends on transmit power (p_t), transmission loss, and attenuation loss. The received power (P_r) in dB at the reference distance l_r using frequency component f is given by [103],

$$P_r = P_t - 10\kappa \log_{10} \frac{l}{l_r} - a(f)(l - l_r), \tag{3.12}$$

where κ is the spreading factor. The received power needs to be converted into W, which can be obtained by,

$$p_r = l_{pwr} * 10^{P_r/10}, \tag{3.13}$$

where l_{pwr} is the reference power. To estimate the power carried by the acoustic signals per unit area in a direction perpendicular to that area, we should calculate the intensity. We calculate the intensity (I) of the acoustic signal using the expression [117],

$$I = \frac{p_r}{4\pi l^2}, \tag{3.14}$$

where l is the distance between the source node and receiving node.

3.1.5 Time of Arrival (ToA)

Time of Arrival (ToA) is one of the important factors for target detection and localization in the underwater environment. ToA is the absolute arrival time of the signal at the base station. We calculate the estimated ToA based on the distance between source and receiver, and the speed of the sound in the seawater. The estimated time of arrival of the received signal can be calculated from [16] [117],

$$t = l/c, \tag{3.15}$$

where t is the estimated time of arrival, l is the distance between source and the receiver, and c is the speed of the sound in seawater. We utilize the estimated ToA of the signal to effectively localize the position of the oil leak in the underwater environment.

3.1.6 Angle of Arrival (AoA)

The angle of arrival (AoA) is the direction from which the acoustic signal is received at the receiver. The bearing angle can be estimated based on phase difference or time delay of the received signals between array elements. We consider the two-element bearing estimation system to calculate AoA of the received signal [118]. The two-element array is shown in Figure 3.6. By assuming the plane sound wave signal, the AoA can be obtained from

$$c_{water}\big(t_A - t_B\big) = l_d . \cos\phi, \tag{3.16}$$

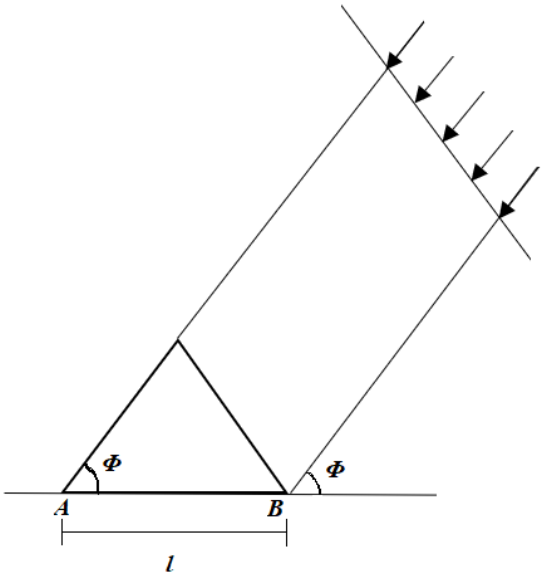

Figure 3.6: Incident sound waves and two-element receiving antenna array [118]

where l_d is the distance between two antennas, t_A and t_B are the propagation time from the source node to the antenna elements A and B, and ϕ is the angle of arrival of the receiving signal.

3.2 Boundary Behavior of Sound

When a sound wave travels through a medium, it will reach the end of the medium and encounters another medium through which it could travel. The interface of two mediums is known as boundary and the behavior of the sound wave at that boundary is described as boundary behavior. When the wave travels from one medium to another medium, a portion of the wave gets reflected whereas most of the wave gets transmitted. A wave travelling in a rarer medium to a denser medium undergoes a phase change of 180^o when that wave gets reflected whereas there will be no phase change if a wave travels from denser medium to rarer medium. There are four possible behaviors that a wave could exhibit

at a boundary: reflection, diffraction, transmission, and refraction. In this section, we describe the transmission, reflection, and refraction properties of sound in the underwater environment.

3.2.1 Transmission

The acoustic signal travelling in a medium is prone to reflection, refraction, scattering, diffraction, interference, and absorption. The transmission of sound is defined as the transfer

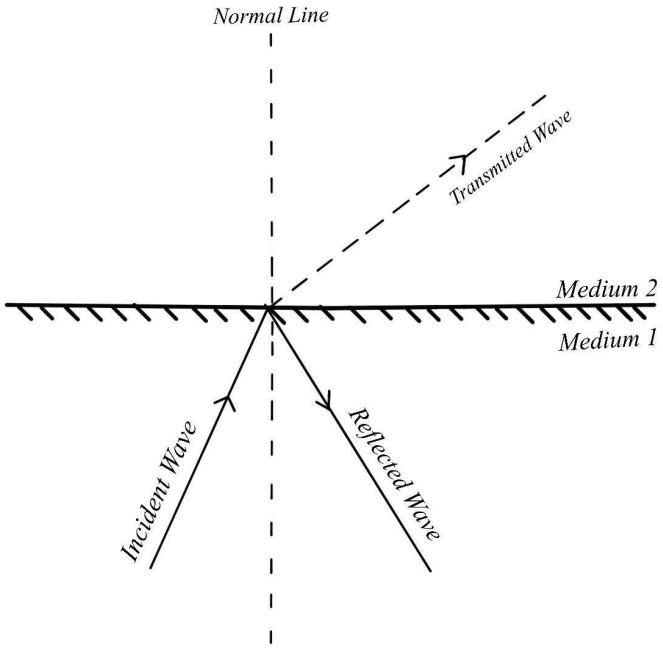

Figure 3.7: Illustration of transmission of sound in two mediums [112]

of acoustic energy through the medium in which it is travelling. Figure 3.7 illustrates the

transmission of sound through two different mediums. The transmission of the sound depends on the acoustic impedance of the medium. The acoustic impedance is given by,

$$z = \rho * c, \tag{3.17}$$

where, ρ is the density of the medium, c is the speed of sound in the medium.

3.2.2 Reflection

When the sound wave travels from one medium to another medium, it gets reflected. The reflected wave depends on the incident wave, the angle of incidence, the acoustic impedance of the travelling medium, and the reflecting surface. In our research, we consider perfect reflection of the acoustic signals. We utilize Snell's law of reflection, where the angle of incidence is equal to the angle of reflection. The Snell's law is given by [117],

$$\frac{\sin\theta_i}{c_1} = \frac{\sin\theta_t}{c_2} = \frac{\sin\theta_r}{c_1}, \tag{3.18}$$

where c_1 is the speed of sound in medium 1, c_2 is the speed of sound in medium 2, θ_i is the angle of incidence, θ_t is the angle of transmission, θ_r is the angle of reflection.

The reflection coefficient for the sound wave traveling from medium 1 to medium 2 is given by [119][120],

- Velocity reflection coefficient: The velocity reflection coefficient of the acoustic signal is obtained from the following equation,

$$V_R = \frac{z_1 - z_2}{z_1 + z_2} \tag{3.19}$$

- Pressure reflection coefficient: The pressure reflection coefficient of the acoustic signal is obtained from the following equation,

$$P_R = \frac{z_2 - z_1}{z_2 + z_1} = -V_R \tag{3.20}$$

- Energy reflection coefficient: The energy reflection coefficient of the acoustic signal is obtained from the following equation,

$$E_R = \left[\frac{z_1 - z_2}{z_1 + z_2}\right]^2 \tag{3.21}$$

In the above equations,

z_1 - acoustic impedance of sound in medium 1

z_2 - acoustic impedance of sound in medium 2.

Using Equations 3.19, 3.20, and 3.21, we can determine the reflection coefficient of the wave based on the fixed parameters of the incident wave. In the next section, we discuss the refraction coefficient of the transmitted wave.

3.2.3 Refraction

The acoustic signal is refracted to form transmitted waves when it reaches the boundary of another medium. When the angle of incidence is greater than the critical angle, energy contained in the acoustic waves are reflected. The acoustic wave is transmitted when the angle of incidence is less than the critical angle. The critical angle is defined by [112],

$$\sin\theta_c = \frac{c_1}{c_2} \tag{3.22}$$

where, c_1 is the speed of sound in medium 1, and c_2 is the speed of sound in medium 2. As discussed in Section 3.2.2, the refraction of sound is calculated based on Snell's law. There are three different cases that describe the refraction of the sound wave.

1. Case 1: If $c_1 < c_2$, the angle of incidence is greater than the refraction angle. The transmitted wave bends towards the normal to the boundary of all angles of incidence.

2. Case 2: If $c_1 < c_2$ and angle of incidence are smaller than the critical angle, the angle of incidence is less than the angle of refraction. The refracted wave bends away from

the normal for all angles of incidence.

3. Case 3: If $c_1 < c_2$ and angle of incidence are greater than the critical angle, the incident wave is totally reflected with no refraction. When the sound wave travels from one medium to another medium, it gets reflected.

Transmission coefficient for the sound wave travelling from medium 1 to medium 2 is given by [119][120]:

- Velocity transmission coefficient: The velocity transmission coefficient of the refracted wave is obtained from the following equation,

$$V_T = \frac{2z_1}{z_1 + z_2} \tag{3.23}$$

- Pressure transmission coefficient: The pressure transmission coefficient of the refracted wave is obtained from the following equation,

$$P_T = \frac{2z_2}{z_1 + z_2} \tag{3.24}$$

- Energy transmission coefficient: The energy transmission coefficient of the refracted wave is obtained from the following equation,

$$E_T = \frac{4z_1 z_2}{\left(z_1 + z_2\right)^2} \tag{3.25}$$

where,

z_1 - acoustic impedance of sound in medium 1

z_2 - acoustic impedance of sound in medium 2.

The refraction coefficient of the transmitted wave is determined using Equations 3.23, 3.24, and 3.25. Equations 3.19 and 3.20 represents the expression for the velocity and pressure reflection coefficient of the acoustic signal. From the equations, we can see that the

acoustic impedance z_1 and z_2 have different signs. The change in the sign is because the velocity and the pressure is reversed upon reflection and corresponds to the phase change by 180^o. For the transmitted wave, the velocity and the pressure remain in the same phase as the pressure and the velocity of the incident wave. The energy of the acoustic signal is proportional to the square of the amplitude of the acoustic signal.

For most of the applications in the underwater monitoring system, velocity and pressure are required for determining the solution. In our research, we consider the power and intensity of the acoustic signal for localizing the oil leak. Since, our main focus is on the estimated arrival time and power of the received signal, we utilize energy reflection and transmission coefficients.

3.3 Topology of UWSNs

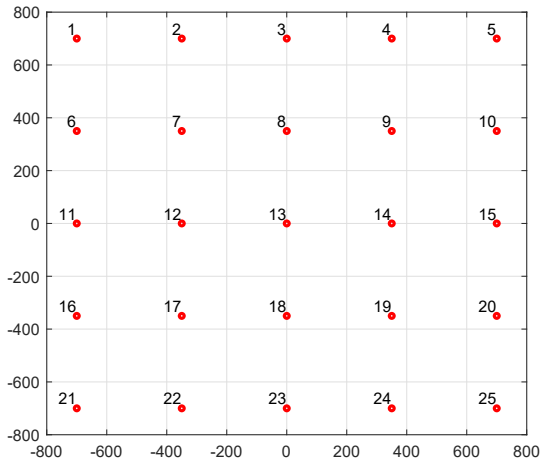

Figure 3.8: Illustration of UWSN with square grid topology

The network's topology is an important factor in determining energy consumption, reliability, and network capacity. The deployment strategy differs for wireless sensor networks

and the underwater wireless sensor networks. There are two types of architectures used in UWSN: 2D UWSNs, and 3D UWSNs. The two-dimensional architecture is used for underwater surface monitoring and underwater bottom monitoring. The three-dimensional architecture is used for underwater column monitoring.

There are three types of deployment processes in UWSNs: static deployment, self-adjustment deployment, and movement assisted deployment [121]. In static deployment, by considering the deployment cost and the complexity of the algorithm, the position of sensor nodes remains static after the deployment. Static deployment is classified into two types: random and regular deployment. When the deterministic deployment is not possible or knowledge of the area to be monitored is unknown, random deployment of nodes is utilized. The deterministic/regular deployment process is preferred for deploying sensor nodes in the ocean to perform collaborative monitoring tasks. In regular deployment, the sensor nodes are placed at the vertices of polygons or polyhedrons such as square, triangle, etc. In self-adjustment deployment, the sensor nodes can adjust their position after initial deployment in the underwater environment. Movement-assisted deployment involves underwater vehicles such as AUVs, ROVs, and other mobile sensor nodes. The underwater vehicles or the mobile nodes roam around the monitoring area, and cooperate with other sensor nodes to accomplish the tasks. The static deployment algorithm is usually centralized because the sensor nodes are deployed uniformly. These algorithms aim at maximizing the network coverage by minimizing the number of sensor nodes deployed. The energy consumption and computational complexity are low in static deployment algorithms compared to self-adjustment and movement assisted algorithms.

In our research, we consider a static two-dimensional architecture in UWSN for ocean monitoring. The static sensor nodes consist of a sensing device, a microcontroller, and an acoustic transceiver. The energy efficiency of square grid topology is better than triangular-

grid topology [122]. We consider untethered square grid topology network and untethered concentric hexagonal topology network for the long term leak detection and localization application. For square grid topology, a total of N_s x N_s sensor nodes (assuming N_s being the number of sensor nodes) is considered, as shown in Figure 3.8. Their geometric position forms a square lattice. For concentric hexagonal topology, a total of $6 \times N_h$ sensor nodes (as-

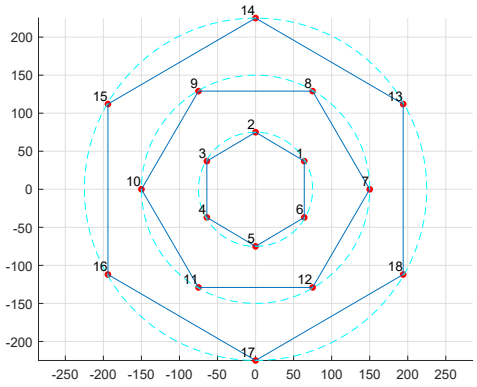

Figure 3.9: Illustration of UWSN with concentric hexagonal topology

suming N_h being the number of hexagons) is considered. Each node in concentric hexagonal topology is separated by an angle of 60^o, as shown in Figure 3.9. Their geometric positions form a hexagon. All the sensor nodes in these topologies are placed on the seafloor, which is assumed to be in the two-dimensional environment.

We assume that all the sensor nodes are equipped with sufficient battery energy. The sensor nodes utilize wireless acoustic sensing for obtaining the information from the other sensors. Similar to the assumption made in [1], we assume that each sensor node is equipped with an omnidirectional transceiver and the transmission range is r. The distance between two adjacent nodes is d_c. The neighbour node receives the sound signal from the source node if these two nodes are within the transmission range, r. The position information of all the sensor nodes is assumed to be known *a priori*. In Chapters 4,5 and 6, we further discuss

these topologies in detail.

3.4 Summary

In this chapter, we reviewed the propagation properties of the acoustic signal in seawater, such as sound speed profile, absorption loss, and spreading loss. We consider the value of spreading factor as $k = 1.5$ in our research. We studied the semi-empirical formula for evaluating transmission loss of acoustic signal and achieving the balance between accuracy and computational complexity. We then presented the expressions for some of the important factors required for target detection and localization underwater, such as received power, intensity, estimated time of arrival, and angle of arrival of the received signal. Finally, we explained untethered network topologies we used in our research.

Chapter 4

Two-Dimensional Analysis Leak Detection

Compared to terrestrial WSNs, target detection in UWSNs is challenging because acoustic sensor nodes are equipped with non-rechargeable and unchangeable batteries to provide power for long-term communications and data collection. Due to the high cost of underwater acoustic sensor nodes, and the non-trivial deployment cost, the number of sensor nodes in UWSNs is limited. The topologies of UWSNs are often predetermined and regular, such as linear, ring, star, and grid. Increasing concern about the pollution levels in the ocean and coastal regions has resulted in multiple strategies to monitor and reduce marine pollution. In recent years, the oil spill is a significant threat to the marine ecosystem. Therefore, to minimize the impact of the oil spill and to prevent the massive oil spill from happening, it is essential to develop effective, early and accurate leak detection mechanisms for UWSNs.

In this chapter, the problem of oil leak caused by pipeline breakage or other factors in UWSNs is addressed. We propose a range estimation method for the detection of oil leak in UWSNs. We perform a two-dimensional analysis of the proposed method. In this analysis, we consider 2D UWSNs with a square grid topology and concentric hexagonal topology. The

position information of the sensor nodes is assumed to be known *a priori*. All these sensor nodes utilize wireless acoustic links for gathering information from other sensor nodes. We consider oil leaks at different ocean depths, including at the seafloor, in the middle of the sea, and on the ocean surface with different sizes and shapes. We investigate the detection ratio of the proposed method by conducting theoretical analysis for different topology sizes. We study the performance evaluation of the proposed scheme for different sizes of leak under different topology densities based on transmission range r.

We organize this chapter as follows. We present the proposed detection method in Section 4.1. The detection ratio of two-dimensional analysis of the proposed method was analyzed by conducting a theoretical analysis in Section 4.2. In Section 4.3, we present the performance evaluation of the proposed method, and we conclude the chapter in Section 4.4.

4.1 Proposed Leak Detection Method

In this section, we present the proposed leak detection method using the range estimation approach. We first present the underwater channel model and the topology of UWSNs used in our work. Preliminaries of the proposed method are then discussed. The proposed range estimation method minimizes the impact of the oil spill and guarantees oil spill detection at the early stage. As discussed in Chapter 3, we utilize the semi-empirical formula (Equation 3.10) to study the underwater acoustic channel and calculate the transmission loss of acoustic signal in the seawater and the oil. The value of *a(f)* can be calculated from Equation 3.5 for seawater and Equation 3.6 for oil.

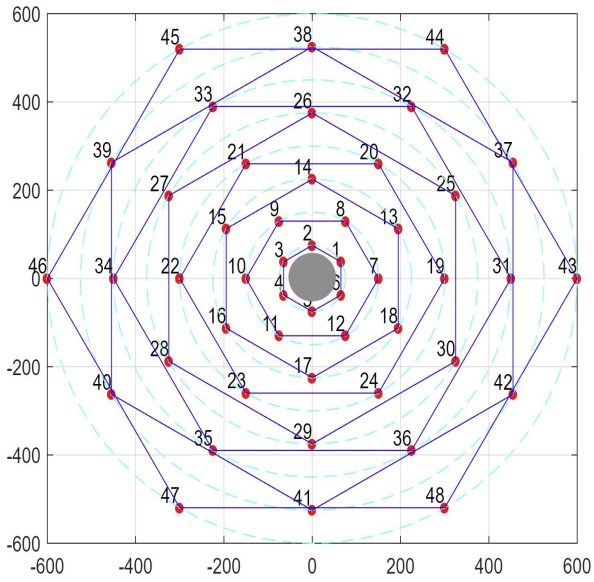

Figure 4.1: Illustration of concentric hexagonal topology with caisson

4.1.1 Topology in UWSN

Our research mainly focuses on the detection and localization of oil spills at the early stage. Based on the literature study, we consider two possibilities which cause oil leaks in the underwater environment. The first possibility is the oil rig platform because the possibility of an oil leak near the rig is high compared to all the other factors. And the second possibility is from the pipeline, which takes the oil from the rig to the tankers. For these two cases, we use two different topologies for calculating the detection ratio. To focus on the area near the caisson, we utilize concentric hexagonal topology. We assume the sensor nodes are placed around the caisson in hexagonal fashion to get better efficiency, as shown in Figure 4.1. Many pipelines in the underwater environment carry oil to the tankers. To detect the leak from the pipeline breakage, we utilize square grid topology and concentric hexagonal topology, as shown in Figure 4.2 and 4.3.

Two sensor nodes can communicate with each other if these two nodes are within the transmission range, r. We consider square grid topology with 49 nodes and concentric

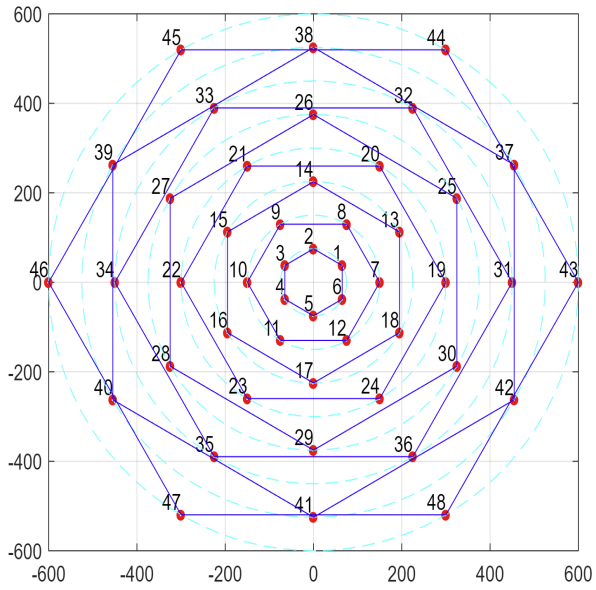

Figure 4.2: Illustration of concentric hexagonal topology without caisson

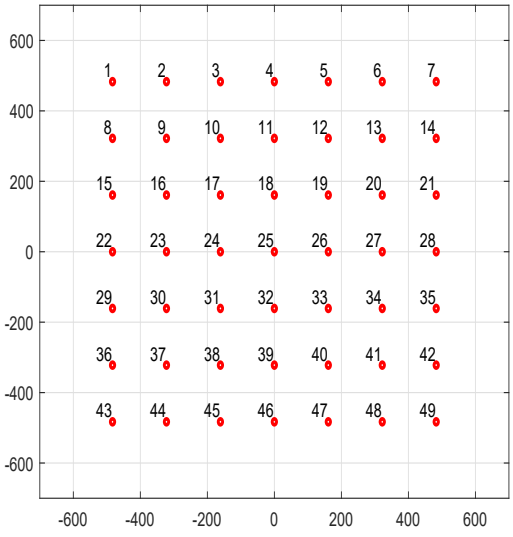

Figure 4.3: Illustration of square grid topology

hexagonal topology with 48 nodes for analyzing the results.

4.1.2 Objective and Assumptions

Our objective is to design an underwater oil leak detection method that detects 90% of the leak at the early stage, as mentioned in Chapter 1. We assume that all the sensor nodes are equipped with sufficient battery energy. The sensor nodes utilize wireless acoustic sensing for obtaining the information from the signal transmitted by the source node. In our design, each sensor node acts as a transmitter and receiver. The operation of each sensor node alternates between transmitting mode and receiving mode. At a time, only one node can act as a transmitter, and all the other nodes within the transmission range r receive the signal. The receiver nodes that are affected by the presence of oil leak are termed as affected receiver nodes. Initially, the sensor node with $nodeID$ 1 is selected as a transmitter to transmit the signal. If the node 1 does not have any affected receiver nodes, the next node from the list (in this case node 2) becomes the source node. If the leak is detected, then the localization process is started, which is discussed in Chapter 6.

4.1.3 Range Estimation Method

In this section, we present a range estimation method for detecting oil leaks in the underwater environment. Receiver nodes affected by the presence of oil leak can be determined using this proposed technique, as shown in Figure 4.4.

In this technique, the range is projected from the source node to the maximum distance d_{max}. We assume the value of d_{max} to be 50 m greater than the transmission range r to cover the network area. Let us say, the oil leak is at the location (x4, y4). For theoretical analysis, we consider the size and location of the oil leak as known. Two perpendicular lines are drawn with respect to the source node. Line 1 is drawn with respect to the range between the source node and oil leak location with the length of the diameter of the oil leak. Line 2 is projected with respect to the oil location and the maximum distance from the source

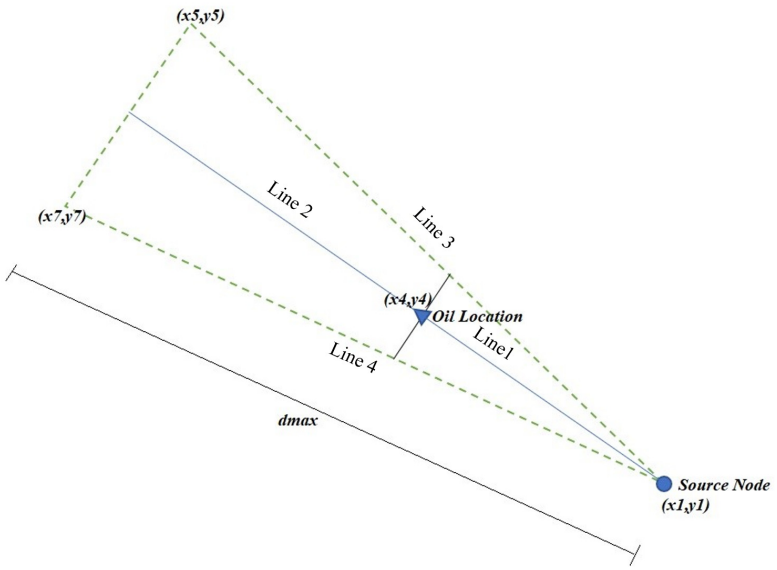

Figure 4.4: Proposed range estimation method

node. Line 3 and Line 4 are drawn and the endpoints of the second perpendicular line are calculated to form a triangle.

When the sensor node becomes the transmitter, the coordinates of the range estimation triangle is computed with respect to the source node. The coordinates of the receiver node, which lies inside the estimated triangle region, are most likely affected by the oil leak. The power, intensity, and ToA of the signal received by the sensor of the affected nodes are recorded and used to detect and localize leak.

4.2 Elucidation of Proposed Scheme

In the previous section, we presented the proposed range estimation method for the detection of an oil leak. In this section, we theoretically analyze the proposed scheme. As mentioned in previous chapters, oil leaks located at different ocean depths are considered, such as near the seafloor, in the middle of the sea, and on the ocean surface. As we discussed in Section 4.1.1, the oil leak is caused by two different factors: oil rig and pipeline breakage. As we

discussed several times, one of the main causes of a spill is when oil is transferred to a tanker. We assume the oil leak can be present anywhere inside the network. We perform two-dimensional analysis for calculating the results. We consider the oil leak at every 1 m interval within the selected network area for two different cases for analyzing the results.

Case 1: We consider the transmitter and receiver as single points.

Case 2: We consider the transmitter and receiver as a circle with a diameter of 10 cm.

We consider different sizes and shapes of oil leaks for better analyzing our proposed method by two-dimensional analysis. We show the results based on network size and size of the leak.

4.2.1 Detection of Oil Leak from the Oil Rig

An oil platform is a large structure built to explore, extract, and process the petroleum products that lie beneath the seabed. The description of the oil platform, its types, and its applications were discussed in Chapter 2. From the literature study, it is understood that oil leak often occurs in the vicinity of a platform. We consider the Hibernia oil rig platform located 315 km east-south west off St. John's, Newfoundland and Labrador, Canada, in 80 m of water for our research. Since the Hibernia platform is a gravity based structure (GBS), it has a concrete caisson with a diameter of 130 m placed on the seafloor. In our work, we use a sensor network with concentric hexagonal topology having the concrete caisson in the middle with a height of 80 m and a diameter of 130 m. The sensor nodes are placed around the caisson in the hexagonal fashion, as shown in Figure 4.1. Our main area of focus is near the caisson. We consider the oil leak to be inside the innermost hexagon. For detecting the leak near the caisson, we consider the triangle-shaped leak near the seafloor and rectangle-shaped leak near the ocean surface. We calculate results for two different cases, as mentioned above.

4.2.2 Detection of Oil Leak from the Pipeline Breakage

There are many pipelines deployed underwater for carrying oil from the rig to the tankers. The oil leak is most likely to happen from the pipeline breakage. We consider two different topologies for detecting the leak from the pipeline breakage. We analyze the proposed scheme based on these two topologies. The values listed in Table 4.1 are given for two different topologies with different network sizes and distance between adjacent nodes. We select the number of nodes and the distance between adjacent nodes to have a fair comparison between two topologies. The oil leak is assumed to be anywhere inside the network area.

For detecting the leak from the pipeline breakage, we consider the leak at three different levels: near the seafloor, in the middle of the sea, and on the ocean surface. The results are calculated based on two different types of transmitter and receiver with two different transmission ranges. We consider both the direct and reflected properties of the acoustic signal while evaluating the performance.

1. *Near the Seafloor:* We consider a triangle-shaped leak with height of 80 m and diameter of the leak as 3 m, 5 m, 10 m or 15 m. Different leak diameter for the triangle-shaped leak corresponds to 188.5×10^3 $litres$, 523.6×10^3 $litres$, 2094.4×10^3 $litres$, or 4712.39×10^3 $litres$ of leaked oil. The illustration of a triangle-shaped leak is shown in Figure 4.5.

2. *Middle of the Sea:* For detecting the oil leak in the middle of the sea, we consider a trapezoid of height 10 m located at the height of 35 m from the seafloor, as shown in Figure 4.6. The diameter of the lower base of the frustum is 1 m. We consider different diameter of the leak for the upper top as 3 m, 5 m, 10 m or 15 m. Different leak diameter for the frustum-shaped leak corresponds to 34.04×10^3 $litres$, 81.15×10^3 $litres$, 290.59×10^3 $litres$, or 630.93×10^3 $litres$ of leaked oil.

3. *Ocean Surface:* After the oil leak, the spilled oil reaches the ocean surface and spreads across the ocean because of the water current. We consider a rectangle-shaped leak for detecting the leak near the ocean surface, as shown in Figure 4.7.

Number of nodes in square grid	Number of nodes in concentric hexagon	Distance between adjacent nodes in square grid (m)	Maximal diameter of outer hexagon (m)	Area of square grid (m^2)/ Number of nodes	Area of concentric hexagon (m^2)/ Number of nodes
16	18	121	450	8235.56	8831.25
25	24	121	600	9370.24	11775
49	48	161	1200	19044	23550
16	18	242	900	32942.25	35325
25	24	242	1200	37480.96	47100
49	48	322	2400	76176	94200
16	18	282	1050	44732.25	48081.25
25	24	282	1400	50895.36	64108.33
49	48	376	2800	103868.08	128216.67

Table 4.1: Selection of network size

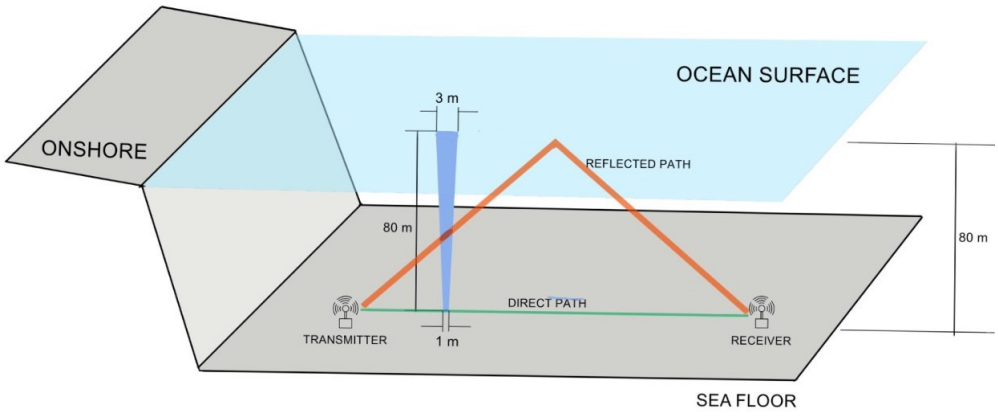

Figure 4.5: Illustration of a triangle-shaped leak

4.3 Performance Evaluation

The sensor nodes in UWSNs utilize wireless acoustic sensing for gathering information from the source nodes. The sensors in the nodes are omnidirectional. In this section, we study the performance evaluation of the proposed leak detection method using two-dimensional analysis. We evaluate the performance based on the detection ratio, network scalability, and power consumption.

4.3.1 Evaluation Parameters

In our work, the parameters we used correspond to Modem 6 Sub-Mini, a widely used underwater acoustic modem designed by Sonardyne. In choosing the evaluation parameters and conditions, we prioritize the applicability of our results to practical UWSN applications. This modem allows the 1 W of transmit power level and 0.2 nW of receiver sensitivity. The

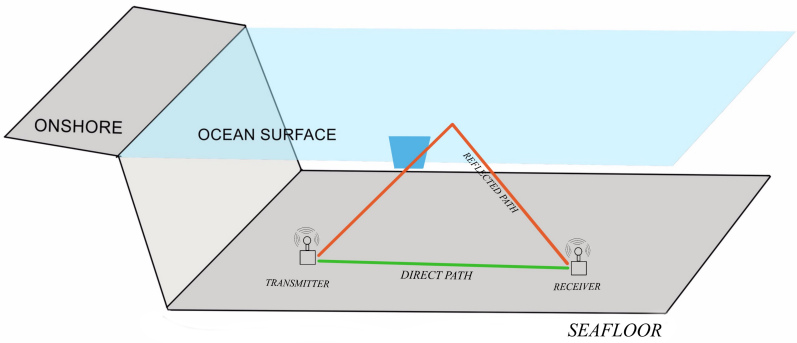

Figure 4.6: Illustration of a trapezoid-shaped leak

technical specification of several acoustic modems with a transmit power of 20 W can achieve the transmission range of 1000 m. Some researchers have employed different transmission powers that correspond to different transmission ranges. We use the transmit power of 1 W, which corresponds to the transmit sound source level of 181 $dB\ re\ 1\ \mu Pa^2$, calculated from Equation 3.11.

For evaluation, we utilize Equation 3.5 and Equation 3.6 for calculating the absorption coefficient of sound in seawater and the oil. For detecting the oil leak, the estimated power and intensity of the acoustic signal from one node to all possible receiver nodes in the topology network is calculated. The estimated power of the received signal can be calculated from the Equation 3.12. We utilize Equation 3.14 for calculating the intensity of the received signal. If the difference between the received power and estimated power is not same, then there

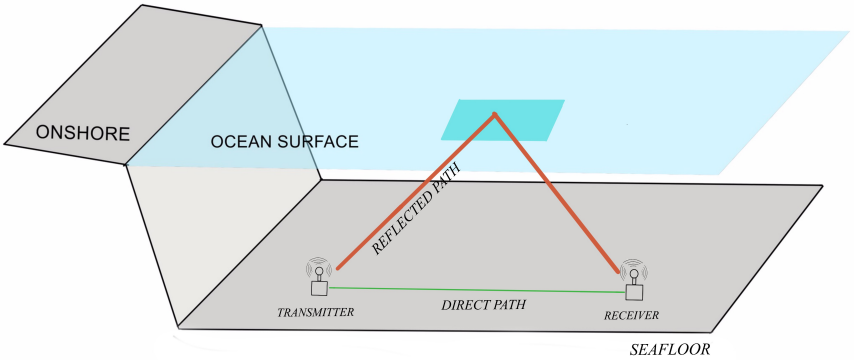

Figure 4.7: Illustration of a rectangle-shaped leak

is the presence of oil leak between that pair of sensor nodes. We summarize the evaluation parameters in Table 6.3.

4.3.2 Detection Ratio

In this subsection, we investigate the detection ratio of sensor nodes for different leak sizes, shapes, and network sizes.

4.3.2.1 Near the oil rig

This section investigates the detection ratio and scalability of the proposed scheme near the oil rig. As mentioned earlier, we consider concentric hexagonal topology with 48 nodes for detecting the leak near the caisson. Figure 4.8 and Figure 4.9 shows the detection percentage

Table 4.2: Parameters and values

Parameters	Value
transmission range r	1000 m or 2000 m
center frequency of the acoustic modem f	10 kHz
speed of sound in water c_{water}	1500 m/s
speed of sound in crude oil c_{oil}	1347.3 m/s
speed of sound in air c_{air}	343 m/s
density of water ρ_{water}	1000 kg/m^3
density of crude oil ρ_{oil}	809 kg/m^3
density of air ρ_{air}	1.27 kg/m^3
transmitting power p_t	1 W
depth of the water	80 m
reference distance l_r	1 m
threshold value for power	0.2×10^{-09} W

of the proposed leak detection method for two different shapes of the leak: triangle-shaped leak near the seafloor, and a rectangle-shaped leak near the ocean surface. We show the results corresponding to concentric hexagonal topology with the maximal diameter of the hexagon as 350 m, 700 m, 1050 m, 1400 m, 1750 m, 2100 m, 2450 m, and 2800 m and concentric hexagonal topology with the maximal diameter of the hexagon as 150 m, 300 m, 450 m, 600 m, 750 m, 900 m, and 1050 m. The reason for showing the results for different network areas is to understand the results of the proposed scheme better. We set the diameter of the oil leak as 3 m, 5 m, 10 m, or 15 m. From Figure 4.8 and Figure 4.9, we observe that the detection percentage increases with the size of the leak. As mentioned in

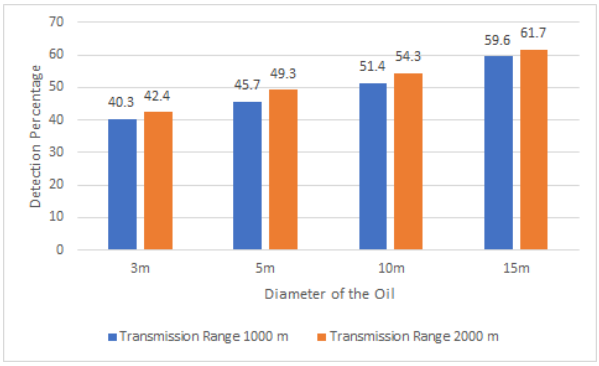

(a) Case 1 with transmission range 1000 m and 2000 m

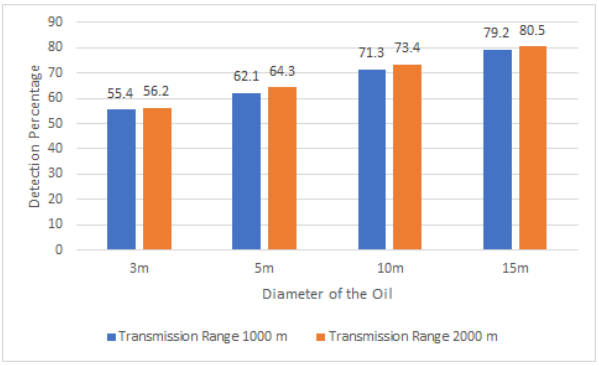

(b) Case 2 with transmission range 1000 m and 2000 m

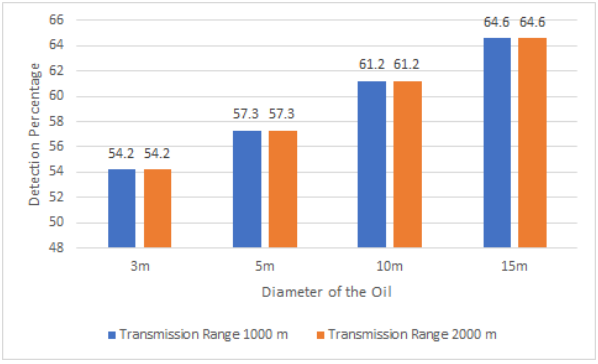

(c) Case 1 with transmission range 1000 m and 2000 m

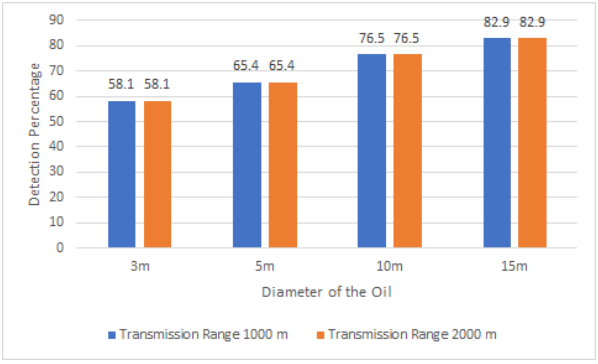

(d) Case 2 with transmission range 1000 m and 2000 m

Figure 4.8: Detection ratio based on two-dimensional analysis for triangle-shaped leak near the oil rig

Section 4.2, the two-dimensional analysis shows the results for two cases with transmission ranges of 1000 m and 2000 m. As mentioned earlier, we consider the depth of the water to be 80 m.

Figures 4.8a, 4.8b, 4.9a, and 4.9b shows the results corresponding to concentric hexagonal topology having the maximal diameter of the outer hexagon as 2800 m, and Figures 4.8c, 4.8d, 4.9c, and 4.9d shows the results corresponding to the concentric

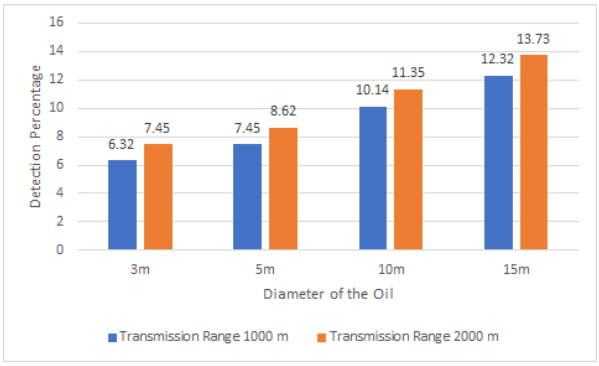

(a) Case 1 with transmission range 1000 m and 2000 m

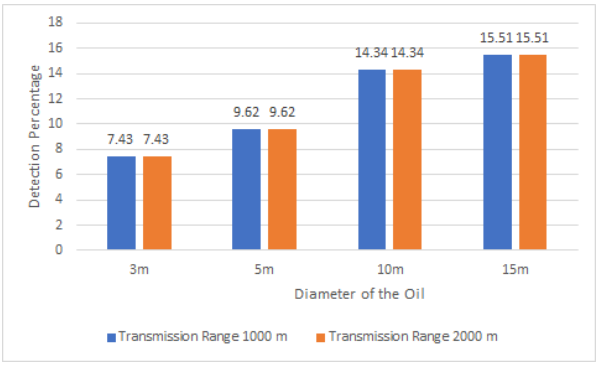

(b) Case 2 with transmission range 1000 m and 2000 m

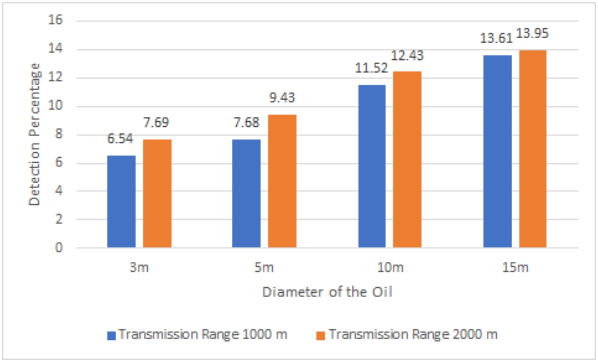

(c) Case 1 with transmission range 1000 m and 2000 m

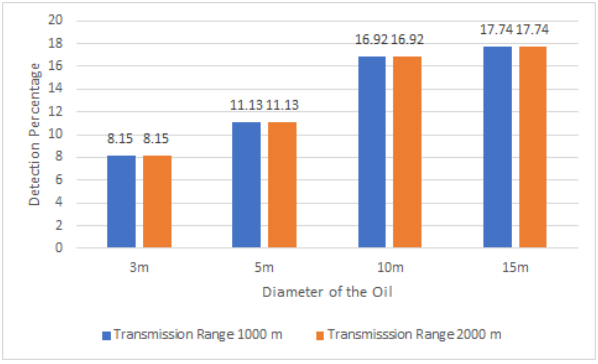

(d) Case 2 with transmission range 1000 m and 2000 m

Figure 4.9: Detection ratio based on two-dimensional analysis for rectangle-shaped leak on the surface near the oil rig

hexagonal topology having the maximal diameter of the outer hexagon as 1200 m. We calculate the results for two concentric hexagonal topologies to eliminate the blind spot areas. The blind spot areas refer to the oil leak location that is not detectable by the sensor nodes because of the topology structure. We calculate the results of the concentric hexagonal topology having the maximal diameter 350 m, 700 m, 1050 m, 1400 m, 1750 m, 2100 m, 2450 m, and 2800 m. Since, for detecting the leaks near the caisson, we concentrate on the

area near the caisson. In this case, the leak is assumed to be inside the hexagon of maximal diameter 350 m. Based on the dimensions we assumed, we experienced many blind spot locations because of the assumed maximal diameter of the hexagon. To avoid the blind spot and to get a better detection ratio compared to the topology dimensions we assumed before, we calculate the results for the concentric hexagonal topology having the maximal diameter 150 m, 300 m, 450 m, 600 m, 750 m, 900 m, 1050 m, and 1200 m. We consider the oil leak diameter as 3 m, 5 m, 10 m, or 15 m.

Each subfigure in Figure 4.8 and Figure 4.9 has two bars for each of the four diameters of the leak, as mentioned earlier. The first bar shows the result for the transmission range 1000 m, and the second bar shows the results for the transmission range 2000 m. We can see the rectangle-shaped leak gives a better detection percentage than a triangle-shaped leak. In addition to this, the transmitter and receiver as a circle with a diameter of 10 cm gives better detection percentage than the transmitter and receiver as single points. The detection percentage for the leak near the ocean surface is reduced by more than 80% because we consider the perfect reflection of the acoustic signal at the ocean surface.

4.3.2.2 From the Pipeline Breakage

In this section, we analyze the detection ratio of the proposed scheme for detecting the leak from the pipeline breakage. As shown earlier, we consider square grid topology with 49 nodes and concentric hexagonal topology with 48 nodes for detecting the leak from the pipeline breakage. Figure 4.10, Figure 4.11, and Figure 4.12 shows the detection percentage of the proposed leak detection method for the leaks at three different levels of the ocean: near the seafloor, middle of the sea and the ocean surface. The distance between two adjacent nodes in the square grid topology is 161 m, and the maximal diameter of the outer hexagon in the concentric grid topology is 1200 m, as shown in Table 4.1. We consider the depth of the

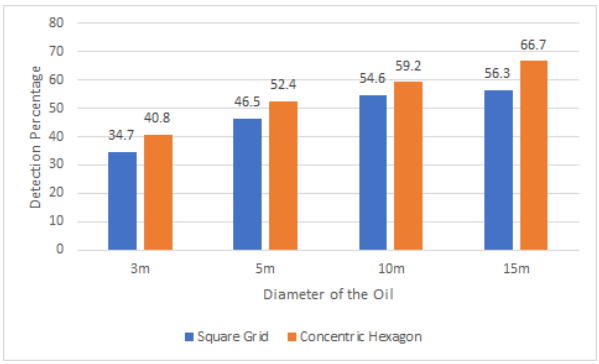

(a) Case 1 with transmission range 1000 m

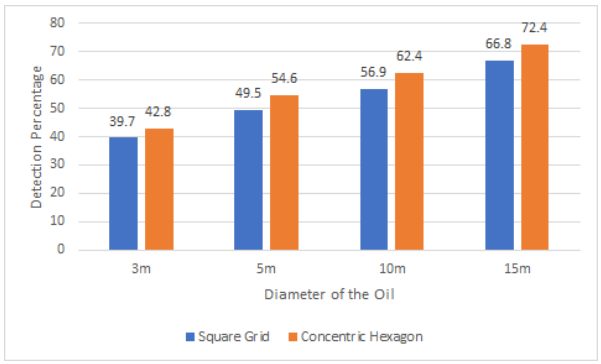

(b) Case 1 with transmission range 2000 m

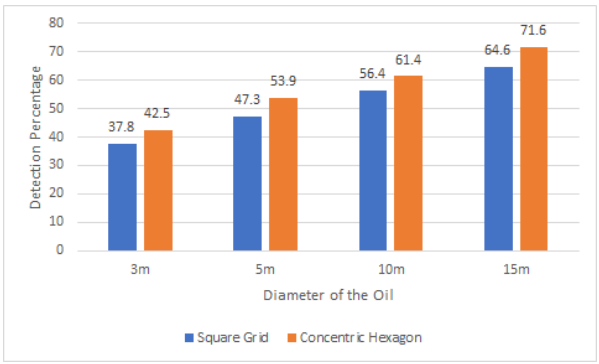

(c) Case 2 with transmission range 1000 m

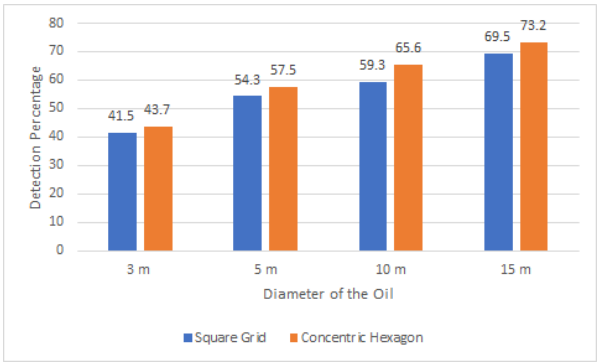

(d) Case 2 with transmission range 2000 m

Figure 4.10: Detection ratio based on two-dimensional analysis for triangle-shaped leak from the pipeline breakage

water column as 80 m.

1. *Near the ocean floor:* We consider a triangle-shaped leak near the seafloor because when the oil leaks from the pipeline, it slowly travels to the surface in the form of a cone and starts spreading as a thin layer on the surface because of water currents. We study the results for different diameters of the oil leak, such as 3 m, 5 m, 10 m, or 15 m, using square grid topology and concentric hexagonal topology.

   Figure 4.10 shows the results of the detection ratio of a triangle-shaped leak from the pipeline breakage for two cases mentioned in Section 4.2. The two bars in the

Figure 4.10 represent the results of square grid topology and concentric hexagonal topology. From Figure 4.10, it is evident that the detection percentage increases with the size of the leak. Compared to all the four subfigures, Figure 4.10d shows the higher detection percentage because the transmission range is 2000 m. It should also be noted that the proposed method using concentric hexagonal topology gives a better detection percentage than square grid topology.

2. *Middle of the sea:* For detecting the oil leak in the middle of the ocean, we consider

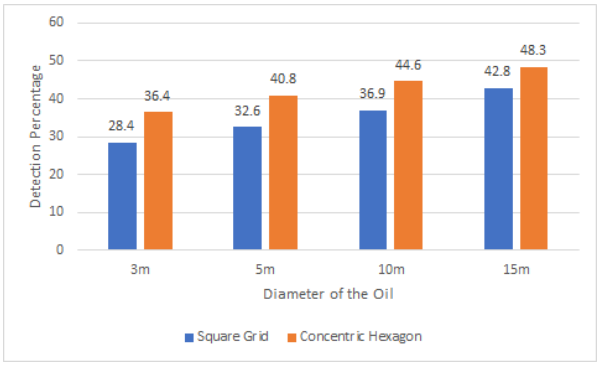

(a) Case 1 with transmission range 1000 m

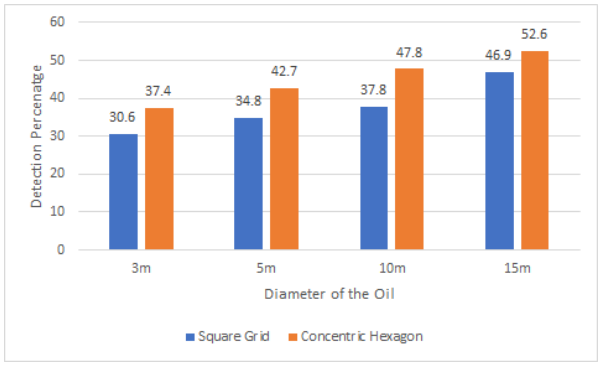

(b) Case 1 with transmission range 2000 m

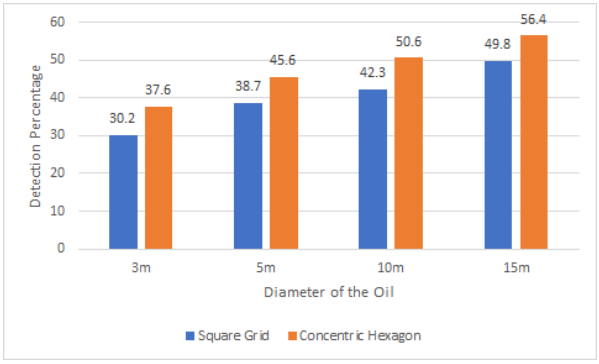

(c) Case 2 with transmission range 1000 m

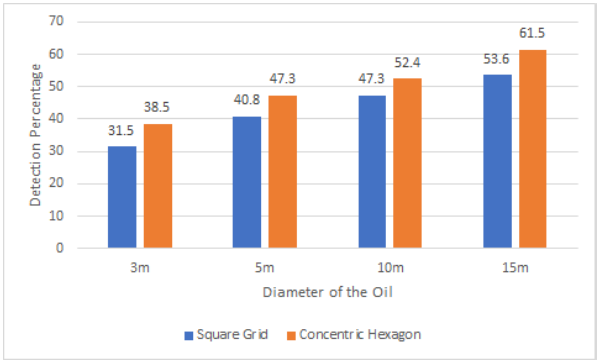

(d) Case 2 with transmission range 2000 m

Figure 4.11: Detection ratio based on two-dimensional analysis for trapezoid-shaped leak in the middle of the ocean

a trapezoid-shaped leak in the middle of the sea about 30 m from the ocean floor. Once the oil leaks from the pipeline, it starts travelling to the surface. Sometimes, the leaked oil moves as slicks in the ocean. To detect that kind of oil slicks, we assume a trapezoid-shaped leak. Similar to the triangle-shaped leak, we consider different sizes of the trapezoid to understand the results better.

The detection ratio of the trapezoid-shaped leak in the middle of the sea due to pipeline breakage is shown in Figure 4.11. Figure 4.11d gives a better detection percentage compared to all the other subfigures. For the leak with a diameter of 15 m, the detection percentage of the triangle-shaped leak is 80% with transmission range 2000 m for Case 2, whereas the detection percentage of the trapezoid-shaped leak is 60% with transmission range 2000 m for Case 2. This is because for a triangle-shaped leak, the height of the triangle is equal to the depth of the water column, which helps the sensor nodes to detect the leak easily compared to the trapezoid, which is just the section of the triangle of height 10 m.

3. *Ocean surface:* At worst case, if the proposed method fails to detect the leak at the early stage, the spilled oil travels to the ocean and forms a thin layer of slick at the ocean surface. We consider a rectangle-shaped leak at the ocean surface with varying sizes to detect the leak.

   Figure 4.12 illustrates the detection ratio of the rectangle-shaped leak for two different cases mentioned in Section 4.2. Compared to the detection percentage of a leak near the ocean floor, and in the middle of the sea, the detection percentage of a leak near the ocean surface is reduced by almost 70%. The detection percentage of a leak near the ocean surface with the diameter 15 m and transmission range 2000 m is 21%, whereas it is 79% and 61% for the leak near the ocean floor, and in the middle of the ocean for

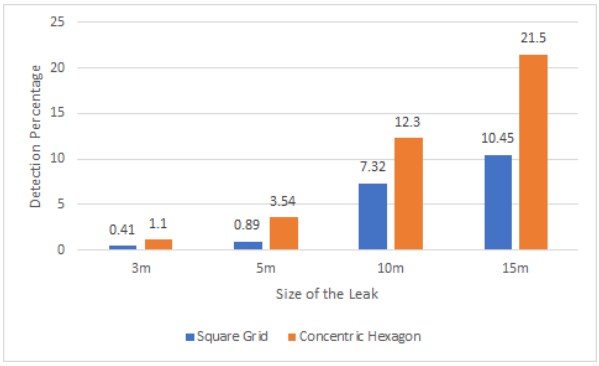

(a) Case 1 with transmission range 1000 m

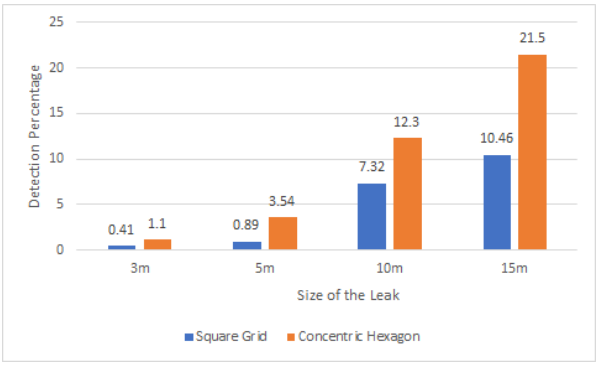

(b) Case 1 with transmission range 2000 m

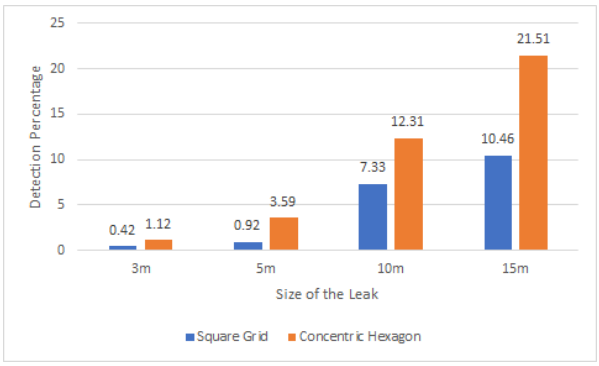

(c) Case 2 with transmission range 1000 m

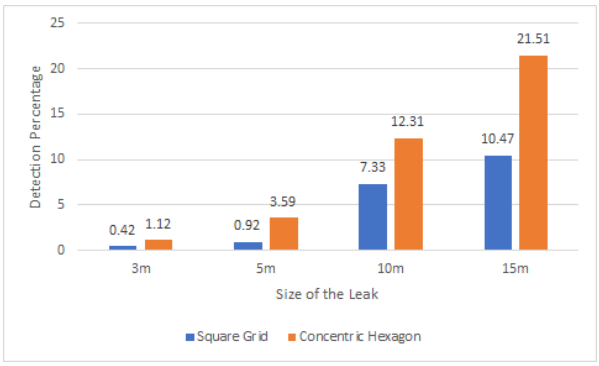

(d) Case 2 with transmission range 2000 m

Figure 4.12: Detection ratio based on two-dimensional analysis for rectangle-shaped leak near the ocean surface

the same condition. The reason for the low detection percentage is because we assume a perfect reflection for surface leaks. We select the perfect reflection of the acoustic signal at the ocean surface because of the ideal conditions studied in the literature study. We can even ignore the perfect reflection and detect the oil leak, but it will complicate the process because of the refraction. We plan to extend our research to detect the oil leak without perfect reflection in the future.

The above discussion shows that the detection percentage is directly proportional to the size of the leak. It should also be noted in the above analysis that concentric hexagonal topology

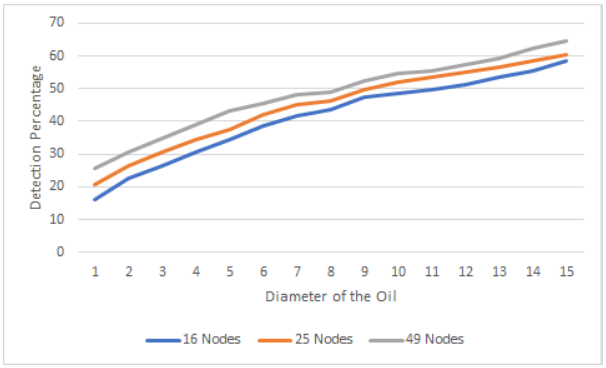

(a)

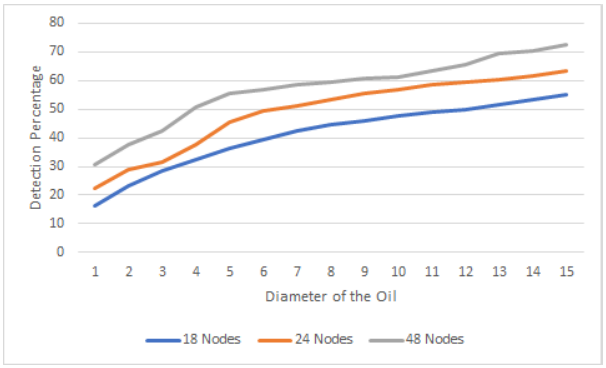

(b)

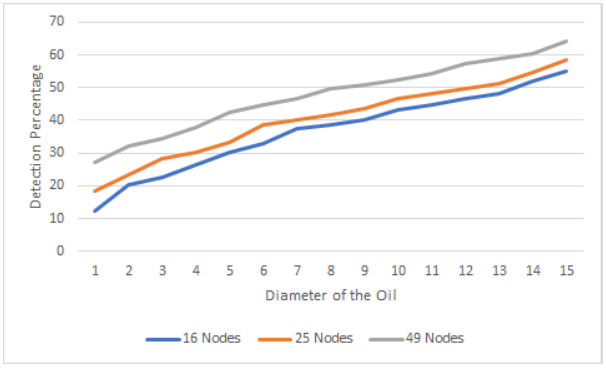

(c)

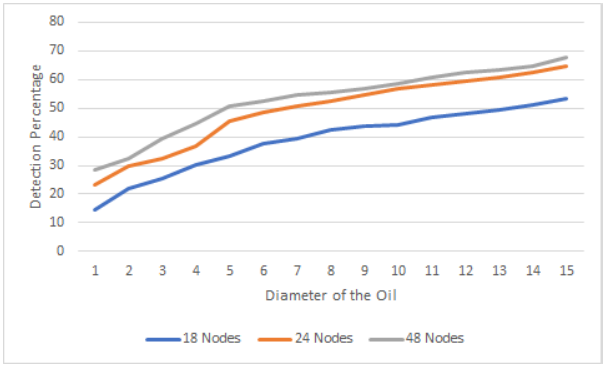

(d)

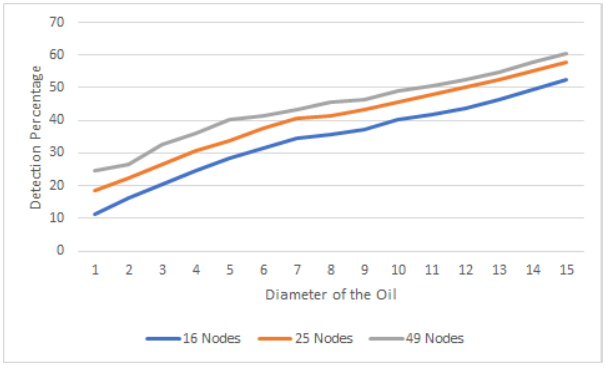

(e)

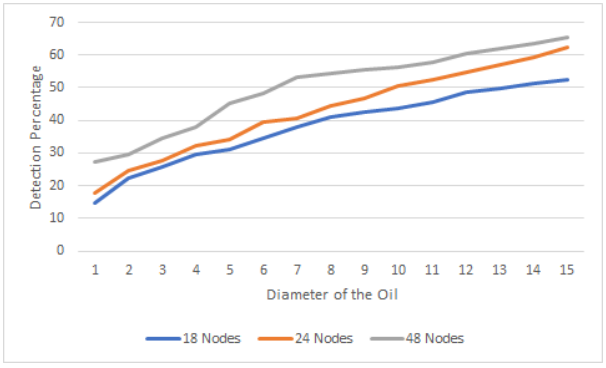

(f)

Figure 4.13: Network scalability based on two-dimensional analysis for triangle-shaped leak

gives better results than square grid topology. In every comparison, the square grid topology covered a smaller area than the concentric hexagonal topology, but the square grid topology had more sensor nodes. Although, the node density is greater for the square grid topology,

the performance is less compared to concentric hexagonal topology. The detection percentage also varies with the transmission range and size of the transmitter and receiver.

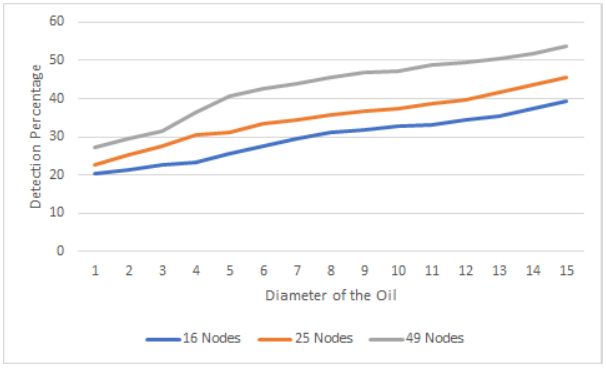

(a)

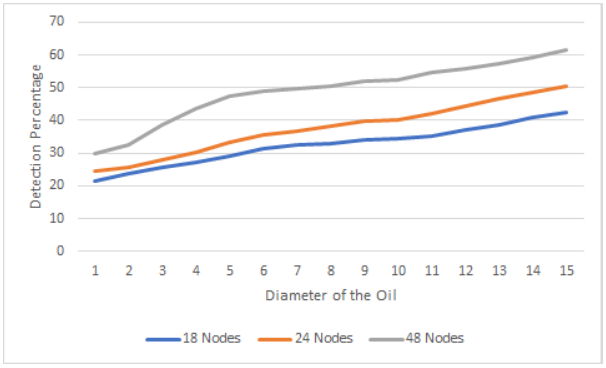

(b)

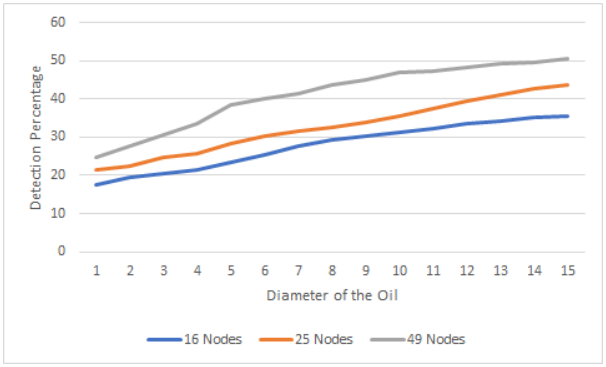

(c)

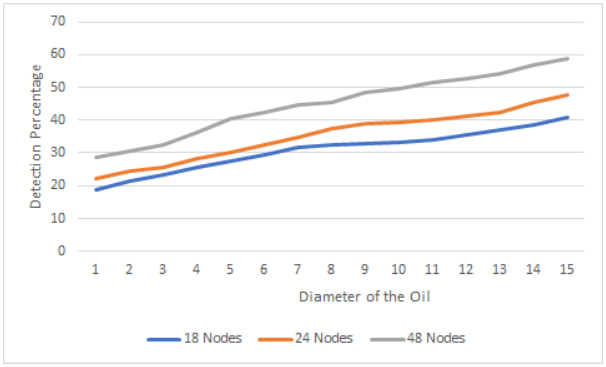

(d)

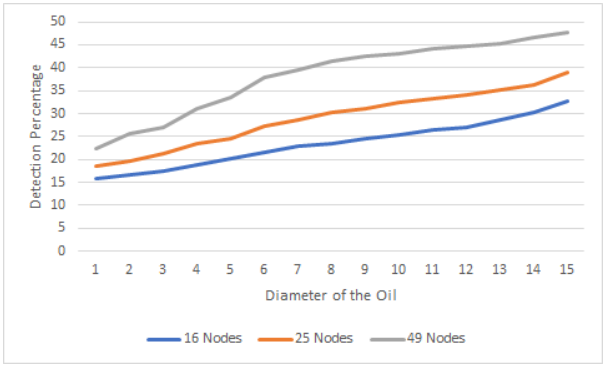

(e)

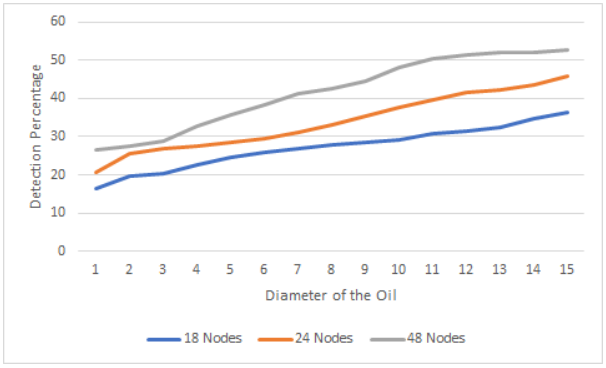

(f)

Figure 4.14: Network scalability based on two-dimensional analysis for trapezoid-shaped leak

4.3.3 Network Scalability

In this subsection, we investigate the detection ratio of sensor nodes for different network size, leak size, and distance between adjacent nodes. Figures 4.13, 4.14, 4.15 shows the detection ratio of sensor nodes under three different network sizes and three different distances between adjacent nodes. We consider the same network topologies, as we discussed in the previous section. We vary the diameter of the oil leak from 1 to 15 m. Figure 4.13 shows the plot for the detection percentage for the triangle-shaped leak near the ocean floor. Figure 4.14 shows the plot for the detection percentage for the trapezoid-shaped oil leak in the middle of the ocean. Figure 4.15 shows the plot for the detection percentage for the rectangle-shaped oil leak on the ocean surface. The three subfigures on the left side from the Figures 4.13, 4.14, and 4.15 shows the results for square grid topology, and the three subfigures on the right side show the results for concentric hexagonal topology.

For a given maximal diameter of the hexagon, the larger network leads to a higher detection ratio because more sensor nodes increase the possibility of detecting the leak. Increasing node density makes it unrealistic for implementation in terms of equipment cost, deployment cost, maintenance cost, energy cost, and even available space.

4.3.4 Power and Intensity

In the previous section, we performed two-dimensional analysis of the detection ratio and network scalability. In this section, we present the power and intensity of the received signal based on the transmitted power. We consider the threshold value for receiver sensitivity as 0.2 nW which is selected from the specifications of the modem we chose for our research. Once the leak is detected, the recorded values of power and intensity of the received signal are important for localizing the oil leak, which is discussed in Chapter 6. We present the results based on the topology we considered. For analyzing the power and intensity values of

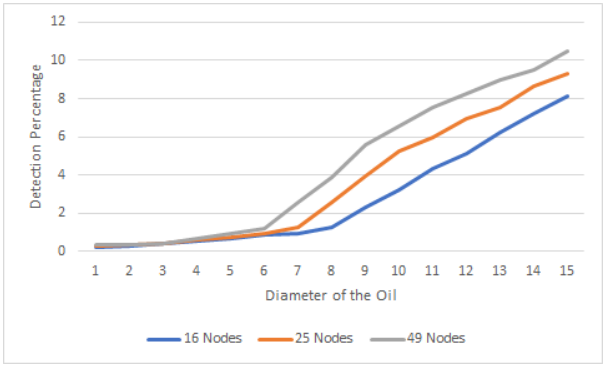

(a)

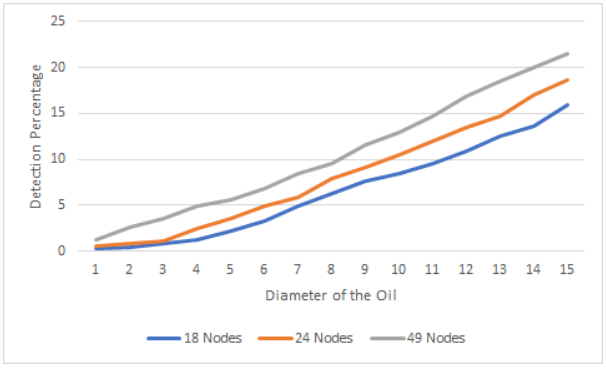

(b)

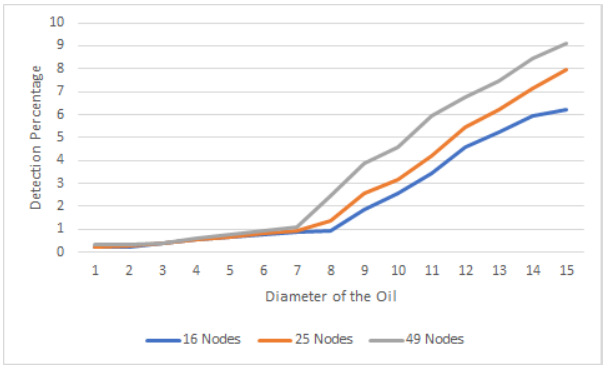

(c)

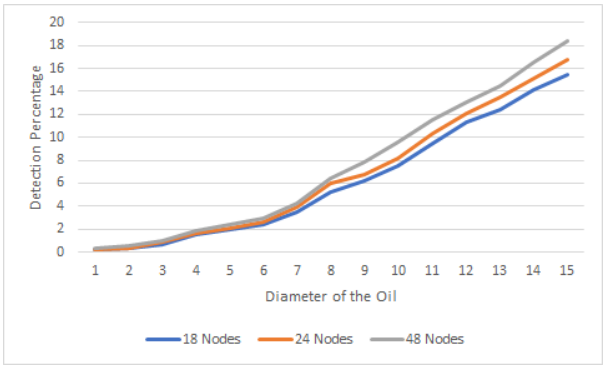

(d)

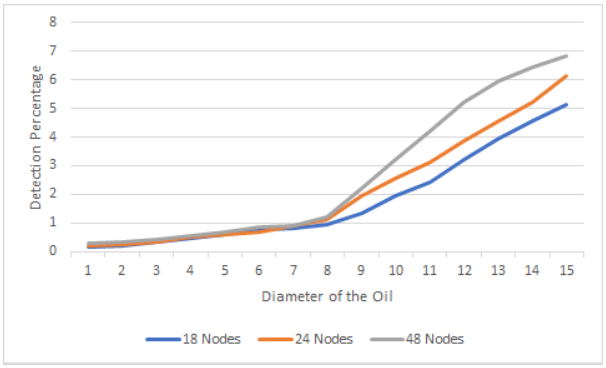

(e)

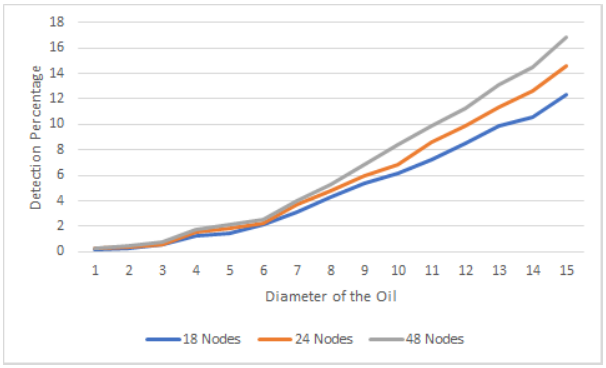

(f)

Figure 4.15: Network scalability based on two-dimensional analysis for rectangle-shaped leak

the received signal, we show the results based on three categories: square grid topology, concentric hexagonal topology without caisson, and concentric hexagonal topology with caisson. The results shown in Figure 4.16, 4.17, 4.18 are calculated for square grid topology with 49 nodes having 161 m as the distance between adjacent nodes and concentric hexagonal topology with 48 nodes having 1200 m as the diameter of the outer hexagon. We consider conical-shaped oil leak with a diameter of 3 m near the ocean floor for showing the results of power and intensity.

4.3.4.1 Square Grid Topology

For analyzing the results using square grid topology, we show the results based on 5 different source nodes. Based on their positions in the network, we choose nodes 7, 14, 13, 19, and 25 as the source nodes one at a time. In 7×7 square grid topology as shown in Figure 4.3, node 25 is the centre node having 8 immediate neighbours. The node 19 has 8 immediate neighbours, node 13 has 8 immediate neighbours, node 14 has 5 immediate neighbours, and node 7 has 3 neighbours.

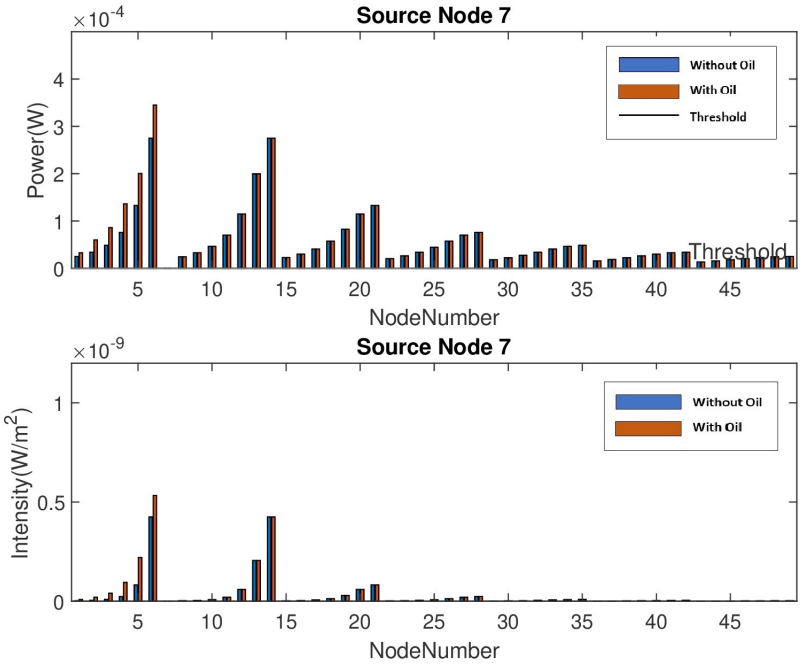

Figure 4.16: Power and intensity values based on two-dimensional analysis for square grid topology with 49 Nodes

Figure 4.16 shows the power and intensity values for source node 7. In Figure 4.16, the label "Without Oil" represents the results of power and intensity without the presence of oil and the label "With Oil" represents the results of power and intensity with the presence of oil. The nodes [1, 2, 3, 4, 5, 6] are the affected receiver nodes for the oil leak at the location (470, 483). We selected this leak location because this is between the neighbour node of the source node and the source node. If the leak location is at (482, 483), the number of affected receiver nodes will increase because that leak location is close to the source node. The leak location (482, 483) is close to node 7, around 1 m from node 7. The affected receiver nodes are [1, 2, 3, 4, 5, 6, 8, 9, 10, 11, 12, 13, 15, 16, 17, 18, 19, 22, 23, 24, 25, 29, 30, 31, 36, 37, 43].

If the leak is close to the source node, we can detect the presence of leaks effectively with

the help of many affected receiver nodes. Similarly, we show the affected receiver nodes for other 4 source nodes in Table 4.3. The leak location is not the same for all the source nodes we considered. We choose the leak locations rationally because we try to cover different locations to cover most cases.

Table 4.3: Power and Intensity of received signal for two-dimensional analysis of oil leak using square grid topology

Source node	Leak location	Affected receiver nodes
7	(470, 483)	[1, 2, 3, 4, 5, 6]
14	(470, 322)	[8, 9, 10, 11, 12, 13]
13	(300, 322)	[8, 9, 10, 11, 12]
19	(150, 161)	[15, 16, 17, 18]
25	(1, 40)	[4, 11, 18]

Table 4.3 lists the considered source node with leak location, and corresponding affected receiver nodes. We consider the threshold value for receiver sensitivity as 0.2 nW which is selected based on Modem 6 Sub-Mini specifications. If the receiver node is farther from the source node, the received power decreases, which means the received power is proportional to the distance.

4.3.4.2 Concentric Hexagonal Topology without Caisson

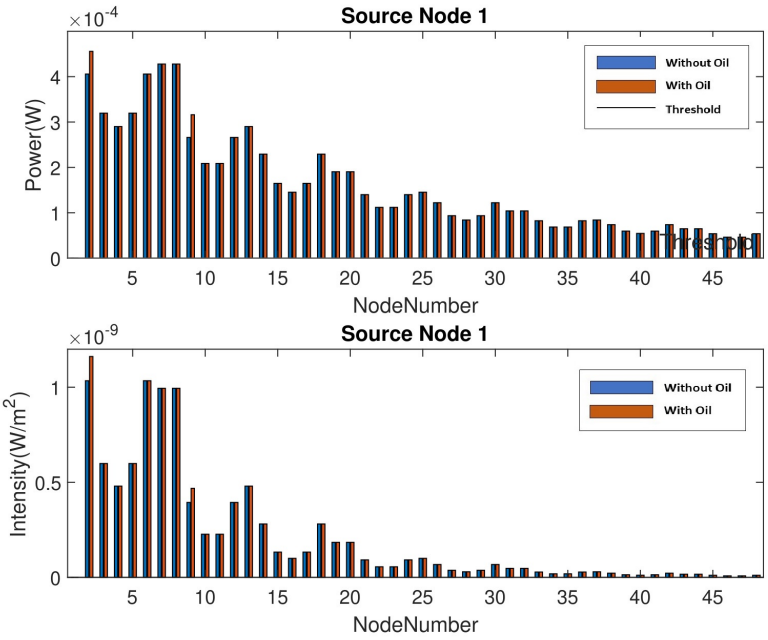

Figure 4.17: Power and Intensity values based on two-dimensional analysis for concentric hexagonal topology without caisson

We consider concentric hexagonal topology having 48 nodes without caisson, as shown in Figure 4.2 for analysis. We select nodes from each hexagon and present the power and intensity values by doing two-dimensional analysis. The selected source nodes are 1, 7, 13, 19, 25, 31, 37, and 43. The oil leak is assumed to be anywhere inside the outer hexagon having a maximal diameter of 1200 m. Figure 4.17 shows the results of power and intensity values for source node 1. In Figure 4.17, the label "Without Oil" represents the results of power and intensity without the presence of oil and the label "With Oil" represents the results of power and intensity with the presence of oil. The oil leak is assumed to be at the location (63, 55), and the receiver nodes affected by this oil leak are [2, 9].

Table 4.4: Power and Intensity of received signal for two-dimensional analysis of oil leak using concentric hexagonal topology without caisson

Source node	Leak location	Affected receiver nodes
1	(63, 55)	[2, 9]
7	(182, 2)	[25, 37]
13	(194, 113)	[20, 26, 32, 38, 44]
19	(301, 1)	[25, 37]
25	(324, 188)	[32, 38, 44]
31	(225, 1)	[7, 10, 22, 34]
37	(1, 262)	[39]
43	(225, 0)	[7, 10, 22]

We present the selected source nodes with leak location and corresponding affected receiver nodes in Table 4.4. For the concentric hexagonal topology without caisson, we assumed the same threshold value for receiver sensitivity to maintain consistency. For all the source nodes, the received power of the receiver nodes is above the threshold value.

4.3.4.3 Concentric Hexagonal Topology with Caisson

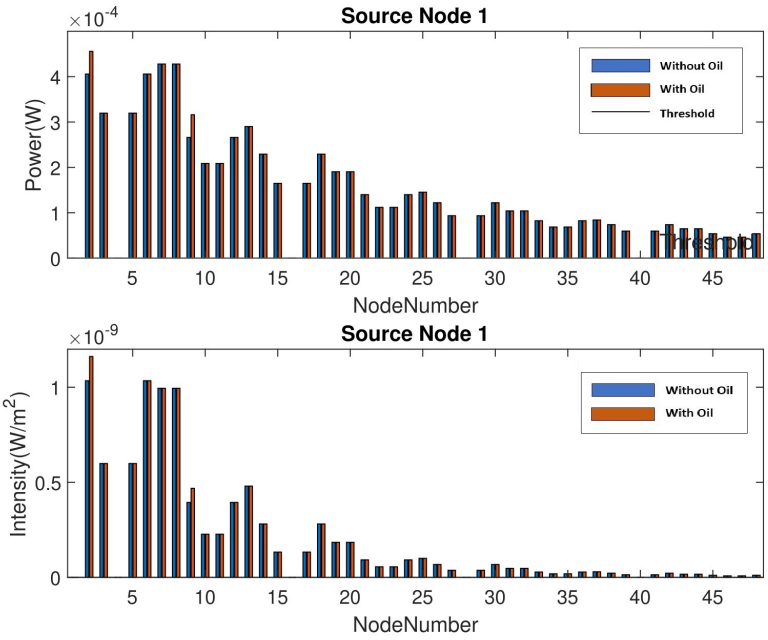

Figure 4.18: Power and Intensity values based on two-dimensional analysis for concentric hexagonal topology with caisson

We consider concentric hexagonal topology having 48 nodes with caisson, as shown in Figure 4.1 for analyzing the results. We select source nodes from each hexagon and present the received power and intensity results by performing two-dimensional analysis. The selected source nodes are 1, 7, 13, 19, 25, 31, 37, and 43. We considered the same source nodes for analyzing the power and intensity values for the concentric hexagonal topology without the caisson. The oil leak is assumed to be inside the inner hexagon having a maximal diameter of 150 m. For a topology with caisson, the area of interest is near the caisson because there are pipelines that carry oil from the rig to the tankers. Figure 4.18 shows the results of power and intensity values for source node 1. In Figure 4.18, the label "Without Oil" represents the results of power and intensity without the presence of oil and the label "With

Oil" represents the results of power and intensity with the presence of oil. The oil leak is assumed to be at the location (63, 55), and the receiver nodes affected by this oil leak are [2, 9].

Table 4.5: Power and Intensity of received signal for two-dimensional analysis of oil leak using concentric hexagonal topology with caisson

Source node	Leak location	Affected receiver nodes
1	(63, 55)	[2, 9]
7	(63, -55)	[40]
13	(63, -53)	[6]
19	(1, 61)	[15]
25	(1, 70)	[3]
31	(63, -55)	[4]
37	(1, 61)	[3, 10]
43	(1, 61)	[4]

We present the selected source nodes with leak location and corresponding affected receiver nodes in Table 4.5. For the concentric hexagonal topology with the caisson, the assumed threshold value for receiver sensitivity is 0.2 nW. When we compare Table 4.4 and Table 4.5, we find that the affected nodes are reduced for the concentric hexagonal topology with the caisson. Because of the caisson, the transmitted signal fails to reach the nodes located on the other side of the caisson as most of the sound gets absorbed by the concrete. The power of the receiver nodes without the oil leak is less than the power with oil leak because oil absorbs less sound than water. We discuss the results of localization in

Chapter 6.

Figures 4.16, 4.17, and 4.18 shows the results of power and intensity values of the received signal for the three different topologies. The received power of the nodes in the considered topology are above the threshold. We discuss the results of receiver sensitivity 0.2 μW in Appendix B for the same set of values considered for the receiver sensitivity 0.2 nW. For the 0.2 μW receiver sensitivity, the detection percentage is the same as the results of detection percentage for 0.2 nW receiver sensitivity. The only difference with 0.2 μW receiver sensitivity threshold is the received power of some of the nodes are less than the threshold. Using 0.2 nW receiver sensitivity, we get more affected nodes for some cases which is useful for locating the leak more precisely.

4.4 Summary

In this chapter, we focused on UWSN oil spills and proposed a leak detection method to detect the leak at the early stage effectively. We studied the detection ratio and the network scalability for different sized networks based on two-dimensional analysis. The proposed method can detect any shape of the oil leak and support more extensive networks. We then study the received power and the intensity of the signal from the source node. The results of received power, and intensity will be used for localizing the leak once the leak is detected, which is discussed in Chapter 6.

Based on the two-dimensional analysis, the proposed method gives a 73% detection ratio for the leak from the pipeline breakage. In comparison to two topologies we considered, the square grid topology covers less area and has higher node density than concentric hexagonal topology. The performance is better for concentric hexagonal topology compared to square grid topology. Our analysis shows that the proposed two-dimensional method detects the

leak at the early stage for most of the leak locations (73% leak locations), but the results of the detection percentage is smaller than the expectation mentioned in Chapter 1. We discuss how to improve the detection percentage in the next chapter.

Chapter 5

Three-Dimensional Analysis of Leak Detection

In chapter 4, we performed a two-dimensional analysis of the proposed leak detection method in UWSNs with a square grid topology and concentric hexagonal topology. In these two topologies, all the sensor nodes are assumed to be deployed on the seafloor, and their geometric positions form a square and hexagonal lattice. As mentioned in previous chapters, UWSNs are challenging compared to WSNs because of the cost of the acoustic devices and deployment cost.

In this chapter, we perform a three-dimensional analysis of the proposed detection method for detecting the leaks in UWSNs and investigate the operation of sensor nodes deployed in the ocean. As discussed in chapter 4, we consider two-dimensional UWSNs with concentric hexagonal topology and square grid topology. All these sensor nodes utilize wireless acoustic sensing for gathering information from other sensor nodes. The position information of all the sensor nodes is assumed to be known *a priori*. We perform a three-dimensional analysis of the proposed leak detection method to achieve a better detection ratio compared to a two-dimensional analysis, as discussed in Chapter 4. We study oil leak with different sizes

and shapes, which is located at various ocean depths, including at the seafloor, in the middle of the sea, and on the ocean surface. We perform three-dimensional analysis to investigate detection ratio of proposed method for different topology sizes. We study the performance evaluation of the proposed scheme for different sizes of leak under different topology density based on transmission range r. We then compare the results of two-dimensional analysis and three-dimensional analysis of the proposed method.

We organize this chapter as follows. In Section 5.1, we present the preliminaries for the three-dimensional analysis of the leak detection method. We perform the three-dimensional analysis of the leak detection method in Section 5.2. The performance evaluation of the proposed scheme is presented in Section 5.3. We conduct a theoretical analysis to compare the two-dimensional and three-dimensional analysis of the leak detection method in Section 5.4. Finally, we conclude the chapter in Section 5.5.

5.1 Proposed Leak Detection Method

5.1.1 Preliminaries

In this section, we present the three-dimensional analysis of the proposed leak detection method. For consistency, we use the same acoustic channel model discussed in Chapter 3. We utilize the semi-empirical formula, as mentioned in Section 4.1. Similar to the topology used in Chapter 4, we consider two different topologies in this chapter, having all the sensor nodes deployed in 2D space and their geometric positions form a square and hexagonal lattice.

Figure 5.1 shows the concentric hexagonal topology with caisson having 48 nodes. Figure 5.2 shows the concentric hexagonal topology having 48 nodes. Figure 5.3 shows the square grid topology having 49 nodes. The distance between the adjacent nodes is d. The position

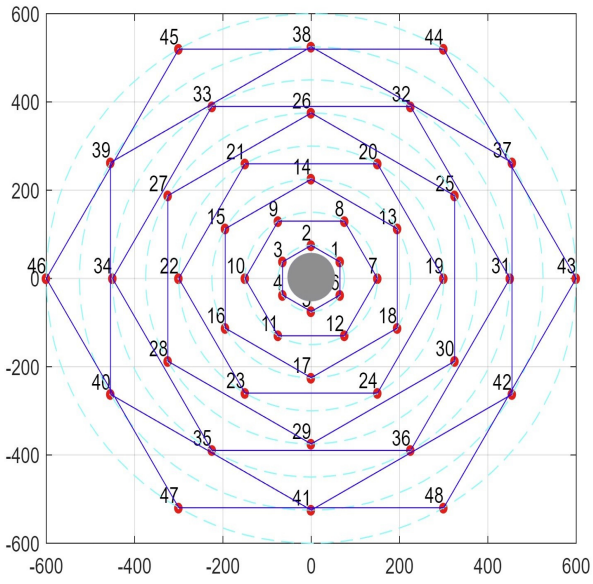

Figure 5.1: Illustration of concentric hexagonal topology with caisson

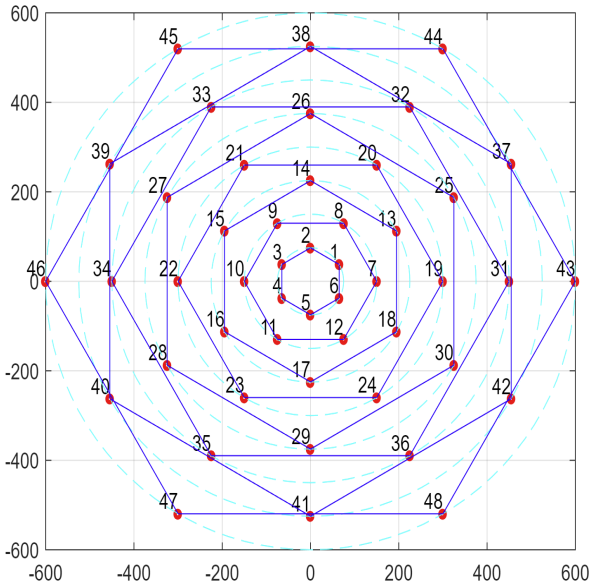

Figure 5.2: Illustration of concentric hexagonal topology without caisson

information of all the sensor nodes is assumed to be known *a priori*.

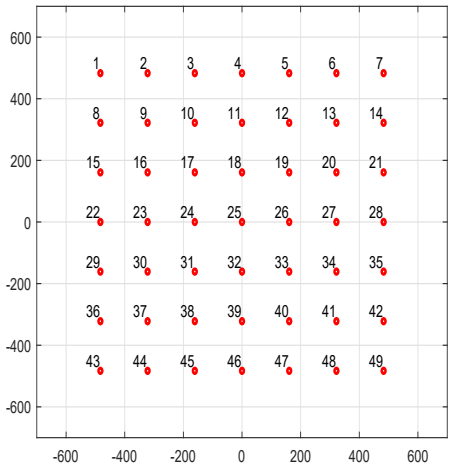

Figure 5.3: Illustration of square grid topology

5.1.2 Objective and Assumptions

In the previous chapter, we presented a two-dimensional analysis of the leak detection method for detecting the leak in UWSNs. The detection ratio of the two-dimensional analysis gives only 73%, which is lesser than our target result. Our objective is to achieve a 90% detection ratio for detecting leaks in UWSNs. To get a better detection ratio than two-dimensional analysis, we perform a three-dimensional analysis of the leak detection method. As we assumed in previous chapters, all the sensor nodes are equipped with sufficient battery energy. The nodes utilize wireless acoustic sensing for gathering information from the neighbour nodes. Each sensor node can act as a transmitter and receiver, but only one sensor node can act as a transmitter at a time. All the other nodes will receive the signal.

5.2 Three-dimensional analysis of Range Estimation Method

In this section, we present a three-dimensional analysis of the range estimation method proposed for detecting the oil leak in the underwater environment. Receiver nodes affected by the presence of oil leaks can be determined using this proposed technique.

The three-dimensional analysis of the proposed method works like two-dimensional analysis, but some of the reflection and refraction properties of three-dimensional analysis differ because we consider three-dimensional oil leak for evaluating the performance of the proposed method. We analyze the proposed scheme by considering two forms of signal: signal transmitted from the source travel through the oil as a line, and the signal transmitted from the source travels through the oil leak as an ellipse. This proposed method can determine the nodes affected by the presence of an oil leak by three-dimensional analysis. The power, intensity, and ToA of the signal received by the sensor of the affected nodes is recorded and used to detect and localize the oil leak.

We conduct a theoretical analysis to analyze the proposed method in this section. The oil leak is assumed to be at different depths of the ocean, such as near the seafloor, in the middle of the sea, and on the ocean surface. As mentioned in Section 5.1.1, we analyze the results for detecting the oil leak caused by two different factors: oil rig and pipeline breakage. We assume the oil leak can be present anywhere inside the topology area. We consider the oil leak at every 1 m interval within the selected topology area for two different cases for analyzing the results.

Case 1: We consider the transmitter and receiver as a single point.

Case 2: We consider transmitter and receiver as a circle with a diameter 10 cm.

We assume different sizes and shapes of oil leaks for better analyzing our proposed

method. We show the results based on network size and size of the leak.

5.2.1 Detection of Oil Leak from the Oil Rig

The oil rig platform area is considered to be most likely to experience an oil leak because the transport of oil to the tankers occurs near the drilling rigs. In our research, we consider the Hibernia oil rig platform as an example located at 315 km east-southwest off St. John's, Newfoundland and Labrador, Canada, in 80 m of water. Our proposed method applies to both shallow water and deep water acoustic channels. The Hibernia platform is based on a gravity based structure (GBS) with a concrete caisson of diameter 130 m in the middle of the rig placed on the seafloor. We consider concentric hexagonal topology having the concrete caisson in the middle with a height of 80 m and diameter of 130 m for our work. The sensor nodes are placed around the caisson in the hexagonal fashion, as shown in Figure 5.1. As mentioned earlier, the focussed area of our research for detecting the oil leak is near the caisson. We assume the oil leak to be anywhere inside the hexagon of maximal diameter 300 m. For evaluation purposes, we assume oil leaks at every 1 m inside the hexagon. For detecting the leak near the caisson, we consider the conical-shaped leak near the seafloor and cuboid-shaped leaked near the surface. We calculate results for two different cases, as mentioned earlier.

5.2.2 Detection of Oil Leak from the Pipeline Breakage

The oil leak from the pipeline is another common reason for oil spills in the underwater environment. For detecting the leak from the pipeline breakage, we consider two different topologies and analyze the proposed scheme based on these two topologies. To have a fair comparison between the two topologies, we consider the number of nodes and the distance between adjacent nodes in the topology based on Table 4.1.

For detecting the leak from the pipeline breakage, we assume leak at three different levels: near the seafloor, in the middle of the sea, and on the ocean surface. The results are calculated based on two different types of transmitter and receiver with two different transmission ranges. We consider both the direct and reflected propagation properties of the acoustic signal while evaluating the performance.

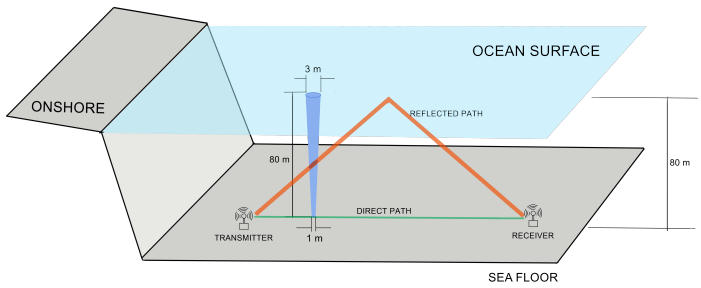

Figure 5.4: Illustration of conical-shaped leak

1. *Near the seafloor:* We assume a conical-shaped leak with a height of 80 m. The illustration of a conical-shaped leak is shown in Figure 5.4. Different leak diameter for the triangle-shaped leak corresponds to 188.5×10^3 $litres$, 523.6×10^3 $litres$, 2094.4×10^3 $litres$, or 4712.39×10^3 $litres$ of leaked oil.

2. *Middle of the sea:* For detecting the oil leak in the middle of the sea, we assume a frustum-shaped leak of height 10 m located at the height of 35 m from the seafloor, as shown in Figure 5.5. Different leak diameter for the frustum-shaped leak corresponds to 34.04×10^3 $litres$, 81.15×10^3 $litres$, 290.59×10^3 $litres$, or 630.93×10^3 $litres$ of leaked oil.

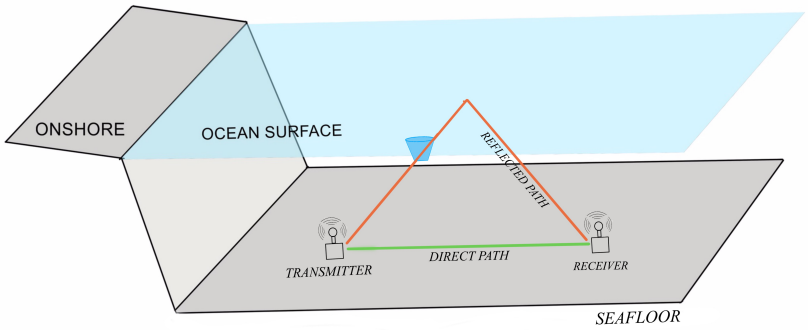

Figure 5.5: Illustration of frustum-shaped leak

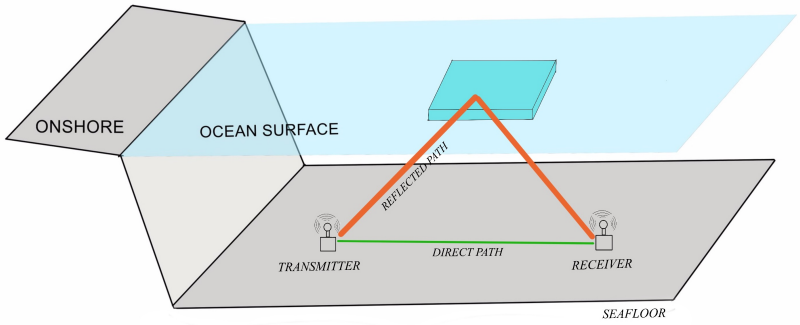

Figure 5.6: Illustration of cuboid-shaped leak

3. *Ocean surface:* After oil leak, the spilled oil reaches the ocean surface and spreads across the ocean because of the water current. We consider a cuboid-shaped leak for detecting the leak near the ocean surface, as shown in Figure 5.6.

5.3 Performance Evaluation

In this section, we study the performance evaluation of the proposed leak detection method by performing three-dimensional analysis. We evaluate the performance based on the detection ratio, network scalability, and power consumption. For consistency, we make assumptions similar to what is assumed for evaluating the leak detection method by two-dimensional analysis.

5.3.1 Evaluation Parameters

For evaluating the leak detection method by two-dimensional analysis, we selected the parameter values that correspond to Modem 6 Sub-Mini. Similarly, we consider the same set of parameters as listed in Table 6.3 for analyzing the leak detection method by three-dimensional analysis. We use the transmit power of 1 W, which corresponds to the transmit sound source level of 181 $dB\ re\ 1\ \mu Pa^2$, calculated from Equation 3.11.

5.3.2 Detection Ratio

In this section, we study the detection ratio of the proposed detection method with varying size, shape, and network size. We then discuss the scalability of the network with the help of the sensor nodes.

5.3.2.1 Near the oil rig

We investigate the detection ratio of the proposed scheme near the oil rig in this section. For the leak near the caisson, we assume the concentric hexagonal topology with 48 nodes, as shown in Figure 4.1. In Figures 5.7 and 5.8, we present the plot showing the detection percentage of the proposed detection method by three-dimensional analysis for two different

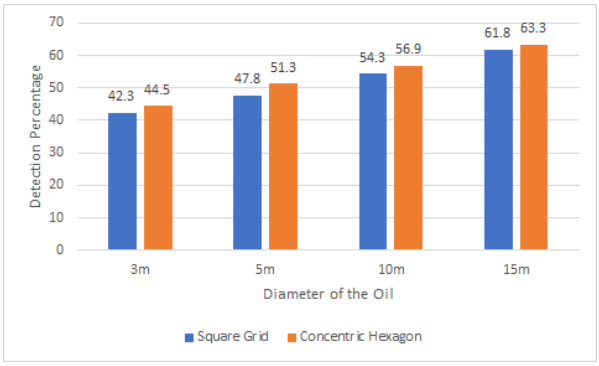

(a) Case 1 with transmission range 1000 m and 2000 m

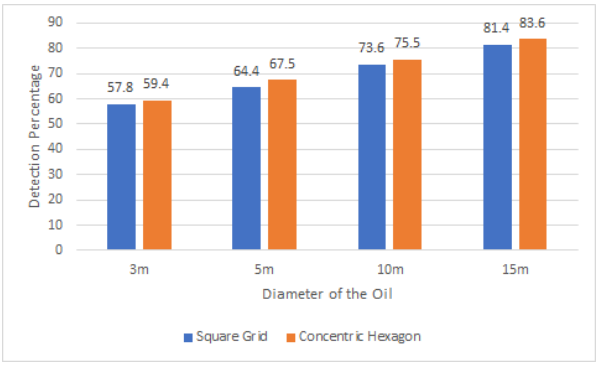

(b) Case 2 with transmission range 1000 m and 2000 m

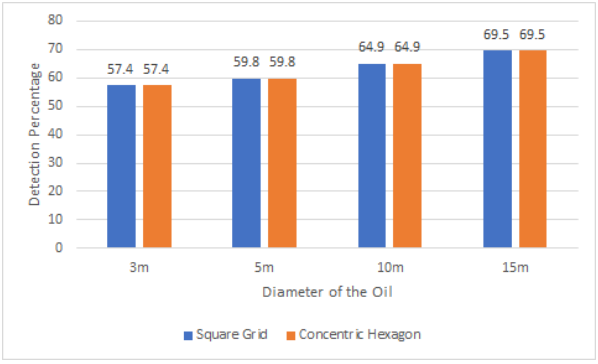

(c) Case 1 with transmission range 1000 m and 2000 m

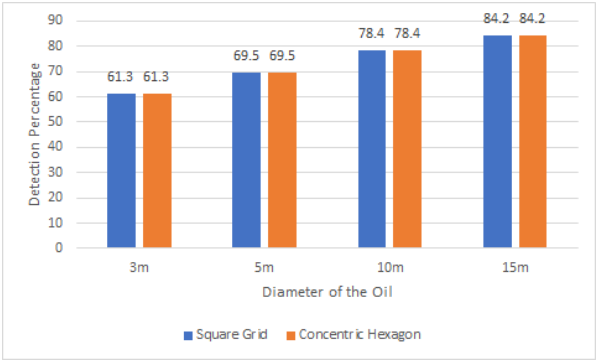

(d) Case 2 with transmission range 1000 m and 2000 m

Figure 5.7: Detection ratio based on three-dimensional analysis for conical-shaped leak near the oil rig

shapes of a leak near the oil rig: conical-shaped leak near the seafloor, and a cuboid-shaped leak near the ocean surface. As mentioned in Chapter 4, we show the results for two different sizes of concentric hexagonal topology. We calculate the results for two concentric hexagonal topologies to eliminate the blind spot areas. The blind spot areas refer to the oil leak location that is not detectable by the sensor nodes because of the topology structure. We calculate the results of the concentric hexagonal topology having the maximal diameter 350 m, 700 m,

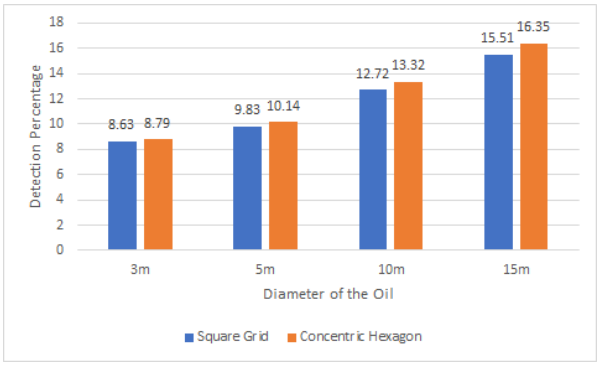

(a) Case 1 with transmission range 1000 m and 2000 m

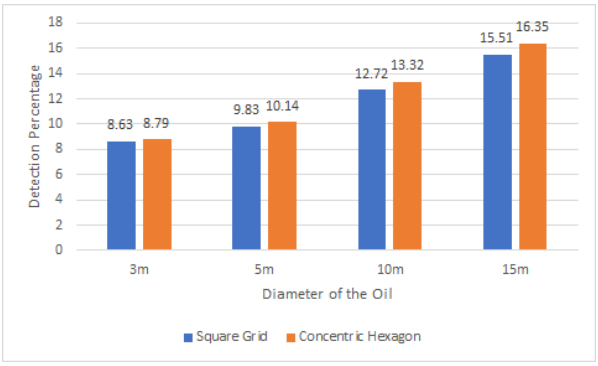

(b) Case 2 with transmission range 1000 m and 2000 m

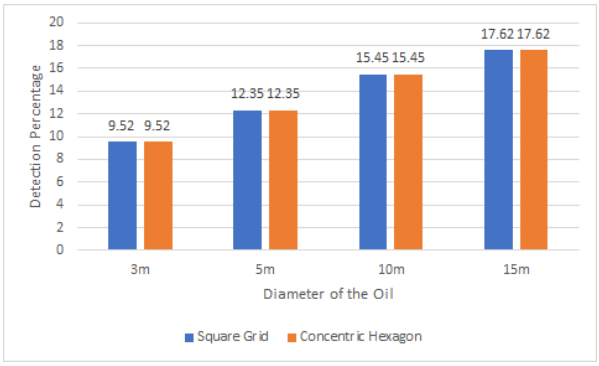

(c) Case 1 with transmission range 1000 m and 2000 m

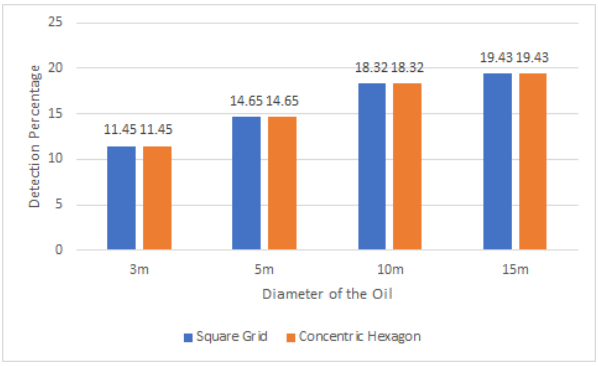

(d) Case 2 with transmission range 1000 m and 2000 m

Figure 5.8: Detection ratio based on three-dimensional analysis for cuboid-shaped leak on the surface near the oil rig

1050 m, 1400 m, 1750 m, 2100 m, 2450 m, and 2800 m. Since, for detecting the leaks near the caisson, we concentrate on the area near the caisson. In this case, the leak is assumed to be inside the hexagon of maximal diameter 350 m. Based on the dimensions we assumed, we experienced many blind spot locations because of the assumed maximal diameter of the hexagon. To avoid the blind spot and to get a better detection ratio compared to the topology dimensions we assumed before, we calculate the results for the concentric hexagonal

topology having the maximal diameter 150 m, 300 m, 450 m, 600 m, 750 m, 900 m, 1050 m, and 1200 m. We consider the oil leak diameter as 3 m, 5 m, 10 m, or 15 m.

Figures 5.7 and 5.8 show the detection percentage, which increases with the size of the leak. As mentioned in Section 4.2, the analysis shows the results for two cases with the transmission range as 1000 m and 2000 m. We consider the depth of the water column as 80 m. Figures 5.7a, 5.7b, 5.8a, and 5.8b show the results of the concentric hexagonal topology having the maximal diameter of the outer hexagon as 2800 m, and the Figures 5.7c, 5.7d, 5.8c, and 5.8d shows the results of the concentric hexagonal topology having the maximal diameter of the outer hexagon as 1200 m. All the subfigures from Figures 5.7 and 5.8 have two bars for each of the four diameters of the oil leak, as mentioned earlier. The first bar shows the result for the transmission range 1000 m, and the second bar shows the results for the transmission range 2000 m.

From Figure 5.7a, 5.7c, 5.8a, and 5.8c, we can see the increase in detection percentage in c compared to a. This is because the sensor nodes are placed closer to the caisson to avoid blind spots. If we compare Figures a and c with b and d, we can see the increase in detection percentage because of the transmitter and receiver's size. The detection percentage for the leak near the ocean surface is reduced almost by more than 80% because we consider the perfect reflection of the acoustic signal at the ocean surface.

5.3.2.2 From the Pipeline Breakage

In this section, we analyze the detection ratio of the proposed scheme for detecting the leak caused by pipeline breakage. For consistency, we consider the square grid topology with 49 nodes and concentric hexagonal topology with 48 nodes, as mentioned in the previous chapter for detecting the leak from the pipeline breakage. Figure 5.9, 5.10, and 5.11 shows the detection percentage of the proposed leak detection method for the leaks at different

ocean levels, including the leak near the seafloor, middle of the sea, and the ocean surface. As mentioned in the table 4.1, we consider the distance between the two adjacent nodes in the square grid topology as 161 m and the maximal diameter of the outer hexagon in the concentric hexagonal topology as 1200 m. The depth of the water column is 80 m.

1. *Near the ocean floor:* The oil leaked from the pipeline travels slowly to the surface in

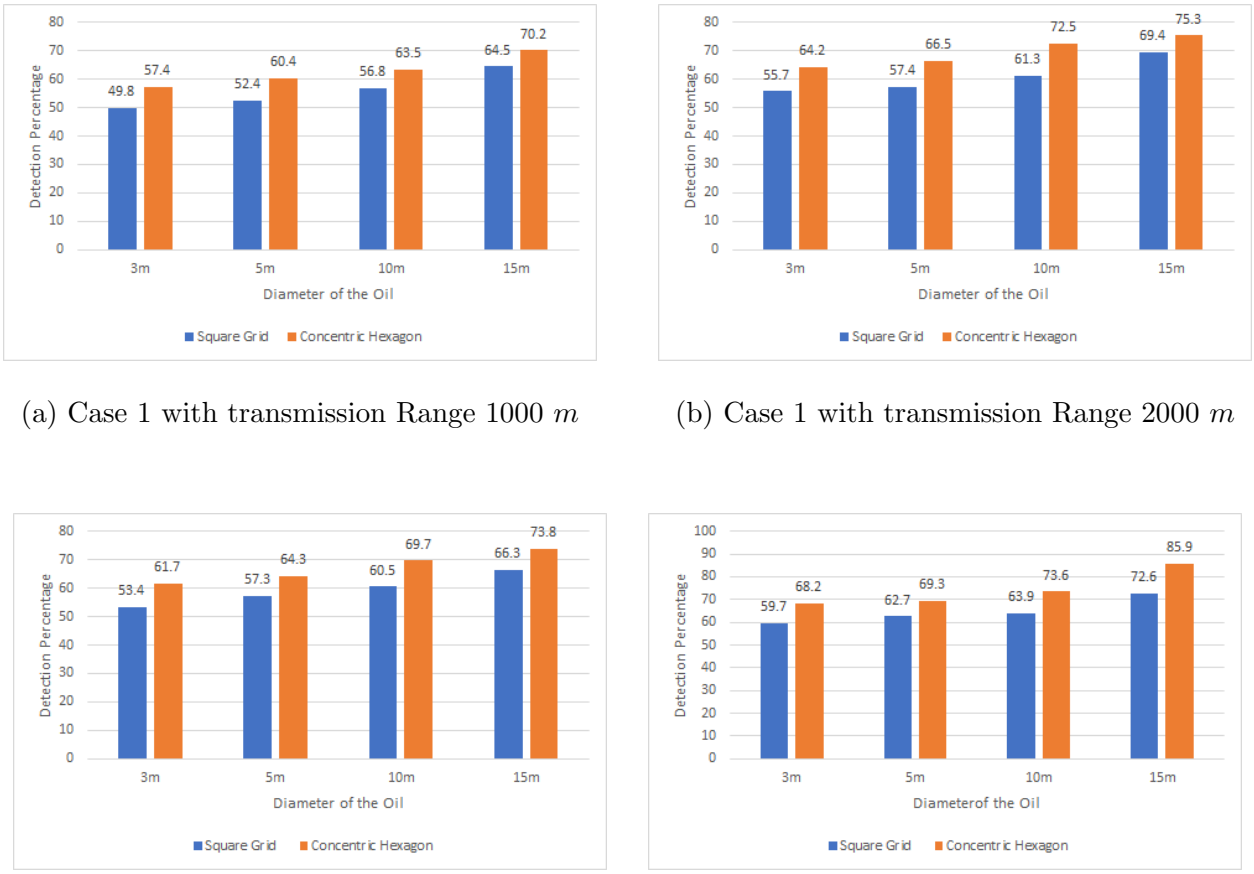

(a) Case 1 with transmission Range 1000 m

(b) Case 1 with transmission Range 2000 m

(c) Case 2 with transmission Range 1000 m

(d) Case 2 with transmission Range 2000 m

Figure 5.9: Detection ratio based on three-dimensional analysis for conical-shaped leak from the pipeline breakage

the form of a cone. The leaked oil starts spreading as a thin layer at the ocean surface because of the water currents. So, we consider a conical-shaped leak near the seafloor.

We study the results for different diameters of the oil leak, such as 3 m, 5 m, 10 m, or 15 m, using square grid topology and concentric hexagonal topology. Figure 5.9 shows the results of the detection ratio of a conical-shaped leak from the pipeline breakage for two cases mentioned in Section 4.2. The two bars in the figure represent the results of square grid topology and concentric hexagonal topology. From Figure 5.9, it is evident that the detection percentage increases with the size of the leak. Compared to all the four subfigures, Figure 5.9d shows the higher detection percentage because the transmission range is 2000 m, and the length of the transmitter and receiver is 10 cm. It is evident from the results that the proposed method using concentric hexagonal topology gives a better detection percentage than square grid topology.

2. *Middle of the sea:* For detecting the oil leak in the middle of the ocean, we consider a frustum-shaped leak in the middle of the sea about 30 m from the ocean floor. Once the oil leaks from the pipeline, it starts travelling to the surface. The leaked oil sometimes moves as slicks in the ocean. To detect that kind of oil slicks, we assume a frustum-shaped leak in the middle of the ocean. Similar to a conical-shaped leak, we consider different sizes of the frustum to understand the results better. The detection ratio of the frustum-shaped leak in the middle of the sea due to pipeline breakage is shown in Figure 5.10. Like the conical-shaped leak, Figure 5.10d gives a better detection percentage compared to all the other subfigures. For the leak with diameter 15 m, the detection percentage of the conical-shaped leak is about 85% with transmission range 2000 m for Case 2, whereas the detection percentage of a frustum-shaped leak is 70% with transmission range 2000 m for Case 2. This is because for a conical-shaped leak, the height of the cone is equal to the depth of the water that helps the sensor nodes to detect the leak easily compared to the frustum, which is just the section of the cone of height 10 m.

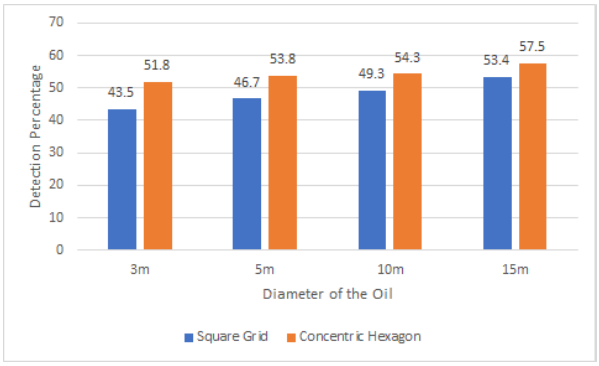

(a) Case 1 with transmission Range 1000 m

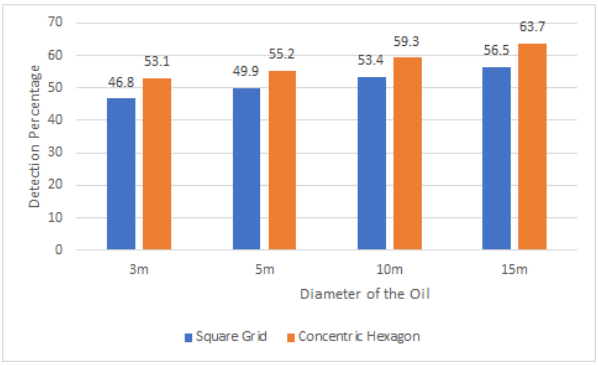

(b) Case 1 with transmission Range 2000 m

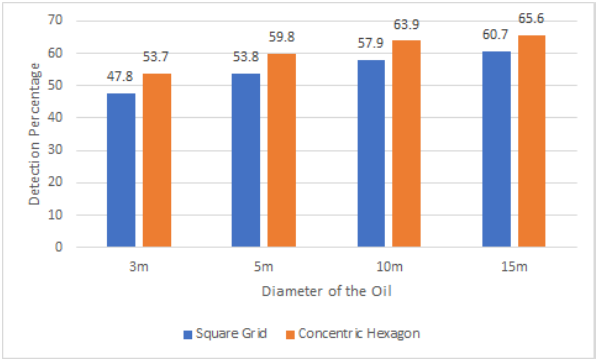

(c) Case 2 with transmission Range 1000 m

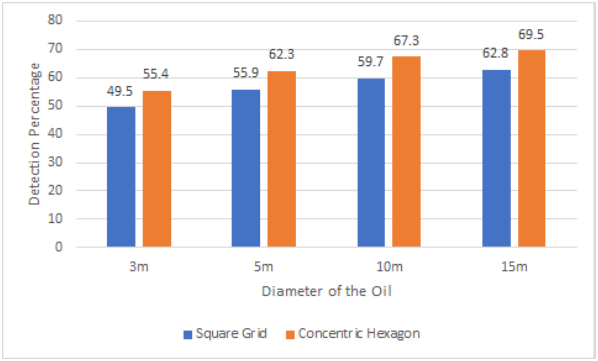

(d) Case 2 with transmission Range 2000 m

Figure 5.10: Detection ratio based on three-dimensional analysis for frustum-shaped leak in the middle of the ocean

3. *Ocean surface:* If the proposed method fails to detect the leak at the early stage, the spilled oil travels to the ocean and forms a thin layer of slick at the ocean surface. To detect that type of leak, we consider a cuboid-shaped leak at the ocean surface with varying sizes. Figure 5.11 illustrates the detection ratio of the cuboid-shaped leak for two different cases mentioned in Section 4.2. Compared to the detection percentage of a leak near the ocean floor, and in the middle of the sea, the detection percentage of a leak near the ocean surface is reduced by almost 70%. The detection percentage of a leak near the ocean surface with the diameter 15 m and transmission range 2000 m for

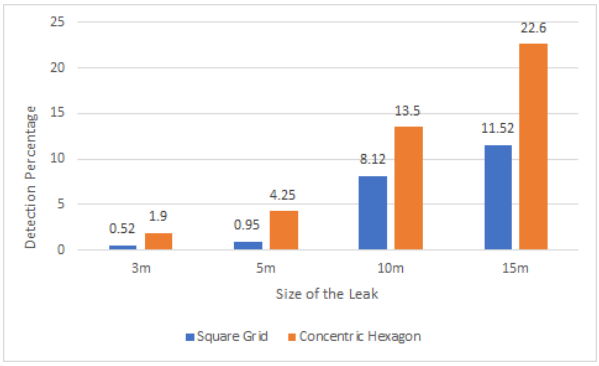

(a) Case 1 with transmission range 1000 m

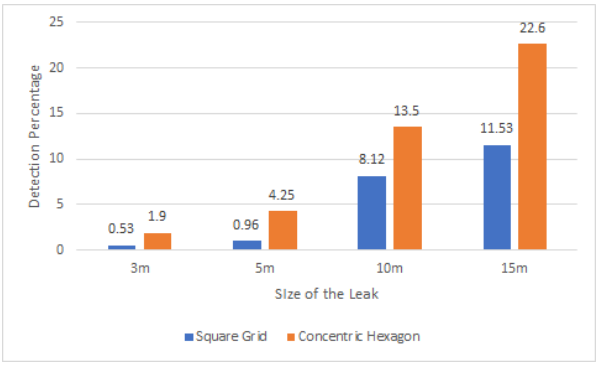

(b) Case 1 with transmission range 2000 m

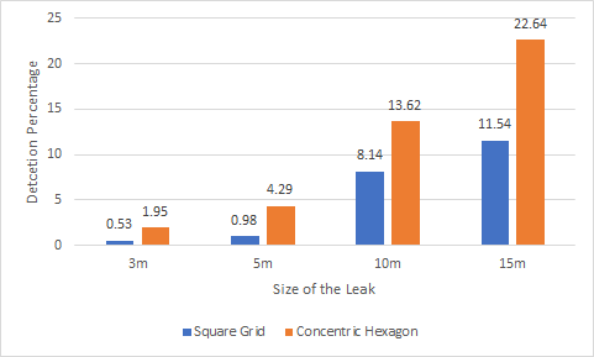

(c) Case 2 with transmission range 1000 m

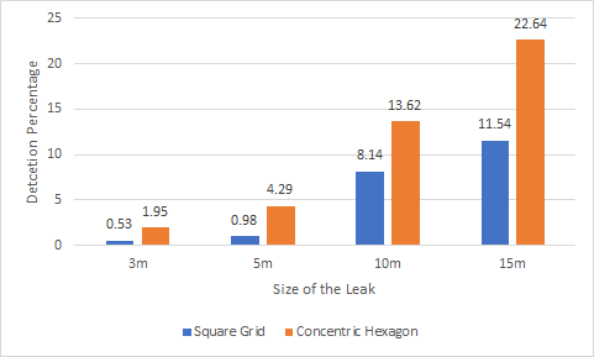

(d) Case 2 with transmission range 2000 m

Figure 5.11: Detection ratio based on three-dimensional analysis for cuboid-shaped leak near the ocean surface

10 cm transmitter and receiver is 23%, whereas it is 85% and 70% for the leak near the ocean floor and in the middle of the ocean for the same condition. The reason for the low detection percentage is because we assume a perfect reflection for surface leaks. We assume the perfect reflection of the acoustic signal at the ocean surface because of the ideal conditions studied in the literature study. We plan to extend our research to detect the oil leak without perfect reflection in the future.

From the above discussion, the detection percentage is directly proportional to the leak's size. From the above analysis, the concentric hexagonal topology covers more area with less

node density and gives better results than square grid topology. The detection percentage also varies with the transmission range and the length of transmitter and receiver. Because of the size and located ocean level of the leak, the detection ratio differs. Since, we assumed perfect reflection at the ocean surface, we are ignoring most of the signals which makes the proposed method to detect only 23% of the leak. Although, we assume perfect reflection at the ocean surface, for the leak near the seafloor, we achieved the detection ratio of 85% because of the direct path of the acoustic signal.

5.3.3 Network Scalability

In this subsection, we investigate the detection ratio of the proposed method with varying network size, size of the leak, and distance between adjacent nodes. Figures 5.12, 5.13, and 5.14 show the detection ratio under three different network sizes and three different distances between adjacent nodes. The topology is the same as what was shown in the previous section. We vary the diameter of the oil leak from 1 to 15 m. Figure 5.12 shows the plot for the detection percentage for the conical-shaped oil leak near the seafloor. Figure 5.13 shows the plot for the detection percentage for the frustum shaped oil leak in the middle of the ocean. Figure 5.14 shows the plot for the detection percentage for the cuboid-shaped oil leak on the ocean surface. The left three subfigures from the Figures 5.12, 5.13, and 5.14 shows the results for square grid topology, and the right three subfigures show the results for hexagonal grid topology.

From the above figures, the topology with more number of nodes provides a better detection percentage compared to the topology with less number of nodes. When there are many nodes in the given area, the possibility of detecting the leak increases. For example, the detection percentage of topology having 49 nodes in 161 m x 161 m gives better detection percentage than the topology having 25 nodes in 161 m x 161 m. Nevertheless, having more

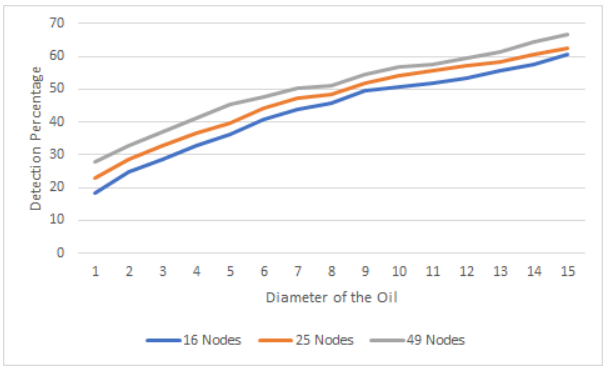

(a)

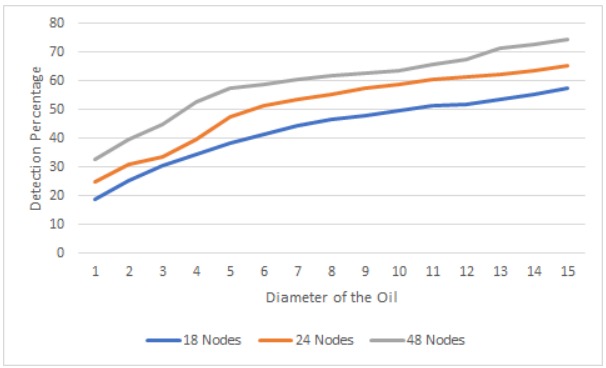

(b)

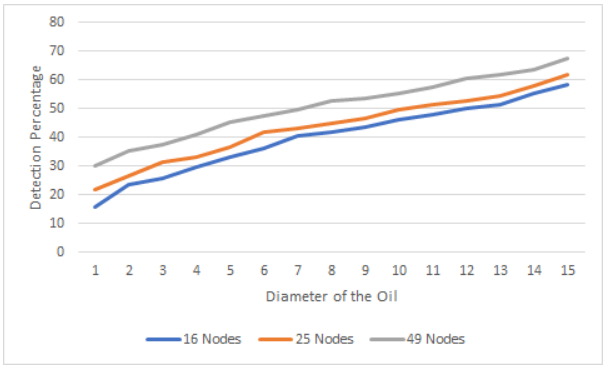

(c)

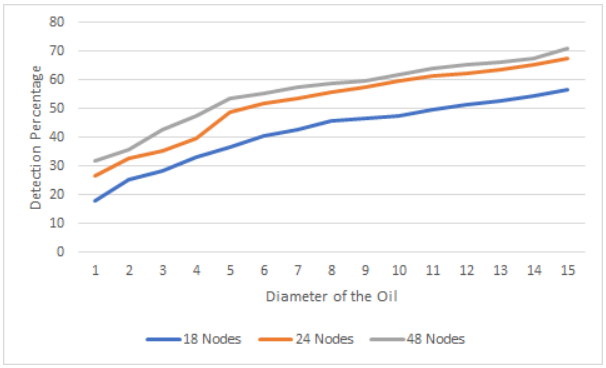

(d)

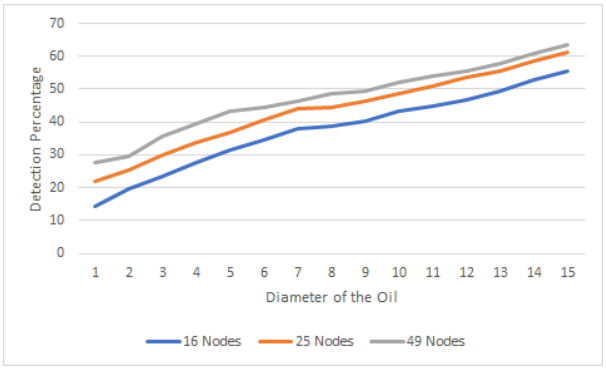

(e)

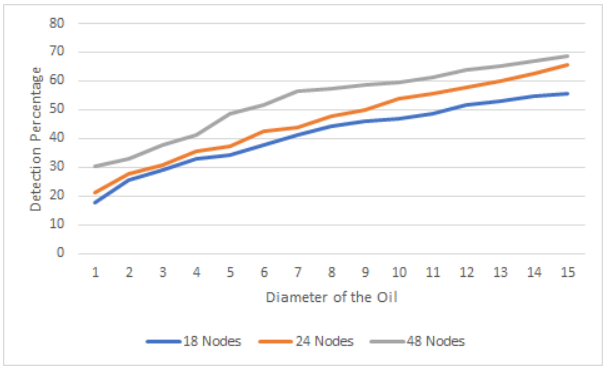

(f)

Figure 5.12: Network scalability based on three-dimensional analysis for conical-shaped Leak

nodes in the smaller area becomes unrealistic and the cost of deployment will be higher.

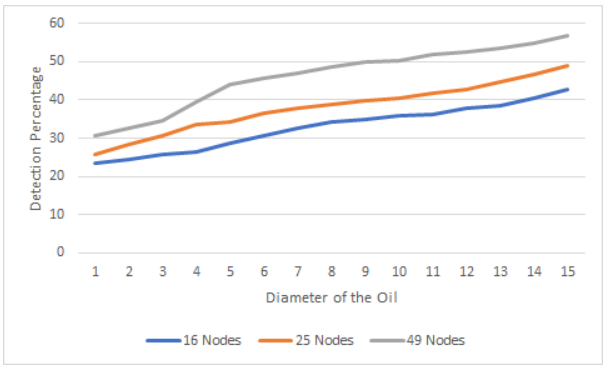

(a)

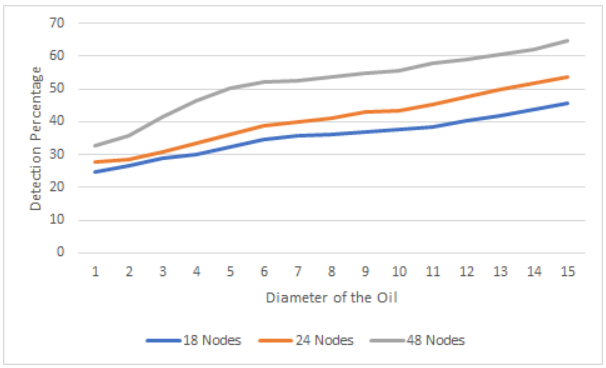

(b)

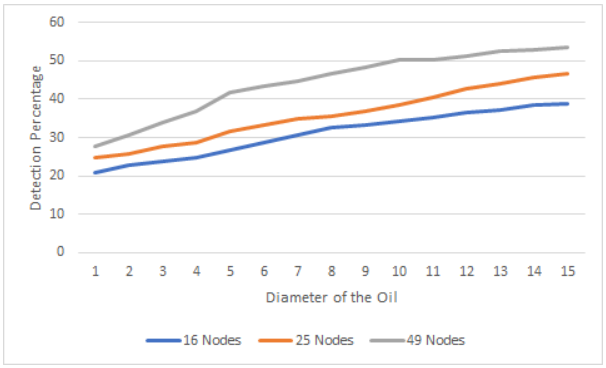

(c)

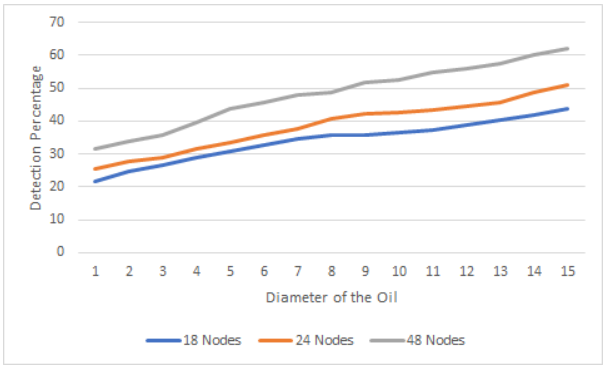

(d)

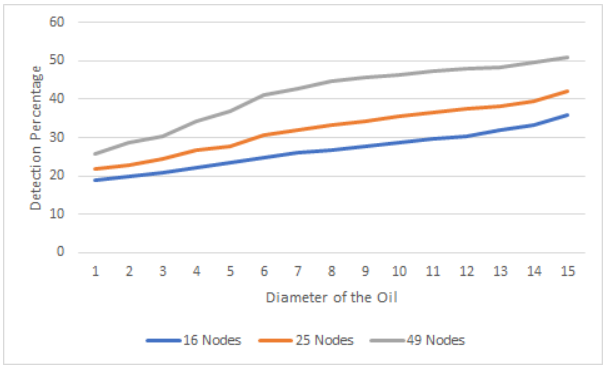

(e)

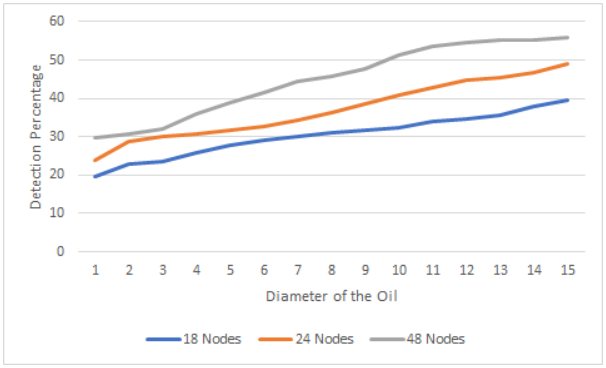

(f)

Figure 5.13: Network scalability based on three-dimensional analysis for frustum-shaped leak

5.3.4 Power and Intensity

The two-dimensional analysis of the power and intensity of the received signal was discussed in the previous chapter. In this section, we discuss the power and intensity of the received

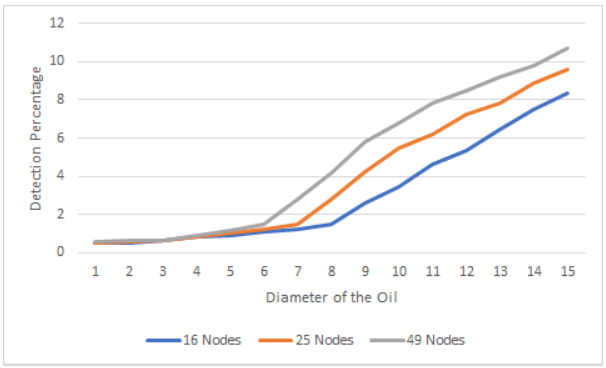

(a)

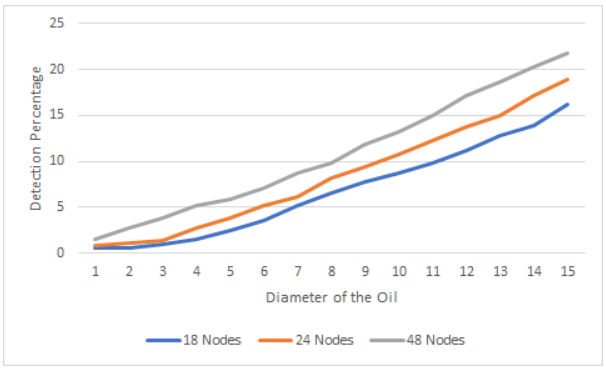

(b)

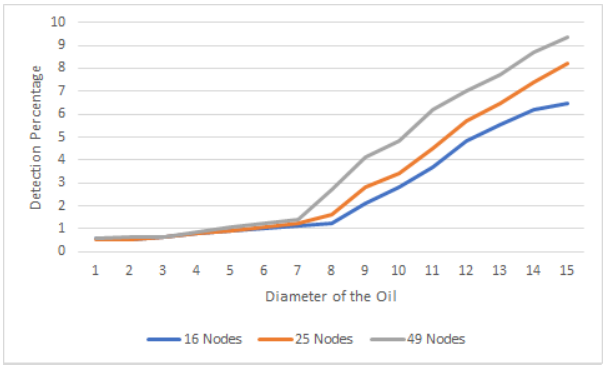

(c)

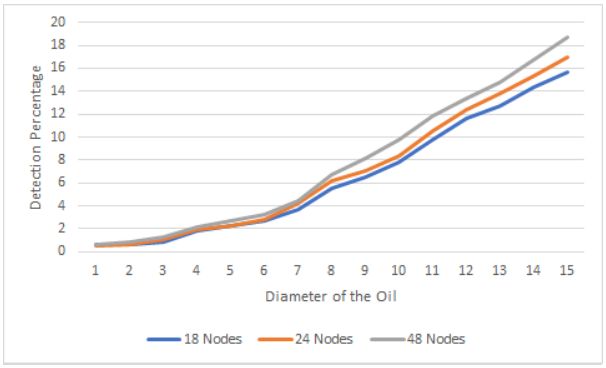

(d)

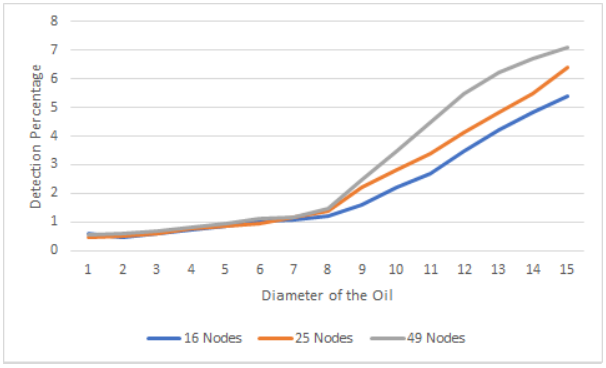

(e)

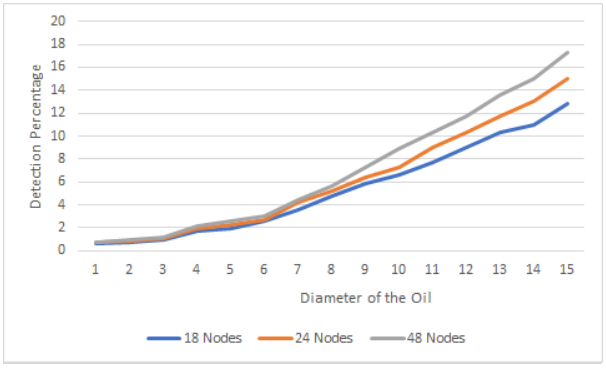

(f)

Figure 5.14: Network scalability based on three-dimensional analysis for cuboid-shaped leak

signal based on the assumed transmit power. We present the results of power and intensity for square grid topology, concentric hexagonal topology without caisson, and concentric hexagonal topology with caisson. The results shown in Figure 5.15, 5.16, 5.17 are calculated

for square grid topology with 49 nodes having 161 m as the distance between adjacent nodes and concentric hexagonal topology with 48 nodes having 1200 m as the diameter of the outer hexagon. We consider conical-shaped oil leak with a diameter of 3 m near the ocean floor for showing the results of power and intensity.

5.3.4.1 Square Grid Topology

For analyzing the results using square grid topology, we show the results based on 5 different source nodes. For consistency, we choose the same source nodes 7, 14, 13, 19, and 25 considered for two-dimensional analysis.

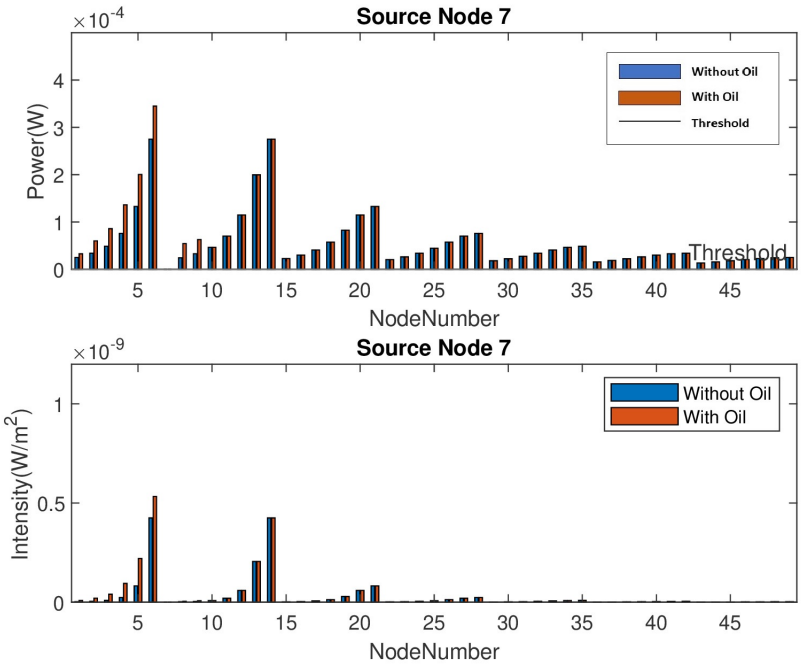

Figure 5.15: Power and Intensity values based on three-dimensional analysis for square grid topology with 49 Nodes

Figure 5.15 shows the power and intensity values for the source node 7. In Figure 5.15, the label "Without Oil" represents the results of power and intensity without the presence of

oil and the label "With Oil" represents the results of power and intensity with the presence of oil. The nodes 1, 2, 3, 4, 5, 6, 8, and 9 are the affected receiver nodes for the oil leak at the location (470, 483).

Table 5.1: Power and Intensity of received signal for three-dimensional analysis of oil leak using square grid topology

Source node	Leak location	Affected receiver nodes
7	(470, 483)	[1, 2, 3, 4, 5, 6, 8, 9]
14	(470, 322)	[1, 2, 8, 9, 10, 11, 12, 13, 15, 16]
13	(300, 322)	[1, 8, 9, 10, 11, 12, 15]
19	(150, 161)	[8, 15, 16, 17, 18, 22]
25	(1, 40)	[4, 11, 18].

From the three-dimensional analysis, Table 5.1 lists the considered source node with leak location, and corresponding affected receiver nodes. Similar to what we assumed for two-dimensional analysis, we consider the same threshold value for the three-dimensional analysis. It should also be noted that the transmitted signal reaching the nearest node is most likely to have a higher received power than the transmitted signal reaching the farthest node from the source node. For example, in the case of source node 7, the nearest node is 6 and 14, and the farther node is 42. The nearest and the farthest node varies for each source node.

5.3.4.2 Concentric Hexagonal Topology without Caisson

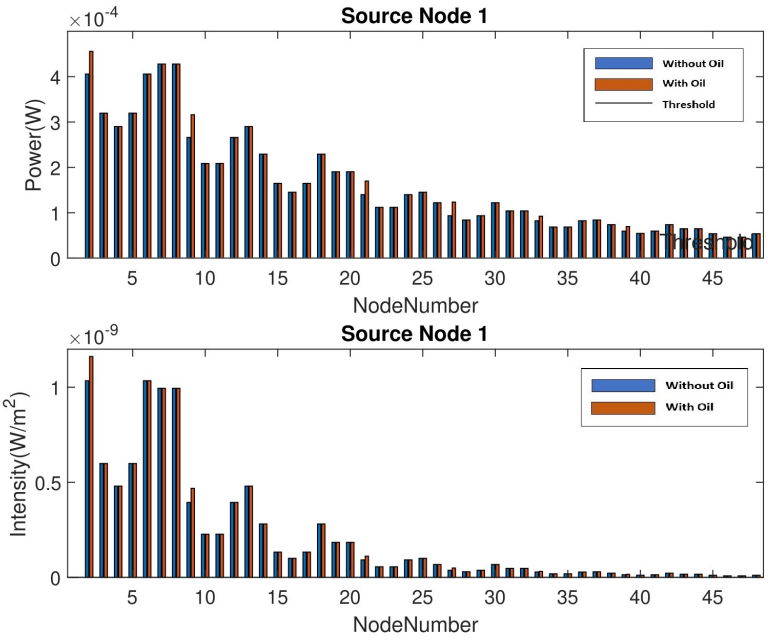

Figure 5.16: Power and Intensity values based on three-dimensional analysis for concentric hexagonal topology without caisson

We consider concentric hexagonal topology having 48 nodes without caisson, as shown in Figure 4.2 for analyzing the results. We select nodes from each hexagon and present the power and intensity values by doing three-dimensional analysis. We select the nodes 1, 7, 13, 19, 25, 31, 37, and 43 as the source node one at a time. The oil leak is assumed to be anywhere inside the outer hexagon, having the maximal diameter of 600 m. Figure 5.16 shows the results of power and intensity values for the source node 1. In Figure 5.16, the label "Without Oil" represents the results of power and intensity without the presence of oil and the label "With Oil" represents the results of power and intensity with the presence of oil. The oil leak is assumed to be at the location (63, 55) and the receiver nodes affected by this oil leak are [2, 9, 21, 27, 33, 39].

Table 5.2: Power and Intensity of received signal for three-dimensional analysis of oil leak using concentric hexagonal topology without caisson

Source node	Leak location	Affected receiver nodes
1	(63, 55)	[2, 9, 21, 27, 33, 39]
7	(182, 2)	[13, 25, 32, 37, 44]
13	(194, 113)	[14, 20, 25, 26, 32, 33, 37, 38, 44, 45]
19	(301, 1)	[25, 31, 32, 37, 43, 44]
25	(324, 188)	[20, 26, 32, 33, 37, 38, 44, 45]
31	(225, 1)	[7, 10, 22, 34]
37	(1, 262)	[39]
43	(225, 0)	[7, 10, 22]

We present the selected source nodes with leak location and corresponding affected receiver nodes in Table 5.2. We assumed the same threshold value for receiver sensitivity for concentric hexagonal topology, as we did for square grid topology. The received power for all the source nodes in this topology is above the assumed threshold value.

5.3.4.3 Concentric Hexagonal Topology with Caisson

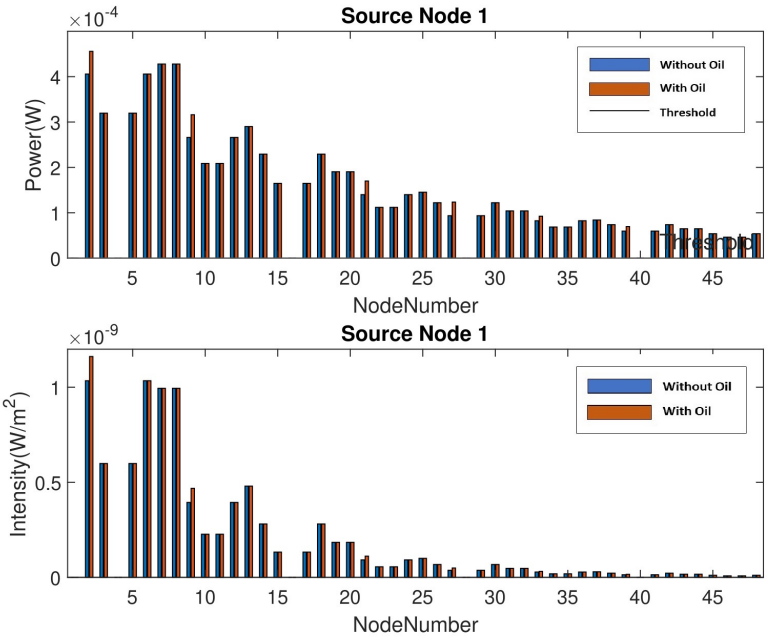

Figure 5.17: Power and Intensity values based on three-dimensional analysis for concentric hexagonal topology with caisson

We consider concentric hexagonal topology having 48 nodes with caisson, as shown in Figure 5.1 for analyzing the results. The source nodes are selected from each hexagon, and the power and intensity values are presented by performing three-dimensional analysis. The selected source nodes are 1, 7, 13, 19, 25, 31, 37, and 43. We considered the same source nodes for analyzing the power and intensity values for the concentric hexagonal topology without the caisson. The oil leak is assumed to be inside the inner hexagon having a diameter of 150 m. We mentioned in the previous section for the topology with the caisson, the leak is assumed to be in the inner hexagon because the area of interest is near the caisson.

Figure 5.17 shows the results of power and intensity values for the source node 1. In Figure 5.17, the label "Without Oil" represents the results of power and intensity without

the presence of oil and the label "With Oil" represents the results of power and intensity with the presence of oil.

The oil leak is assumed to be at the location [63, 55] and the receiver nodes affected by this oil leak are [2, 9, 21, 27, 33, 39].

Table 5.3: Power and Intensity of received signal for three-dimensional analysis of oil leak using concentric hexagonal topology with caisson

Source node	Leak location	Affected receiver nodes
1	(63, 55)	[2, 9, 21, 27, 33, 39]
7	(63, -55)	[40]
13	(63, -53)	[6]
19	(1, 61)	[15]
25	(1, 70)	[3]
31	(63, -55)	[4]
37	(1, 61)	[3, 10]
43	(1, 61)	[4]

We present the selected source nodes with leak location and corresponding affected receiver nodes in Table 5.3. We assume the threshold value for receiver sensitivity as 0.2 nW for the concentric hexagonal topology with the caisson. From Tables 5.2 and 5.3, we can see the number of affected nodes is reduced for the concentric hexagonal topology with the caisson. Because of the caisson, the transmitted signal fails to reach the nodes located on the other side of the caisson.

From the above sections, the power of affected receiver nodes with the presence of oil

is high compared to the power of the affected receiver nodes without oil. These power and intensity values are used for localizing the leak in the underwater environment. We will further discuss the results of localization using these values in Chapter 6.

Figures 5.15, 5.16, and 5.17 shows the results of power and intensity values of the received signal for the three different topologies. The received power of the nodes in the considered topology are above the threshold. We discuss the results of receiver sensitivity 0.2 μW in Appendix B for the same set of values considered for the receiver sensitivity 0.2 nW. For the 0.2 μW receiver sensitivity, the detection percentage is the same as the results of detection percentage for 0.2 nW receiver sensitivity. The only difference with 0.2 μW receiver sensitivity threshold is the received power of some of the nodes are less than the threshold. Using 0.2 nW receiver sensitivity, we get more affected nodes for some cases which is useful for locating the leak more precisely.

5.4 Comparison of Two-Dimensional Analysis and Three-Dimensional Analysis

Table 5.4: Comparison of the results for square grid topology

Oil leak	Two-Dimensional	Three-Dimensional
Conical-Shaped Leak	69.5	72.6
Frustum-Shaped Leak	53.6	62.8
Cuboid-Shaped Leak	10.47	11.54

Table 5.5: Comparison of the results for concentric hexagonal topology without the caisson

Oil leak	Two-Dimensional	Three-Dimensional
Conical-shaped leak	73.2	85.9
Frustum-shaped leak	61.5	69.5
Cuboid-shaped leak	21.5	22.6

Table 5.6: Comparison of the results for concentric hexagonal topology with the caisson

Oil leak	Two-Dimensional	Three-Dimensional
Conical-shaped leak	82.9	84.2
Cuboid-shaped leak	17.7	19.4

In this section, we compare the results of the proposed method discussed in Chapter 4 and Chapter 5. In Chapter 4, we discussed the results based on square grid topology and concentric hexagonal topology. For all the cases we assumed, the detection percentage increases with the size of the leak. For concentric hexagonal topology with caisson, we consider the leak within the innermost hexagon because we focus on the leak that happens because of the caisson. For concentric hexagonal topology without caisson, we consider the leak to be present inside the topology area. From the results obtained, the proposed method for detecting a three-dimensional leak gives better results than a two-dimensional leak. We tabularized the detection percentage of the two-dimensional and three-dimensional leak for square grid topology with 49 nodes and concentric hexagonal topology with 48 nodes. Table 5.4 shows the detection percentage of the two-dimensional leak and three-dimensional leak for

the square grid topology. Table 5.5 shows the detection percentage of the two-dimensional leak and three-dimensional leak for the concentric hexagonal topology without caisson. Table 5.6 shows the detection percentage of the two-dimensional leak and three-dimensional leak for the concentric hexagonal topology with caisson. It is clear from the results that the detection percentage for a three-dimensional leak is better than a two-dimensional leak. All three Tables 5.4, 5.5, and 5.6 show the result for the oil leak with a diameter of 3 m. The concentric hexagonal topology gives a better detection percentage although the node density is lower compared to square grid topology.

We prefer concentric hexagonal topology over square grid topology because the results of concentric hexagonal topology for detecting the oil leak are better than the results of square grid topology. We have tabularized the number of nodes and distance between adjacent nodes in Table 4.1. Based on the entries from Table 4.1, we compare the results of square grid topology and concentric hexagonal topology. Based on nodes in the topology network, concentric hexagonal topology covers more leak locations than square grid topology for the same area.

5.5 Summary

In this chapter, we focused on the issue of oil spills in UWSN. To be realistic and to achieve a better detection percentage, we proposed a leak detection method to detect the leak at the early stage by three-dimensional analysis. We studied the detection ratio and the network scalability for different sized networks. Our analysis shows that the three-dimensional analysis of the proposed method provides a better detection percentage of 85% compared to two-dimensional analysis, which gave the detection percentage of 73% discussed in Chapter 4. The proposed method can be applied to detect any shape of the oil leak and support more

extensive networks. We then study the receiving power and the intensity of the receiving signal from the source node. The results of received power and intensity will be used for localizing the leak, which is discussed in Chapter 6. The proposed scheme is limited to detect the oil spills but can be extended to detect other types of targets such as tracking ships, icebergs using different regular topology. Finally, we compare the results of two-dimensional analysis and three-dimensional analysis of the proposed scheme. Our proposed method provides the detection percentage of 85% for the concentric hexagonal topology with 48 nodes. Although, our proposed method did not achieve the expected results as mentioned in Chapter 1, results of the three-dimensional analysis are better compared to the results of the two-dimensional analysis. For obtaining the detection results, we use point-to-point approach for a particular leak location to identify how many nodes can detect that particular leak location. But, we use cooperative approach for localizing the leak which we discuss in Chapter 6. We plan to extend our algorithm to improve the detection ratio and to detect other types of targets in the underwater environment.

Chapter 6

Localization of Leak

In previous chapters, we studied oil spill detection problems in UWSNs with square grid topology and concentric hexagonal topology for long-term marine monitoring applications. The advancement of UWSNs further brings new challenges for localization in the underwater environment. In this chapter, we propose a cooperative localization scheme for localizing oil leaks in the underwater environment. Using the information from other adjacent sensor nodes, the location of the leak is determined approximately. The proposed algorithm locates the leak approximately by using received power and estimated arrival time of the received signal at the particular sensor node based on the transmitted power from the source node.

Chapter 6 is subdivided into three sections. Section 6.1 describes the basic cooperative scheme for localization and presents the proposed localization algorithm. Section 6.2 will evaluate the performance of the proposed algorithm, and conclusions are drawn in Section 6.3.

6.1 Cooperative Scheme for Localization

Localization is essential for many applications, including target detection such as oil spills, illegal fishing ship tracking, and other targets in the underwater environment. The cooperative localization is the most used technique for improving the performance by utilizing the information from adjacent sensor nodes. Localization is classified into a centralized scheme and a distributed scheme. In centralized localization, the central nodes in the network collect and process data for localizing the event. In distributed localization, each sensor node has its computational ability to handle data from the neighbouring nodes. Hence, the distributed localization scheme is more suitable for the underwater wireless sensor network localization. In this chapter, we consider the scenario where the sensor nodes are used for localization by gathering the information of adjacent sensor nodes.

6.1.1 Problem Description

In UWSNs, the marine environment is often affected by the oil spill because of the pipeline breakage or other factors near the oil rig. It is essential to localize the leak location at the earliest to prevent the spread of leaked oil into the ocean. Therefore, the whole problem is to design a cooperative localization algorithm for localizing the oil leak in UWSNs. Since, two-dimensional analysis for leak detection method did not give the expected results as mentioned in Chapter 1, we consider three-dimensional analysis for localization of leak. To localize the leak, the sensor nodes gather information from the adjacent sensor nodes using a cooperative technique.

6.1.2 Basic Cooperative Scheme

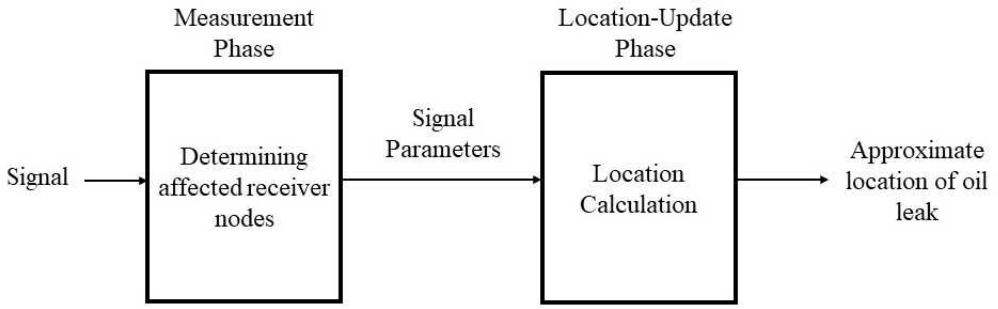

Figure 6.1: Phases in localization

In the underwater acoustic channel, the transmission loss is related to the distance between the sound source and the receiver. The concept of cooperation in the underwater wireless networks is new, which relies on direct communication between the nodes. The information collected and communicated by the sensor node is useful in conjunction with the node's location knowledge. In the previous section, a sensor node, which is an intended transmitter, transmits the sound signal, and all the other sensor nodes in the topology receive the signal. There are two phases in the proposed cooperative scheme, including the measurement phase and location-update phase, as shown in Figure 6.1.

6.1.2.1 Measurement Phase

In the measurement phase, the sensor nodes affected by the presence of oil leaks are determined based on the received signal power and estimated arrival time. The measurement phase is often affected by uncertainty due to noise, multipath, interference, and other environmental effects.

6.1.2.2 Location-Update Phase

The second phase is the location-update phase, where the sensor nodes infer their state based on, estimated signal metrics, and state information of neighbouring nodes. Based on the affected nodes determined from the measurement phase, the approximate location of the oil leak is determined.

6.1.3 Assumptions

Table 6.1: Structure of signal metrics table stored in each node

Node ID	Received power	Estimated ToA	Distance	Immediate neighbours

Table 6.2: Structure of information table stored in each node

Node ID	Priority list	Waiting time	IMMAFFECT	AFFECT	CLEAR

For localizing the leak, we make some assumptions about the sensor nodes and the topology. The sensor nodes are deployed in the two-dimensional area in a square grid or concentric hexagonal topology. All the sensor nodes are equipped with sufficient battery life, and the position information of all sensor nodes is assumed to be known *a priori*. While deploying the sensor nodes in UWSNs, each sensor node is embedded with the information in the form of Table 6.1 such as received power, estimated arrival time of the received signal with

respect to the *node ID*, and distance from the other nodes. Each sensor node also contains information about immediate neighbour nodes. For the given topology, the source node is selected based on the order of *nodeID*, i.e. 1, 2, 3, . . . ,*n*. Each sensor node has another table as shown in Table 6.2 having the information about waiting time, a priority list with respect to the *nodeID*. The priority list for each source node is decided based on the distance between the source node and the other receiver nodes. The closest node to the source node is given a higher priority. If the distance between the source node and two or more receiver nodes are the same, the priority is given to the node in the order of *nodeID*. For source node 1, the distance between node 1 and node 2 is the same as the distance between node 1 and node 6. In such a case, the priority is first given to node 2 and then to node 6. Table 6.2 also have *IMMAFFECT*, *AFFECT* and *CLEAR* field which updates during the process. For example, for the source node 1, node 7 is the affected receiver node for the leak location (470, 483). But, node 7 is not an immediate neighbour node of node 1. Since, node 7 is affected receiver node and not immediate neighbour node of source node, it sends the *AFFECT* message to other nodes. The field *AFFECT* in the Table 6.2 is now filled with node 7. If node 7 was the immediate neighbour node of the source node, then it sends *IMMAFFECT* message to the other nodes, and *IMMAFFECT* in the table is filled with the value 7. Once the localization process is complete, the process restores to the original state, and the source node is set to 1 by default.

6.1.4 Localization Algorithm

The following terms are used in the Localization algorithm.

1. *tx:* node that is transmitting the signal to other nodes (*receiverNodes*) in the topology. By default, the *tx* is set to 1. The next *sourceNode* is selected based on the *receiverNodes* and its signal metrics.

2. *receiverNodes:* The nodes that are within the transmission range r of the *sourceNode*, are considered as *receiverNodes*.

3. *previousSourceNode:* When the next *sourceNode* becomes the *sourceNode*, the current *sourceNode* becomes *previousSourceNode*.

4. *nodeID:* The identity of each node (1, 2, ..., n).

5. *nNodes:* Number of nodes in the topology.

6. *IMMAFFECT nodes:* The *receiverNodes* affected by the presence of oil leak which are the immediate neighbours of *sourceNode*.

7. *AFFECT nodes:* The *receiverNodes* affected by the presence of oil leak but not the immediate neighbour of *sourceNode*.

8. *S: S* represents the set which contains the pair of nodes affected by the presence of oil leak.

9. *receivedSignalMetrics:* Received Signal metrics include received power, intensity, time of arrival of the received signal.

10. *estimatedSignalMetrics:* Estimated Signal metrics include estimated power, estimated intensity, estimated time of arrival of the signal that a node should get from the received signal when there is no oil leak.

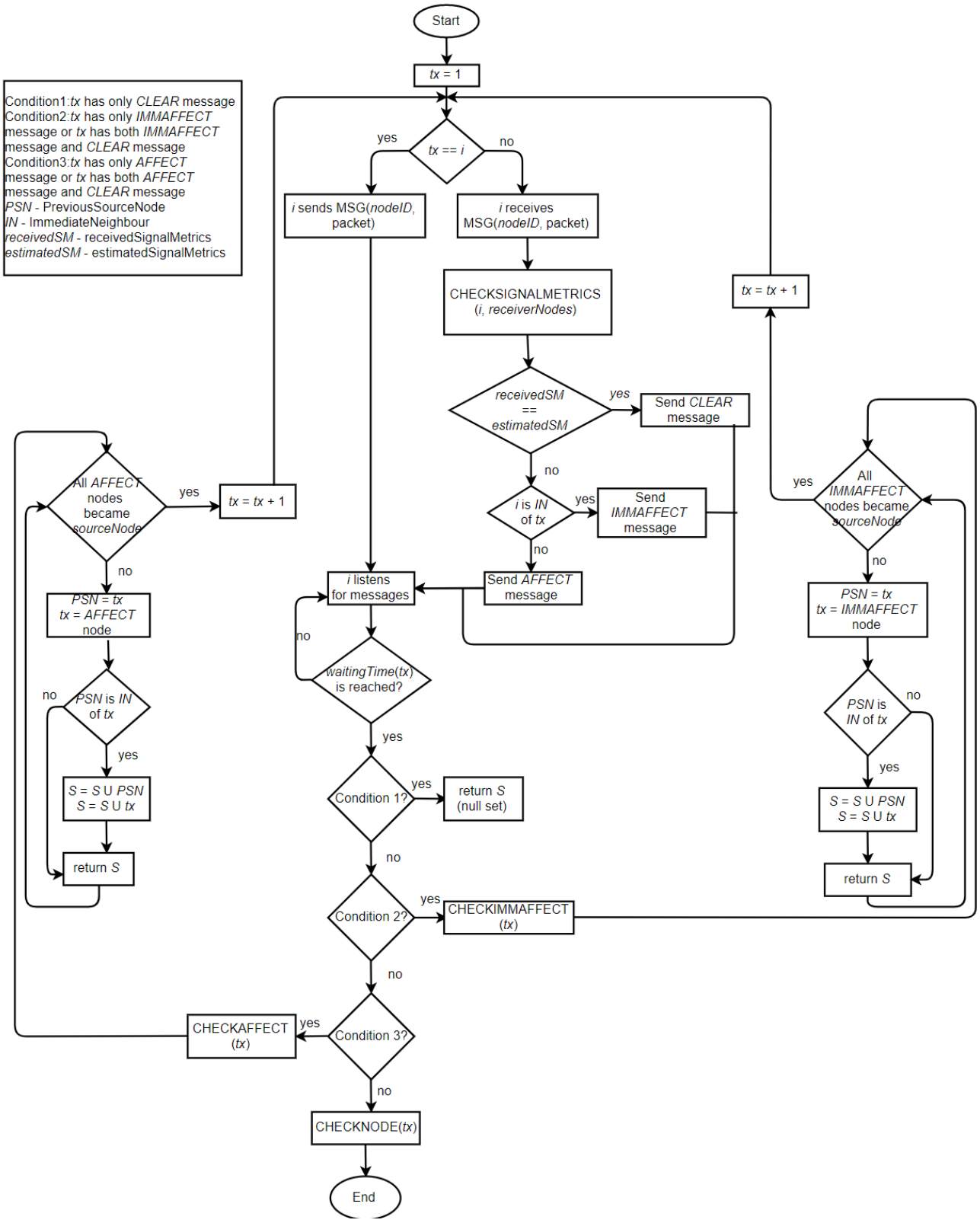

Figure 6.2: Flowchart for localization process

6.1.5 Algorithm Procedure

We discuss the localization process for the ith node as a transmitter and receiver. In this section, we discuss the proposed localization process shown in Figure 6.2.

1. The localization process always begins with node 1. The variable tx is set to 1 by default. The tx gets changed during the localization process.

2. First, we check if node i is equal to tx. If yes, then node i sends *MSG(nodeID, packet)* to other nodes and listens for messages from other nodes until *waitingTime* is reached. If node i is not equal to tx, then node i receives *MSG(nodeID, packet)* from tx if node i is one of the potential receiver nodes of the tx. In our case, all the nodes in the topology network are within the transmission range. *MSG(nodeID,packet)* consists of $nodeID$ of the tx and the packet.

3. Once node i receives the packet, it checks if *receivedSignalMetrics* is equal to *estimatedSignalMetrics*. If the signal metrics are equal, node i sends *CLEAR* message. If the signal metrics are not equal, node i checks if it is the immediate neighbour of tx. If node i is the immediate neighbour of tx, then node i sends a *IMMAFFECT* message to all the nodes in the network. If node i is not the immediate neighbour of tx, then node i sends *AFFECT* message to all the nodes.

4. All these messages are sent based on *priorityList* and *waitingTime* of the nodes. All the *receiverNodes* listens for messages from other nodes until *waitingTime* is reached.

5. Once the *waitingTime* is reached, tx checks its Table 6.2. If tx has only *CLEAR* message, then it means there is no leak. If tx has only *IMMAFFECT* message or both *IMMAFFECT* message and *CLEAR* message, then tx performs *CHECKIMMAFFECT(tx)*. If tx has only *AFFECT* message or both *AFFECT* message and

CLEAR message, then *tx* performs *CHECKAFFECT(tx)*. If not, then *tx* performs *CHECKNODES(tx)*

6. *CHECKIMMAFFECT(tx)* consists of *tx* node. The *tx* node becomes *previousSourceNode*. The higher priority node from the *IMMAFFECT* node becomes the *tx* and starts transmitting the signal. And the process continues, until all the nodes sends messages. If *tx* has *previousSourceNode* as the *IMMAFFECT* node, then the set with *previousSourceNode* and *tx* is returned.

7. *CHECKAFFECT(tx)* consists of *tx* node. The *tx* node becomes *previousSourceNode*. The higher priority node from the *IMMAFFECT* node becomes the *tx* and starts transmitting the signal. And the process continues, until all the nodes send messages. If *tx* has *previousSourceNode* as the *IMMAFFECT* node, then the set with *previousSourceNode* and *tx* is returned.

8. *CHECKNODES(tx)* consists of *tx* node. *CHECKNODES(tx)* performs *CHECKIMMAFFECT(tx)* and *CHECKAFFECT(tx)*. Once all the possible nodes from the *CHECKNODES(tx)* becomes *tx*, then *tx* is incremented by 1 and the process repeats.

9. The set returned during the localization process, consists of nodes that are immediate neighbours to each other. Once the set is returned, the focus should be near those nodes. Because, based on our algorithm, the leak is determined to be near the returned sensor nodes.

6.2 Performance Evaluation

6.2.1 Evaluation Parameters

Table 6.3: Evaluation parameters

Parameters	Value
transmission range r	1000 m or 2000 m
center frequency of the acoustic modem f	10 kHz
speed of sound in water c_{water}	1500 m/s
speed of sound in crude oil c_{oil}	1347.3 m/s
speed of sound in air c_{air}	343 m/s
transmitting power p_t	1 W
depth of the water	80 m
reference distance l_r	1 m

All the sensor nodes are placed on the seafloor either in a square grid topology or concentric hexagonal topology, as shown in Chapter 4 and Chapter 5. The position information of all the sensor nodes is assumed to be known *a priori*. Table 6.3 summarizes the evaluation parameters for localizing the leak in an underwater environment. The parameters we used correspond to the Modem 6 Sub-Mini, a widely used underwater monitoring acoustic modem designed by Sonardyne.

6.2.2 Analysis of Proposed Localization method

In Chapters 4 and 5, we discussed the detection of oil leak by two-dimensional and three-dimensional analysis. In UWSNs, in addition to the detection of an oil leak, localization of oil leaks is also important to prevent damage to the marine environment by taking necessary measures. In the previous section, we presented the localization algorithm for localizing the approximate area of the oil leak. In this section, we evaluate the performance of the proposed cooperative algorithm for localizing the leak.

6.2.2.1 Results on Localization using Square Grid Topology

Table 6.4: Localization results of square grid topology for leak location (-68, 260)

Source Node	Previous Source Node	Immediate Neighbours	IMMAFFECT	AFFECT	CLEAR
1	-	[2, 8, 9]	-	[18, 19, 26, 27, 28, 35]	All nodes except [18, 19, 26, 27, 28, 35]
18	1	[11, 17, 19, 25, 10, 12, 24, 26]	[10]	[9, 3, 2]	All nodes except [10, 9, 3, 2]
10	18	[3, 9, 11, 17, 2, 4, 16, 18]	[18]	[26, 34, 42]	All nodes except [18, 26, 34, 42]

We consider the square grid topology with 49 nodes placed on the seafloor. For discussing the result, we assume the oil leak location as (-68, 260). The results of localization for square grid topology is given in Table 6.4. As mentioned earlier, the order of the source node starts from 1. Node 1 acts as the source node and transmits the signal. Since the oil leak is at the location (-68, 260), the sensor nodes affected by the presence of oil are [18, 19, 26, 27, 28, 35]. The immediate neighbour nodes of node 1 are [2, 8, 9]. Based on our cooperative algorithm, since there are no IMMAFFECT nodes, node 18 becomes the source node and transmits the signal. The affected receiver nodes with node 18 as the source node are [10, 9, 3, 2]. Now, the power and time of arrival of the received signal are analyzed. The immediate neighbour nodes of node 18 are [11, 17, 19, 25, 10, 12, 24, 26]. From these affected receiver nodes, node 10 is the immediate neighbour of node 18. Node 10 becomes the source node and transmits the signal. The affected receiver node with node 10 as the source node are [18, 26, 34, 42]. Since node 18 is the previous source node and the first IMMAFFECT node for source node 10, node 18 and node 10 is added to the set and returned. The leak location is determined to be near the location of these two nodes. Localization process completed once the set is returned. Our localization algorithm does not precisely give the oil location, but it gives the oil leak's approximate location.

6.2.2.2 Results on Localization using Concentric Hexagonal Topology

Table 6.5: Localization results of concentric hexagonal topology with caisson for leak location (130, 200)

Source Node	Previous Source Node	Immediate Neighbours	IMMAFFECT	AFFECT	CLEAR
1	-	[2, 6, 7, 8, 13]	-	[20, 32, 44]	All nodes except [20, 32, 44]
20	1	[8, 13, 14, 25, 26, 32]	[8]	[1, 5, 11, 23, 35, 47]	All nodes except [8, 1, 5, 11, 23, 35, 47]
8	20	[1, 2, 7, 9, 13, 14, 20]	[20]	[32, 44]	All nodes except [20, 32, 44]

We consider the concentric hexagonal topology with 48 nodes placed on the seafloor. Let us assume that the oil leak is at the location (130, 200). The results of localization for concentric hexagonal topology is given in Table 6.5. As mentioned in the previous section, node 1 acts as the source node and transmits the sound signal. The receiver nodes affected by the presence of an oil leak is [20, 32, 44]. The immediate neighbours for node 1 are [2, 6, 7, 8, 13]. Since none of the affected receiver nodes are the immediate neighbours of the source node, the first node from the AFFECT nodes list becomes the next source node. Here, node 20 becomes the source node and transmits the signal. The affected receiver nodes with node 20 as the source node are [8, 1, 5, 11, 23, 35, 47]. The immediate neighbours of node 20 are [8, 13, 14, 25, 26, 32]. From the affected receiver nodes, node 8 is the IMMAFFECT node and rest of the nodes are the AFFECT nodes. All the nodes except the affected receiver nodes send a CLEAR message. Since, the previous source node and first IMMAFFECT node are not same, based on the algorithm, node 8 becomes the source node and transmit the signal. The affected receiver nodes are [20, 32, 44]. The immediate neighbour nodes of node 8 are [1, 2, 7, 9, 13, 14, 20]. The first node in the IMMAFFECT list and the previous source node is same, the pair with previous source node and current source node is returned and the localization process is completed. Therefore, we determine the oil leak is between node 8 and node 20.

6.2.2.3 Results on Localization using Concentric Hexagonal Topology with Caisson

Table 6.6: Localization results of concentric hexagonal topology for leak location (63, 55)

Source Node	Previous Source Node	Immediate Neighbours	IMMAFFECT	AFFECT	CLEAR
1	-	[2, 6, 7, 8, 13]	[2]	[9, 21, 27, 33, 39, 45]	All nodes except [2, 9, 21, 27, 33, 39, 45]
2	1	[1, 3, 8, 9, 14]	[1]	[7]	All nodes except [1, 7]

For concentric hexagonal topology with caisson, we consider 48 nodes placed on the seafloor. For the topology with the caisson, we focus on the area near the caisson, which is inside the inner hexagon in our case. So, we assume the same leak location (63, 55). The results of localization for concentric hexagonal topology with caisson is given in Table 6.6. Since there is a caisson in the middle, the number of receiver nodes affected by the presence of oil leaks will be reduced. This is because the signal travelling through the caisson will be absorbed, and it cannot reach the sensor nodes on the other side of the caisson. In some rare cases, if the signal reaches the sensor nodes on the other side of the caisson, for the considered receiver sensitivity, the signal metrics will not be measurable by our sensor nodes because the value will be too low to detect. So, we avoid the sensor nodes located at 180^o to the source node while calculating the topology results with caisson. Node 1 will act as the source node and transmits the signal. The receiver nodes affected by node 1 are [2, 9, 21, 27, 33, 39]. For concentric topology with caisson, the sensor nodes that are located 180^o to source node will not receive the signal because concrete absorbs the signal more. The immediate neighbour nodes to node 1 are [2, 6, 7, 8, 13]. Based on the cooperative localization algorithm, node 2 is the immediate neighbour and affected receiver node with respect to node 1, it becomes the source node and transmits the signal. For node 2, the affected receiver nodes are [1,7]. The immediate neighbour nodes of node 2 are [1, 3, 8, 9, 14]. Since, node 1 is the IMMAFFECT node of node 2 and the previous source node, so the set with previous source node and current source node is returned and the localization process is returned. Therefore, the oil leak is determined to be located near the area between node 1 and node 2.

Since leak detection precedes localization, the success attainable by the proposed leak detection method limits the success rate of leak localization. Once the leak is detected, our proposed localization algorithm locates the leak. The localization algorithm is based on a

cooperative approach. The results obtained are based on two or more nodes present in the topology network. In other words, if a leak is detectable, then that leak could be localized by the proposed localization algorithm. The evaluation results for the localization presented in this thesis would be accurate.

6.3 Summary

Localization is a significant issue in the UWSNs because of the challenges and limitations of the underwater environment. In this chapter, we proposed a cooperative scheme for localizing the leak based on the received power and estimated arrival time. Leak detection precedes localization and so the 85% success attainable in the proposed leak detection scheme limits the success rate of localization. In this cooperative scheme, the sensor nodes utilize the information from the other nodes to locate the position of the leak. We discuss the result of three different topologies we considered for our research. A typical set of parameters associated with the Modem 6 Sub-Mini was applied in our evaluation. Our proposed scheme can localize the leak by providing the leak location near the set of sensor nodes. The set can contain either two or more sensor nodes that are the immediate neighbour nodes to each other. As mentioned earlier, we can only detect 85% cases of leak locations based on the topology we considered, we can only localize 85% case of leak location by doing three-dimensional analysis.

Chapter 7

Conclusion and Future Work

In long-term marine monitoring applications, detection and localization of oil leak is a critical and challenging issue. This thesis presents schemes corresponding to different aspects of UWSNs, aiming at detecting and localizing the oil leak. Subsequent sections provide a summary of research contributions, conclusions, and suggestions for future work.

7.1 Conclusions

The main research contributions of this thesis are summarized as follows:

Comprehensive Study on propagation properties of acoustic signals and Underwater Channel Models

We reviewed propagation properties of acoustic signals in seawater in terms of absorption loss, sound speed profile, spreading loss, power, intensity, and arrival time. As well, we studied different transmission losses of acoustic signals with reflection and refraction of the signals. We then discussed the different deployment process and topologies used in UWSNs.

Two-Dimensional Leak Detection

For long-term environmental monitoring applications, we proposed a leak detection method

based on range estimation to detect the leak in the underwater environment. We perform two-dimensional analysis to study the performance of the proposed method. We studied the detection ratio and network scalability for square grid topology and concentric hexagonal topology. We further present the power and intensity values of the received signal. Based on the results, the two-dimensional analysis of the proposed leak detection method does not give the expected results, as we mentioned in Chapter 1.

Three-Dimensional Leak Detection

We addressed the leak detection problem in Chapter 4. The results of the two-dimensional analysis were not as expected as mentioned in Chapter 1. We performed a three-dimensional analysis of leak detection method for detecting the leak in UWSNs for square grid topology and concentric hexagonal topology. We present the detection ratio and network scalability of the sensor nodes placed in square grid topology or concentric hexagonal topology. The three-dimensional analysis of the proposed leak detection method achieved 85% detection ratio based on the results. Although our analysis does not achieve the expected result of 90% detection ratio, it detects 85% of the leaks at the early stage, which is acceptable compared to the results achieved in the two-dimensional analysis. We used untethered topology network for analysing the results of proposed scheme. The results of the proposed scheme would not affect if we use tethered topology network.

Localization of Leak

We proposed a localization algorithm for locating the leak in the underwater environment for long-term marine monitoring applications. In addition to detecting a leak, it is essential to localize the leak to take further measures to avoid future circumstances. We proposed the cooperative localization algorithm in which the sensor nodes utilize the information from the other sensor nodes in the topology. Using a cooperative method, we can effectively localize the leak within a short duration of time. The performance evaluation showed that

the proposed localization algorithm gives the best localization ratio for three-dimensional analysis. All the results mentioned in this thesis is based on untethered topology network. The detection and localization ratio would not improve if we used tethered topology network.

7.2 Suggested Future Research

In this thesis, we have studied different approaches to detect and localize the leak at an early stage in the underwater environment. Next, we present and discuss some suggestions ideas for future research.

Extension of Detection and Localization Method

We have proposed the detection and localization method for UWSNs with square grid topology and concentric hexagonal topology for long-term marine monitoring applications. The proposed method can be extended to other regular topologies based on the type of applications. Since, we did not achieve the expected results, a study on how to achieve atleast 90% results should be done.

Field Experiments and Proposed Scheme Implementation

Unlike terrestrial channel models, there is no consensus on the statistical characterization of underwater acoustic channel models due to spatial and temporal variability. It would be a significant step toward the research to implement the proposed detection and localization method on the commercial acoustic modems and evaluate the performance of the proposed schemes by field experiments.

Extension of Proposed Method to detect other targets

We developed an algorithm for detecting and localizing the presence of oil leak in UWSNs. Our proposed algorithm can be extended to detect targets such as icebergs, illegal fishing ships, and other enemy vehicles. We could also apply machine learning approach to detect

and localize oil leak in the underwater environment. If we build a model based on the training data, we could predict the oil leak in the underwater environment. We need statistical data based on the detected leaks and the reason for the oil leak.

References

[1] I. F. Akyildiz, D. Pompili, and T. Melodia, "Underwater acoustic sensor networks: research challenges," *Ad Hoc Networks*, vol. 3, no. 3, pp. 257 – 279, May 2005.

[2] M. Chitre, S. Shahabudeen, and M. Stojanovic, "Underwater acoustic communications and networking: Recent advances and future challenges," *Marine Technology Society Journal*, vol. 42, pp. 103–116, Spring 2008.

[3] M. Erol-Kantarci, H. T. Mouftah, and S. Oktug, "A survey of architectures and localization techniques for underwater acoustic sensor networks," *IEEE Communications Surveys Tutorials*, vol. 13, no. 3, pp. 487–502, 2011.

[4] J.Catipovic, D.Brady, and S.Etchemendy, "Development of underwater acoustic modems and networks," *Oceanography*, vol. 06, pp. 112–119, 1993.

[5] J. Rice, B. Creber, C. Fletcher, P. Baxley, K. Rogers, K. McDonald, D. Rees, M. Wolf, S. Merriam, R. Mehio, J. Proakis, K. Scussel, D. Porta, J. Baker, J. Hardiman, and D. Green, "Evolution of seaweb underwater acoustic networking," in *OCEANS 2000 MTS/IEEE Conference and Exhibition. Conference Proceedings*, vol. 3, 2000, pp. 2007–2017.

[6] G. A. Hollinger, S. Choudhary, P. Qarabaqi, C. Murphy, U. Mitra, G. Sukhatme, M. Stojanovic, H. Singh, and F. Hover, "Underwater data collection using robotic

sensor networks," *IEEE Journal on Selected Areas in Communications*, vol. 30, pp. 899–911, 2012.

[7] Z. Hu, L. Wang, C. Ye, and Z. He, "Research of acoustic survey devices applied on deepsea vehicles," in *IEEE/OES China Ocean Acoustics (COA)*, 2016, pp. 1–5.

[8] C. Joochim, R. Phadungthin, and S. Srikitsuwan, "Design and development of a remotely operated underwater vehicle," in *16th International Conference on Research and Education in Mechatronics (REM)*, 2015, pp. 148–153.

[9] L. Paull, S. Saeedi, M. Seto, and H. Li, "AUV navigation and localization: A review," *IEEE Journal of Oceanic Engineering*, vol. 39, no. 1, pp. 131–149, 2014.

[10] D. K. Miu, *Fundamentals of Electromagnetics*. New York, NY: Springer New York, 1993.

[11] J. Preisig, "Acoustic propagation considerations for underwater acoustic communications network development," *SIGMOBILE Mobile Computing Communications*, vol. 11, no. 4, p. 2–10, 2007.

[12] L. Lanbo, Z. Shengli, and C. Jun-Hong, "Prospects and problems of wireless communication for underwater sensor networks," *Wireless Communications and Mobile Computing*, vol. 8, no. 8, pp. 977–994, May 2008.

[13] M. Doniec, M. Angermann, and D. Rus, "An end-to-end signal strength model for underwater optical communications," *IEEE Journal of Oceanic Engineering*, vol. 38, no. 4, pp. 743–757, 2013.

[14] C. Gabriel, M. Khalighi, S. Bourennane, P. Leon, and V. Rigaud, "Monte-carlo based channel characterization for underwater optical communication systems," *IEEE/OSA Journal of Optical Communications and Networking*, vol. 5, no. 1, pp. 1–12, 2013.

[15] L. M. Brekhovskikh and Y. Lysanov, *Fundamentals of Ocean Acoustics*, 1st ed. Springer, March 2003.

[16] R. Urick, *Principles of Underwater Sound*, 3rd ed. McGraw Hill, New York, 1983.

[17] F. Jensen, W. Kuperman, M. Porter, and H. Schmidt, *Computational Ocean Acoustics*. NY: Springer, 2000.

[18] M. Stojanovic and J. Preisig, "Underwater acoustic communication channels: Propagation models and statistical characterization," *IEEE Communications Magazine*, vol. 47, pp. 84–89, Jan. 2009.

[19] M. Domingo, "A topology reorganization scheme for reliable communication in underwater wireless sensor networks affected by shadow zones," *Sensors (Basel, Switzerland)*, vol. 9, pp. 8684–708, 11 2009.

[20] D. Pompili, T.Melodia, and I.Akyildiz, "Three-dimensional and two-dimensional deployment analysis for underwater acoustic sensor networks," *Ad Hoc Networks*, vol. 7, pp. 778–790, Jun. 2009.

[21] D.Pompili, T.Melodia, and I.Akyildiz, "Deployment analysis in underwater acoustic wireless sensor networks," Sept. 2006, pp. 48–55.

[22] R. Jahnke, J. Bane, A. Barnard, J. Barth, F. Chavez, H. Dam, E. Dever, P. DiGiacomo, J. Edson, R. Geyer, S. Glenn, K. Johnson, M. Moline, J. O. Donnell, J. Oltman-Shay, O. Persson, O. Schofield, H. Sosik, and E. Terrill, "Coastal observatory research arrays: A framework for implementation planning," CoOP CORA Workshop, Tech. Rep., December 2003.

[23] WHOI, "https://catalog.data.gov/dataset/woods-hole-oceanographic-institutes-marthas-vineyard-coastal-observatory-component-locations-es," November 2020.

[24] Ocean Networks Canada, "https://www.oceannetworks.ca/observatories," July 2020.

[25] CRD Community Green Map, "http://crdcommunitygreenmap.ca/location/venus," June 2020.

[26] Marine Tech Centre, "https://marinetechcentre.ca/current-companies/venus/," July 2020.

[27] Ocean Networks Canada, "https://www.oceannetworks.ca/observatories/pacific/saanich-inlet," July 2020.

[28] CRD Community Green Map, "http://crdcommunitygreenmap.ca/location/venus-saanich-inlet-node," August 2020.

[29] Ocean Networks Canada, "https://www.oceannetworks.ca/observatories/pacific/strait-georgia," March 2020.

[30] CRD Community Green Map, "http://crdcommunitygreenmap.ca/location/venus-strait-georgia-central-node," July 2020.

[31] RUTGERS, "https://rucool.marine.rutgers.edu/," April 2020.

[32] WHOI, "http://4dgeo.whoi.edu/panama/index.html," July 2020.

[33] The official PRIMO Website, "http://science.whoi.edu/users/sgallager/primo/home.html," April 2020.

[34] Argo, "https://argo.ucsd.edu/," April 2020.

[35] OCEANSITES, "http://www.oceansites.org/," April 2020.

[36] The Global Ocean Observing System, "https://www.goosocean.org/," April 2020.

[37] New Millennium Observatory, "https://www.pmel.noaa.gov/eoi/nemo/," August 2020.

[38] Ocean Networks Canada, "https://www.oceannetworks.ca/observatories/pacific#northeast," September 2020.

[39] C. Barnes, M. Best, and A. Zielinski, "The neptune canada regional cabled ocean observatory," *Sea Technology*, vol. 49, pp. 10–14, 07 2008.

[40] Folger Passage, "https://www.oceannetworks.ca/introduction-folger-passage," September 2020.

[41] Barkeley Canyon, "https://www.oceannetworks.ca/introduction-barkley-canyon," August 2020.

[42] Cascadia Basin, "https://www.oceannetworks.ca/introduction-cascadia-basin," July 2020.

[43] Endeavour, "https://www.oceannetworks.ca/introduction-endeavour-0," March 2020.

[44] Clayoquot Slope c, "https://www.oceannetworks.ca/introduction-clayoquot-slope," July 2020.

[45] Monterey Accelerated Research System Cabled Observatory, "https://www.mbari.org/at-sea/cabled-observatory/," July 2020.

[46] WHOI, "https://www.whoi.edu/science/aope/dso/h2o/," August 2020.

[47] ESONET, a Network of Excellence, "http://www.esonet-noe.org/about-esonet," July 2020.

[48] Sonardyne, "https://www.sonardyne.com/product/bluecomm-underwater-optical-communication-system/," July 2020.

[49] DSPComm, "https://www.dspcommgen2.com/aquacomm-underwater-wireless-modem/," July 2020.

[50] M. Naderi, M. Patzold, and A. G. Zajic, "A geometry-based channel model for shallow underwater acoustic channels under rough surface and bottom scattering conditions," *2014 IEEE Fifth International Conference on Communications and Electronics (ICCE)*, July 2014.

[51] M. Chitre, "A high-frequency warm shallow water acoustic communication channel model and measurements," *The Journal of the Acoustical Society of America*, pp. 2580–2586, Nov 2007.

[52] M. Chitre, J. Potter, and O. Heng, "Underwater acoustic channel characteristics for medium-range shallow water communications," vol. 01, Nov. 2007, pp. 40–45.

[53] M. Stojanovic and J. Preisig, "Underwater acoustic communication channels: Propagation models and statistical characterization," *IEEE Communications Magazine*, pp. 84–89, Jan. 2009.

[54] T. Yang, "Measurements of temporal coherance of sound transmissions through shallow water," *The Journal of the Acoustical Society of America*, pp. 2595–2614, Nov 2006.

[55] W. Yang and T. Yang, "High-frequency channel characterization for m-ary frequency-shift keying underwater acoustic communcations," *The Journal of the Acoustical Society of America*, pp. 2615–2626, Jan 2006.

[56] I. Udovydchenkov, R. Stephen, T. F. Duda, S. Bolmer, P. Worcester, M. Dzieciuch, J. Mercer, R. Andrew, and B. Howe, "Bottom interacting sound at 50 km range in a

deep ocean environment," *The Journal of the Acoustical Society of America*, vol. 132, pp. 2224–2231, Oct. 2012.

[57] T. Shimura, H. Ochi, and H. Song, "Experimental demonstration of multiuser communciation in deep water using time reversal," *The Journal of the Acoustical Society of America*, vol. 134, pp. 3223–3229, Oct. 2013.

[58] K. Sadeghi and M. Musa, "Semisubmersible platforms: Design and fabrication: An overview," *Academic Research International*, vol. 10, pp. 28–38, 03 2019.

[59] A. Martini, M. Troncossi, and A. Rivola, "Leak detection in water-filled small-diameter polyethylene pipes by means of acoustic emission measurements," *Applied Sciences*, 2017.

[60] S. Datta and S. Sarkar, "A review on different pipeline fault detection methods," *Journal of Loss Prevention in the Process Industries*, pp. 97–106, May 2016.

[61] S. Davoodi and A. Mostafapour, "Theoretical analysis of leakage in high pressure pipe using acoustic emission method," *Advanced Material Research*, pp. 917–922, Jan. 2012.

[62] S. W. Oh, D. Yoon, G. J. Bae, and H. S. Kim, "Acoustic data condensation to enhance pipeline leak detection," *Nuclear Engineering and Design*, pp. 198–211, Feb.2018.

[63] R. Cramer, D. Shaw, R. Tulalian, and V. S. P Angelo, "Detecting and correcting pipeline leaks before they become a big problem," *Society of Petroleum Engineers*, 2015.

[64] F. Tanimola and D. Hill, "Distributed fibre optic sensors for pipeline protection," *Journal of Natural Gas Science and Engineering*, pp. 134–143, Nov. 2009.

[65] Z. Jia, Z. Wang, and Z. L. W Sun, "Pipeline leakage localization based on distributed fbg hoop strain measurements and support vector machine," *Optik*, pp. 1–13, 2019.

[66] A. Khan, V. Vrabie, J. Mars, A. Girard, and G. D'Urso, "A source separation technique for processing of thermometric data from fibre-optic dts measurements for water leakage identification in dikes," *IEEE Sensors*, pp. 1118–1129, 2008.

[67] D. P. A Kroll, W Baetz, "On autonomous detection of pressured air and gas leaks using passive ir-thermography for mobile robot application," 2009, pp. 921–926.

[68] S. Zhang, B. Liu, and J. He, "Pipeline deformation monitoring using distributed fibre optical sensor," *Measurements*, 2019.

[69] J. Du, L. Wang, C. Cai, C. Yin, and G. Zhao, "On autonomous detection of pressured air and gas leaks using passive ir-thermography for mobile robot application," Dec. 2017, pp. 137–140.

[70] M. Golmohamadi, "Pipeline leak detection," *Master's Thesis, Missouri University of Science and Technology*, 2015.

[71] P. Murvay and I. Silea, "A survey on gas leak detection and localization techniques," *Journal of Loss Prevention in the Process Industries*, pp. 966–973, 2012.

[72] M. Ahmed, A. Shama, E. Mohammad, and K. Mohammad, "Review of leakage detection methods for subsea pipeline," *17th International Congress of the International Maritime Association of the Mediterranean*, pp. 1–9, 2017.

[73] S. L. Scott and M. A. Barrufet, "Worldwide assessment of industry leak detection capabilities for single and multiphase pipelines," *OffShore Technology Research Center College Station*, 2003.

[74] M. H. Manekiya and P. Arulmozhivarman, "Leakage detection and estimation using ir thermography," 2016, pp. 1516–1519.

[75] L. Boaz, S. Kaijage, and R. Sinde, "An overview of pipeline leak detection and location systems," Jul. 2014.

[76] P. C. Mandal, "Gas leak detection in pipelines and repairing system of titas gas," *Journal of Applied Engineering*, pp. 23–34, 2014.

[77] L. Quaife and D. Acker, "Pipeline leak location technique using a novel test fluid and trained dogs," Feb. 1993.

[78] D. A. Anisi and C. Skourup, "A step-wise approach to oil and gas robotics," Jun 2012, pp. 47–52.

[79] C. Gomez and D. R. Green, "Small unmanned airborne systems to support oil and gas pipeline monitoring and mapping," *Arabian Journal of Geosciences*, pp. 202–209, 2017.

[80] T. R. Sheltami, A. Bala, and E. M. Shakshuki, "Wireless sensor networks for leak detection in pipelines: A survey," *Journal of Ambient Intelligence and Humanized Computing*, pp. 347–356, 2016.

[81] P. Ostapkowicz, "Leak detection in liquid transmission pipelines using simplified pressure analysis techniques employing a minimum of standard and non-standard measuring devices," *Engineering Structures*, pp. 194–205, 2016.

[82] Z. Yu, L. Jian, and S. J. Z Zhoumo, "A comnined kalman filter-discrete wavelet transform method for leakage detection of crude oil pipelines," Aug. 2009, pp. 3–1086 – 3–1090.

[83] Alaska Department of Environmental Conservation, "Technical review of leak detection technologies," 1999.

[84] N. Yashwanth and B. R. Sujatha, "Wireless sensor node localization in underwater environment," *2016 International Conference on Electrical, Electronics, Communication, Computer and Optimization Techniques (ICEECCOT)*, 2016.

[85] D. Park, K. Kwak, J. Kim, and W. K. Chung, "3D underwater localization scheme using em wave attenuation with a depth sensor," *2016 IEEE International Conference on Robotics and Automation (ICRA)*, 2016.

[86] C. Kim, S. Lee, and K. Kim, "3D underwater localization with hybrid ranging method for near-sea marine monitoring," *2011 IFIP 9th International Conference on Embedded and Ubiquitous Computing*, 2011.

[87] M. Isik and O. Akan, "A three dimensional localization algorithm for underwater acoustic sensor networks," *IEEE Transactions on Wireless Communications*, pp. 4457–4463, 2009.

[88] V. M. Janik, S. M. Parijs, and P. M. Thompson, "A two-dimensional acoustic localization system for marine mammals," *Marine Mammal Science*, pp. 437–447, 2000.

[89] T. Bian, R. Venkatesan, and C. Li, "Design and evaluation of a new localization scheme for underwater acoustic sensor networks," *GLOBECOMM 2009- IEEE Global Telecommunications Conference*, 2009.

[90] D. Mirza and C. Schurgers, "Motion-aware self-localization for underwater networks," *ACM international workshop on Wireless network testbeds, experimental evaluation and characterization - WuWNeT*, 2008.

[91] V. Chandrasekhar and W. Seah, "An area localization scheme for underwater sensor networks," *OCEANS 2006*, 2006.

[92] W. Cheng, A. Teymorian, L.Ma, X.Cheng, and X.Lu, "Underwater localization in sparse 3D acoustic sensor networks," *IEEE INFOCOM - The 27th Conference on Computer Communications*, 2008.

[93] H. Luo, Z. Guo, W. Dong, F. Hong, and Y. Zhao, "LDB: localization with directional beacons for sparse 3D underwater acoustic sensor networks," *Journal of Networks*, vol. 1, 2010.

[94] H. P. Tan, R. Diamant, W. K. G. Seah, and M. Waldmeyer, "A survey of techniques and challenges in underwater localization," *Ocean Engineering*, vol. 38, pp. 1663–1676, 2010.

[95] R. M. Vaghefi and R. M. Buehrer, "Asynchronous time-of-arrival-based source localization," in *2013 IEEE International Conference on Acoustics, Speech and Signal Processing*, 2013, pp. 4086–4090.

[96] I. Ullah, J. Chen, X. Su, C. Esposito, and C. Choi, "Localization and detection of targets in underwater wireless sensor using distance and angle based algorithms," *IEEE Access*, vol. 7, pp. 45 693–45 704, 2019.

[97] J. Yi, D. Mirza, R. Kastner, C. Schurgers, P. Roberts, and J. Jaffe, "ToA-TS: Time of arrival based joint time synchronization and tracking for mobile underwater systems," *Ad Hoc Networks*, vol. 34, pp. 211–223, 2015.

[98] D. Mirza, P. Naughton, C. Schurgers, and R. Kastner, "Real-time collaborative tracking for underwater networked systems," *Ad Hoc Networks*, vol. 34, pp. 196–210, 2015.

[99] R. Peng and M. L. Sichitiu, "Angle of arrival localization for wireless sensor networks," in *2006 3rd Annual IEEE Communications Society on Sensor and Ad Hoc Communications and Networks*, vol. 1, 2006, pp. 374–382.

[100] J. B. Andersen and K. I. Pedersen, "Angle-of-arrival statistics for low resolution antennas," *IEEE Transactions on Antennas and Propagation*, vol. 50, no. 3, pp. 391–395, 2002.

[101] K. Tong, X. Wang, A. Khabbazibasmenj, and A. Dounavis, "RSS-Based localization in obstructed environment with unknown path loss exponent," in *2014 IEEE 80th Vehicular Technology Conference (VTC2014-Fall)*, 2014, pp. 1–5.

[102] T. L. N. Nguyen and Y. Shin, "An efficient RSS localization for underwater wireless sensor networks," *Sensors*, vol. 19, no. 14, 2019.

[103] T. Xu, Y. Hu, B. Zhang, and G. Leus, "RSS-based sensor localization in underwater acoustic sensor networks," *Proceedings of the IEEE International Conference on Acoustics,Speech and Signal Processing(ICASSP)*, pp. 3906–3910, May 2016.

[104] M. Hosseini, H. Chizari, Chai Kok Soon, and R. Budiarto, "RSS-based distance measurement in underwater acoustic sensor networks: An application of the lambert w function," in *2010 4th International Conference on Signal Processing and Communication Systems*, 2010, pp. 1–4.

[105] J. Gao, X. Shen, and H. Wang, "A hybrid localization algorithm for multi-hop mobile underwater acoustic networks," *Journal of Sensors*, vol. 22, pp. 494–500, 2017.

[106] V. Chandrasekhar, W. K. Seah, Y. S. Choo, and H. V. Ee, "Localization in underwater sensor networks: survey and challenges," *ACM international workshop on Underwater networks*, pp. 33–40, Sept. 2006.

[107] W. Wang, S. Li, J. Yang, Z. Liu, and W. Zhou, "Feature extraction of underwater target in auditory sensation area based on mfcc," in *2016 IEEE/OES China Ocean Acoustics (COA)*, 2016, pp. 1–6.

[108] T. S. Tiang and M. N. Mahyuddin, "Cooperative formation control algorithm of a generic multi-agent system applicable for multi-autonomous surface vehicles," in *2016 IEEE International Conference on Underwater System Technology: Theory and Applications (USYS)*, 2016, pp. 133–138.

[109] C. C. Leroy, S. P. Robinson, and M. J. Goldsmith, "A new equation for the accurate calculation of sound speed in all oceans," *The Journal of the Acoustical Society of America*, 2008.

[110] H. Medwin, "Speed of sound in water: A simple equation for realistic parameters," *The Journal of the Acoustical Society of America*, 1975.

[111] Mackenzie, "Nine-term equation for sound speed in the oceans," *The Journal of the Acoustical Society of America*, 1981.

[112] L. Kinsler, A. Frey, A. Coppens, and J. Sanders, *Fundamentals of Acoustics*. John Wiley and Sons, 2000.

[113] E. Westwood and P. Vidmar, "Eigenray finding and time series simulation in a layered-bottom ocean," *The Journal of the Acoustical Society of America*, vol. 81, pp. 912–924, Nov. 1987.

[114] M. Zorzi, P. Casari, N. Baldo, and A. Harris, "Energy-efficient routing schemes for underwater acoustic networks," *IEEE Journal on Selected Areas in Communications*, vol. 26, pp. 1754–1766, Nov. 2008.

[115] R. Su, R. Venkatesan, and C. Li, "Acoustic propagation properties of underwater communication channels and their influence on the medium access control protocols," *IEEE International Conference on Communications (ICC)*, 2012.

[116] P. C. Etter, *Underwater Acoustic Modeling and Simulation*, 3rd ed. Boca Raton, FL: CRC Press, 2003.

[117] J. A. Kleppe, *Engineering Applications of Acoustics*. Norwood, MA:Artech House, 1989.

[118] D. Sun, J. Dung, C. Zheng, and W. Huang, "An underwater acoustic positioning algorithm for compact arrays with arbitrary configuration," *IEEE Journal of Selected Topics in Signal Processing*, vol. 13, pp. 120–130, Feb. 2019.

[119] V. A.Shutilov, *Fundamental Physics of Ultrasound*. Gordon and Breach Science Publishers, 1988.

[120] H. Medwin and L. S. Clay, *Fundamentals of Acoustical Oceanography*. McGraw Hill, 1983.

[121] G. Han, C. Zhang, L. Shu, and N. Sun, "A survey on deployment algorithms in underwater acoustic sensor networks," *International Journal of Distributed Sensor Networks*, pp. 1–11, 2013.

[122] D. Pompili, T.Melodia, and I.Akyildiz, "Topology structure design for underwater acoustic wireless sensor network," *IEEE International Conference of IEEE Region 10 (TENCON 2013)*, 2013.

Appendices

Appendix A: Modem Specification

In this Appendix A, we present the specifications of Sonardyne Modem 6 Sub-mini. We choose the parameters for our calculations based on the specifications of Sonardyne Modem 6 Sub-mini. The receiver sensitivity of this modem represents the sensitivity of the modem to measure the received signal. We might need external detector to measure the received signal strength.

Sonardyne Global Headquarters
T. +44 (0) 1252 872288
F. +44 (0) 1252 876100
E. sales@sonardyne.com
www.sonardyne.com

Datasheet

Modem 6 Sub-Mini (Subsea)

Description

The Modem 6 range, based on existing 6G equipment, provides a reliable and cost-effective method of wirelessly transferring underwater sensor data in real-time.

The Modem 6 Sub-Mini is a compact and easy-to-mount instrument, suitable for transmission of data from a wide range of sensors including: current profilers, temperatures, depth and custom instrumentation.

Type 8377-1111 is depth rated to 1,000 m and has an omni-directional transducer designed for excellent horizontal and shallow water communication.

Type 8377-4112 is depth rated to 4,000 m and has a directional transducer.

Modem 6 is a flexible range of instruments, supporting specific communication settings for a variety of link types such as low latency data, fire and forget, acknowledged and large data uploads. A 512 kB modem buffer stores data when a modem link is not active.

All Modem 6 products utilise Sonardyne Wideband® signal processing and standard 6G control language. They can be programmed using the supplied software and a serial link or any third-party terminal software.

This technology is field proven and provides unprecedented levels of robustness and flexibility in challenging acoustic environments.

Data transfer rates range from 9,000 bps down to 200 bps depending on the environment.

Advanced communication protocols and intelligent data packet stitching ensure latency is minimised and data is delivered error free.

For safety, a pressure relief valve is incorporated, and an external on/off switch saves the rechargeable battery when not in use.

Key Features

- Sonardyne Wideband® telemetry provides up to 9,000 bps actual acoustic data rate
- Compatible with all Modem 6 instruments
- Full two-way Sonardyne Wideband 2 interrogation and reply – mitigates interference and multi-path issues
- Incorporates field proven communication technology used within critical subsea applications
- More than 500 unique Sonardyne addresses
- Robust performance in noisy and reverberant environments
- Rechargeable NiMH battery
- External on/off switch for saving battery when not in use
- Rugged, easy to mount housing

Sonardyne Global Headquarters
T. +44 (0) 1252 872288
F. +44 (0) 1252 876100
E. sales@sonardyne.com
www.sonardyne.com

Specifications

Modem 6 Sub-Mini (Subsea)

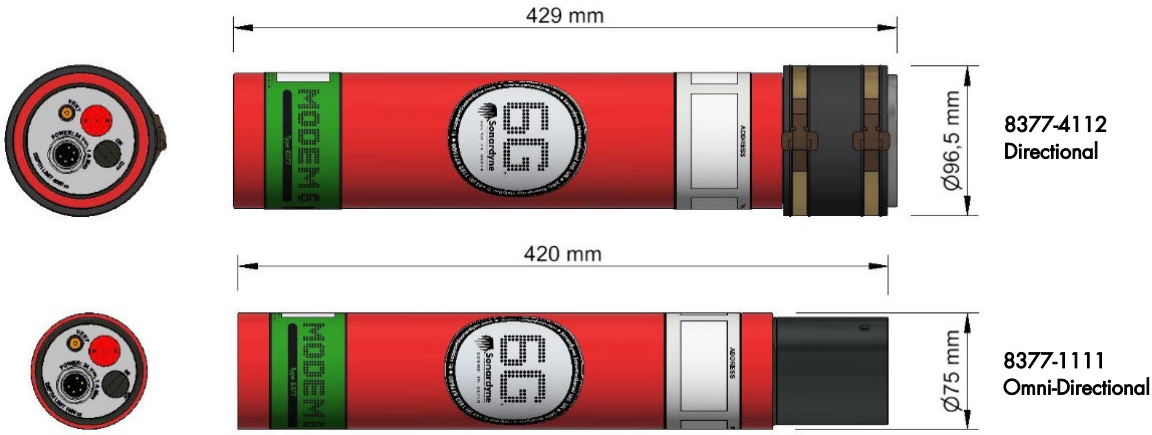

Feature	Type 8377-1111	Type 8377-4112
Depth Rating	1,000 metres	4,000 metres
Operating Frequency	MF (21–32.5 kHz)	MF (21–32.5 kHz)
Transceiver Beam shape	Omni-directional	Directional
Maximum Data Rate	9000 bps	9000 bps
Serial Port (RS232)	2400–115200 baud	2400–115200 baud
Data Buffer/Storage	512 kB	512 kB
Range*	1–1.5 km	3–4 km
Transmit Source Level (re. 1 µPa @ 1 m)	181 dB	187 dB
Receive Sensitivity (dB re 1 µPa)	<85 dB	<80 dB
Power Supply	Rechargeable NiMH battery or external 24 V	Rechargeable NiMH battery or external 24 V
Battery charge 0-100 %	5 hours	5 hours
Quiescent Life (Battery)	>35 Days	>35 Days
Connector 5-Way (Standard)	Subconn MCBH5M	Subconn MCBH5M
Mechanical Construction	Aluminium alloy, anodised	Aluminium alloy, anodised
Operating Temperature	-5 to 40°C	-5 to 40°C
Storage Temperature	-20 to 55°C	-20 to 55°C
Dimensions (Length x Diameter)	420 x 75 mm	429 x 97 mm
Weight in Air/Water**	3.2/1.3 kg	5.5/3.2 kg
Battery Charger	8370-011-01	8370-011-01

*Depends on ambient noise level and ray bending due to SVP.

**Estimated weights

Pin	Description
1	RS232 comms In (RX)
2	0 V
3	RS232 comms Out (TX)
4	External power 24 V
5	N/A

Appendix B: Additional Results for Power and Intensity

In Chapter 4 and Chapter 5, we discussed the results of power and intensity with 0.2 nW as the receiver sensitivity. In this section, we discuss the results of power and intensity of the received signal for three different topologies and 0.2 μW as the receiver sensitivity. The detection percentage is the same for the receiver sensitivity 0.2 nW and 0.2 μW. The number of affected receiver nodes increased for the receiver sensitivity 0.2 nW compared to 0.2 μW receiver sensitivity. The results shown in Figure 1 are calculated for square grid topology with 49 nodes having 161 m as the distance between adjacent nodes and concentric hexagonal topology with 48 nodes having 1200 m as the diameter of the outer hexagon. We consider conical-shaped oil leak with a diameter of 3 m near the ocean floor for showing the results of power and intensity.

For analyzing the results using square grid topology, we show the results based on 5 different source nodes. For consistency, we choose the same source nodes 7, 14, 13, 19, and 25 considered for two-dimensional analysis.

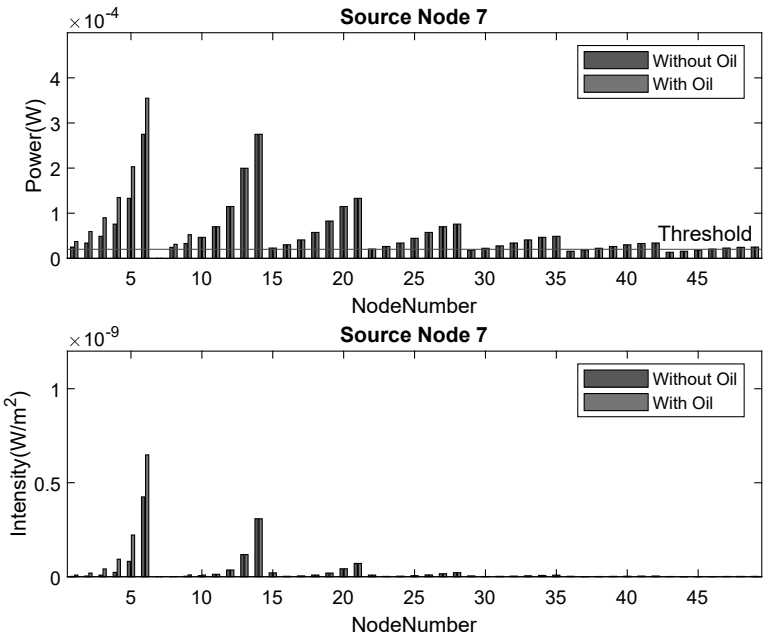

Figure 1: Power and Intensity values based on three-dimensional analysis for square grid topology with 49 Nodes

Figure 1 shows the power and intensity values for the source node 7. In Figure 1, the label "Without Oil" represents the results of power and intensity without the presence of oil and the label "With Oil" represents the results of power and intensity with the presence of oil. The nodes 1, 2, 3, 4, 5, 6, 8, and 9 are the affected receiver nodes for the oil leak at the location (470, 483).

Table 1: Power and Intensity of received signal for three-dimensional analysis of oil leak using square grid topology

Source Node	Leak Location	Affected Receiver Nodes
7	(470, 483)	[1, 2, 3, 4, 5, 6, 8, 9]
14	(470, 322)	[1, 2, 8, 9, 10, 11, 12, 15, 16]
13	(300, 322)	[8, 9, 10]
19	(150, 161)	[8, 15, 16, 17, 18, 22]
25	(1, 40)	[4, 11, 18]

From the three-dimensional analysis, Table 1 lists the considered source node with leak location, and corresponding affected receiver nodes. Similar to what we assumed for two-dimensional analysis, we consider the same threshold value for the three-dimensional analysis. We can see from the Figure 1, for the source node 7, the receiver nodes except 29, 36, 37, 43, 44, and 45 will be able to receive the transmitted signal from the source node. The calculated received power for nodes 29, 36, 37, 43, 44, and 45 is less than the considered threshold value. It should also be noted that the transmitted signal reaching the nearest node is most likely to have the higher received power than the transmitted signal reaching the farthest node from the source node. For example, in the case of source node 7, the nearest node is 6 and 14, and the farther node is 42. The nearest and the farthest node varies for each source node.

If the receiver sensitivity is 0.2 nW, received power of all the nodes is above the receiver sensitivity threshold. From this analysis, we conclude that if we use 0.2 nW as the receiver sensitivity, we get more affected nodes for some cases which will be useful for locating the oil leak.